UNIVERSITY OF TRENTO

Doctoral School in Civil, Environmental and
Mechanical Engineering

Curriculum 1. Civil and Environmental Engineering

Daniele Rossi

SAR data processing for the detection and monitoring of braided gravelbed rivers morphodynamics

2024 - Doctoral thesis

UNIVERSITY OF TRENTO - Italy
Department of Civil, Environmental
and Mechanical Engineering

Doctoral School in Civil, Environmental and Mechanical Engineering
Topic 1. Civil and Environmental Engineering - XXXV cycle 2020/2022

Doctoral Thesis - March 2024

Daniele Rossi

SAR data processing for the detection and monitoring of braided gravelbed rivers morphodynamics

Supervisors
Alfonso Vitti, University of Trento
Guido Zolezzi, University of Trento
Walter Bertoldi, University of Trento

Credits of the cover image: Archivio fotografico ERPAC
Servizio catalogazione, promozione, valorizzazione e sviluppo del territorio
Micossi Mario - Grande veduta del Tagliamento verso il mare da monte Ragogna

University of Trento
Doctoral School in Civil, Environmental and Mechanical Engineering
http://web.unitn.it/en/dricam
Via Mesiano 77, I-38123 Trento
Tel. +39 0461 282670 / 2611 - *dicamphd@unitn.it*

Contents

Abstract

BRAIDED rivers represent one of the most complex forms of natural streams. Characterized by intense bed-load transport and highly dynamic channels, they carry significant naturalistic value and support a multiplicity of ecosystem services. Anthropogenic stressors and environmental changes put under stress hydro-morphological dynamics, biological processes, and ecosystem functioning and services of these fragile environments, necessitating integrated management and conservation strategies to preserve their biodiversity and ecological integrity.

From a regulatory perspective, the two European Directives 2007/60/EC (the Floods Directive) and 2000/60/EC (the Water Framework Directive) identify and promote win–win measures that both reduce hydraulic risk and enhance the quality of water bodies. Some examples of win–win measures are river naturalization projects that not only restore river ecosystems to their natural state, enhancing biodiversity and ecosystem services but also provide flood protection, improve water quality, and offer recreational opportunities for local communities. This thesis contributes to the development of scientific knowledge in the previously mentioned areas, facilitating the know-how transfer of expertise from academia to the public institution. Building on these premises, this thesis aims to provide additional insights into the morphodynamics of braided rivers, offering new perspectives on the evolution of morphological indices during flood events and contributing valuable knowledge on how these complex systems respond to external stressors. The PhD thesis has been structured along three parts.

The primary goal was to develop an innovative unsupervised algorithm for extracting the spatial and temporal evolution of braided river morphology. This computational framework is tailored for Sentinel–1 Synthetic Aperture Radar (SAR) data, overcoming the limitations imposed by weather conditions and day–night cicles. Moreover, it can be effortlessly adapted to additional SAR imagery databases. In cases where the water class covers only a minimal area of the entire scene, the histogram primarily represents the dry soil class. The framework faces this challenge employing a Self-Adaptive Thresholding Approach (SATA) to achieve a distinct bimodal distribution, enabling the accurate computation of threshold values for the ’dry soil’ and ’water’ classes. The tool, developed within the Python–API of Google Earth Engine (GEE), allowed us to assess the intra–event inundation dynamics, the estimation of the relationship between hydrometric level and wet area extension, and the assessment of bank erosion phenomena.

The second chapter focuses on analyzing how morphological indices, such as the Total Braiding Intensity (TBI) index defined as the number of active channels, the Maximum Channel distance (MCD) defined as the distance between the most external channels, and the Cross-Sectional Cumulative Wetted Area (WA) defined as the sum of the wet area of all chanels in a cross section, correlate with discharge variations during flood events. To achieve this objective, the framework designed for Sentinel–1 images was adapted for use with high–definition imagery from the Italian COSMO–SkyMed satellite constellation. Leveraging the superior ground resolution of 3x3 meters provided by the Italian COSMO–SkyMed satellite constellation, we successfully segmented narrow secondary branches that remained undetected with Sentinel–1’s 5x20 meter resolution. Thus obtained, the temporal evolution of the braiding system, enables us to evaluate the temporal evolution and the relationship between the TBI, MCD, and WA indices with increasing discharge values.

The last part of the PhD thesis, deals with the assessment of the river bed grain size. The initial concept behind this PhD work was to analyze the potential of Synthetic Aperture Radar (SAR) data in assessing not only river morphology but also the pattern of patches with different grain size. While the initial two parts of the work addressed this, the final section’s analysis of SAR data, unfortunately, did not provide significant results. Nevertheless, the subjects of surface roughness and the creation of spatially distributed grain size maps continue to hold significant scientific value in the fields of hydraulic and eco–hydraulic modeling and a key information for river management and renaturation projects. The principal role of this factor led us to slightly shift the research focus towards a detailed investigation of these elements, utilizing orthophotos, digital imagery, and corresponding analytical methods to model patterns of river roughness and grain size. A map illustrating the spatial pattern of grain size at the river reach scale was produced through regression analysis. This analysis correlated the texture properties derived from orthophoto tiles with the d50, d84, d90, and d95 grain size characteristics obtained from digital images, thereby providing considerable support for the implementation of detailed hydraulic models.

Chapter 1

Monitoring the river dynamics evolution occurring during extreme events with Sentinel–1

Abstract

Remote sensing plays a central role in the assessment of environmental phenomena and has increasingly become a powerful tool for monitoring shorelines, river morphology, flood–wave delineation and flood assessment. Optical–based monitoring and the characterization of river evolution at long time scales is a key tool in fluvial geomorphology. However, the evolution occurring during extreme events is crucial for the understanding of the river dynamics under severe flow conditions and requires the processing of data from active sensors to overcome cloud obstructions. This work proposes a cloud–based unsupervised algorithm for the intra–event monitoring of river dynamics during extreme flow conditions based on the time series of Sentinel–1 SAR data. The method allows the extraction of multi–temporal series of spatially explicit geometric parameters at high temporal and spatial resolutions, linking them to the hydrometric levels acquired by reference gauge stations. The intra–event reconstruction of inundation dynamics has led to (1) the estimation of the relationship between hydrometric level and wet area extension and (2) the assessment of bank erosion phenomena. In the first case, the behavior exhibits a change when the hydrometric level exceeds 1 m. In the second case, the erosion rate and cumulative lateral erosion were evaluated. The maximum erosion velocity was greater than 1 m/h, while the cumulative lateral erosion reached 130 m. Time series of SAR acquisitions, provided by Sentinel–1 satellites, were analyzed to quantify changes in the wet area of a reach of the Tagliamento river under different flow conditions. The algorithm, developed within the Python–API of GEE, can support many types of analyses of river dynamics, including morphological changes, floods monitoring, and bio-physical habitat dynamics. The results encourage future advancements and applications of the algorithm, specifically exploring SAR data from ICEYE and Capella Space constellations, which offer significantly higher spatial and temporal resolutions compared to Sentinel–1 data.

The content of this chapter has been published as:
Rossi D., Zolezzi G., Bertoldi W., Vitti A. 2023. Monitoring Braided River-Bed Dynamics at the Sub-Event Time Scale Using Time Series of Sentinel–1 SAR Imagery. *Remote Sensing*, 15, 3622. DOI: `https://doi.org/10.3390/rs15143622`

Author contributions:
Conceptualization: **D.R.**, A.V., W.B. and G.Z., *Data curation*: **D.R.**, *Formal analysis*: **D.R.** and A.V., *Methodology*: **D.R.**, A.V. and W.B., *Software*: **D.R.**, *Supervision*: A.V., W.B. and G.Z.

1.1 Introduction

Rivers and their floodplains are among the most complex, dynamic, and diverse ecosystems on Earth, providing major economic, health, cultural, scientific, and educational ecosystem services [4, 73]. Despite accounting for just 1.4% of the land surface area, riparian zones provide at least 25% of all terrestrial ecosystem services [93]. Rivers' dynamic behavior originates from the continuous interaction between variable flow, sediment transport and associated morphological change, and ecological feedback, mainly through aquatic and riparian vegetation [35, 22, 83]. Most of these dynamic processes occur during floods, which are characterized by the increase in flowing discharge, often associated with a large widening of the inundated areas, both inside the active channel and in adjacent zones. The possibility of understanding, quantifying, and predicting river evolution strongly depends on our ability to monitor what happens during these events, which in some cases last for only a few hours or days but can shape the riverbed morphology for the following months and years [74, 36]. The accurate monitoring of the dynamics of rivers and floodplains plays a vital role in improving river management practices and achieving the objectives outlined in the Water Framework and Flood Directives at the European level (2000/60/EC [28] and 2007/60/EC [29]). Moreover, these directives promote the development of proper flood forecasting and monitoring systems, aiming at preventing high socio-economical losses and at planning a variety of flood-management alternatives [91]. Recent studies have demonstrated that estimation of rainfall provided from the Integrated Multi-satellite Retrievals (IMERG) algorithm for the Global Precipitation Measurement constellation coupled with the mesoscale Weather Research Forecasting (WRF) model [77] can be effectively utilized to accomplish these objectives and fulfill the requirements of the directives [37].

In the last decade, advances in remote sensing technologies and the computational ability to process vast datasets are increasing at unprecedented speed and have revolutionized the way we quantify and assess river systems [76], offering new sources of high resolution, multidimensional data across wide spatial scales and at multiple time scales, towards a data-rich geomorphological science [81]. The availability of different satellite imagery, often freely accessible, can be coupled with various cloud computing platforms and distributed systems such as Google Earth Engine (GEE), Sentinel Hub, Open Data Cube, openEO, and others [40].

Satellite images, and in particular the freely available Landsat and Sentinel–2 multi–spectral images, have been successfully used for river mapping since the 1990s [86], with continuous improvements since then, towards the accurate evaluation of channel width [70], river centerline and sinuosity [63], and, more in general, for mapping surface water extent and dynamics [71, 48, 87].

However, approaches based on optical data in the visible and near–infrared range suffer from strong limitations due to the adverse atmospheric conditions that often characterize flood events. Particularly in the case of relatively small catchments (areas smaller than 10^4–10^5km^2), flood peaks occur shortly after rain events, implying that cloud coverage is very likely to persist, reducing the possibility of effectively monitoring large river areas. On the contrary, satellites carrying active radar sensors operating in the microwave range are not affected by cloud coverage and therefore provide an attractive way to remotely track the dynamics of rapidly changing river systems. Indeed, Synthetic Aperture Radar (SAR) has played a crucial role in identifying wet and dry classes due to its ability to provide data regardless of the weather conditions or time of observation. Numerous techniques have been developed to fully exploit the potential of SAR data. In the early studies, flood stage measurement, braided river patterns, and river discharge were manually performed by the operator [13, 85, 64]. More recently, flood monitoring and river morphology assessments are performed by employing the RGB composition of a reference image (e.g., pre-flood) and a target image (e.g., post-flood), followed by a threshold technique such as the seed-growing segmentation, Maximum Likelihood, or K-means [23, 78, 2, 3, 69, 61]. Morphological operators (opening and closing), followed by a K-means thresholding algorithm and a fuzzy logic classifier have been successfully applied to map flooded vegetation [80] and distinguish water surfaces from artifacts caused by heavy precipitation or wet snow [79]. Opening and closing operators, coupled with Support Vector Machine (SVM) [51] and watershed by immersion segmentation [20], are employed, respectively, for extracting river linear features and segmenting the river channel.

However, the application to SAR datasets of fully automated thresholding algorithms, such as the one proposed by Otsu, are still challenging for the scientific community [105, 62]. For example, the target class often covers only a small portion of the overall scene, failing to clearly emerge in the histogram of the entire image. Under these circumstances, parametric methods, which typically necessitate the estimation of probability distribution functions for the two target objects (dry soil and wet area, in our case), are not feasible. In this context, several techniques of image splitting and sub-image bimodality testing come into play [26, 19, 15, 90].

In the last decade, numerous studies have focused on extracting water streams and water bodies using various approaches that utilize deep neural networks [68, 67, 18, 104, 99, 103]. A more detailed description of the aforementioned papers is provided in Section 1.2.

To improve the efficacy of these methods, in this work, we present the development of an unsupervised and cloud-based algorithm for the near-real-time analysis of stack SAR images. In the workflow, which is described in detail in Section 1.3, we accomplish the following objectives:

(i) we incorporate water flow level information through metadata enrichment to facilitate the automatic extraction and monitoring of inundation dynamics at a sub-event temporal scale;

(ii) we evaluate the denoising of speckle using three edge-stopping functions;

(iii) we develop and apply a Self-Adaptive Thresholding Approach (SATA), which is based on the Otsu algorithm.

The algorithm is then tested and verified on a 13 km long reach of the Tagliamento River (Italy), a large, braided gravel bed river, recognized as the most natural and dynamic large river in the European Alps. Furthermore, the availability of imagery at the sub-event time scale, as opposed to the standard before–after-flood approach, allows the observation and quantification of lateral bank erosion and channel dynamics during the flood event and with accurate timing as a function of water level and inundation duration.

The Chapter 1 is organized as follows: Section 1.2 contains a review of the existing methods that allow river-channel segmentation based on SAR data; Section 1.3 presents the theoretical approach and describes the details of the computation steps and the dataset; Section 1.4 illustrates the case study, and Section 1.5 shows the results of mapping river-inundated areas and morphological change during the flood events that occurred from 2018 to 2020. Discussion on perspectives and limitations of the present work, along with the geomorphological significance and main concluding remarks, is provided in Section 1.7.

1.2 Related works

The detection of flood areas, the extraction of water surfaces, and the monitoring of river morphology have a lowest common denominator: the accurate clustering of images. In the existing literature, different approaches can be found, whose complexity also depends on the historical moment in which the research was conducted.

Brakenridge et al. (1994) [13] and Smith et al. (1995) [85] employed a fixed threshold value for clustering ERS-1 imagery. Brakenridge et al. quantified the flood stage by establishing a correlation between the extent of the 1993 flood of the Mississippi River and high-quality topographic data. On the other hand, Smith et al. examined the correlation between multitemporal surface area of water and discharge measurements for a braided glacial river in British Columbia.

Nykanen et al. (1998) [64] classified the connected braided system by first manually selecting the upstream part of a known channel and then selecting the disconnected sections that visually appeared to be part of active channels. After approximately one hour of image reworking, the binary classification was completed. They also attempted to use an Unsupervised Bayesian Classification algorithm in order to fully automate the procedure, but the result was a poorly connected braided channel network.

More recently, Klemenjak et al. [51] presented an algorithm for the automatic extraction of river networks that can be applied to multi-temporal or multi-polarized high-resolution SAR data (TerraSAR-X). The method is implemented using the Support Vector Machine and is based on the supervised classification of morphological profiles. They found that in the presence of bridges or power lines the procedure could produce gaps in the river network. In these cases, the choice of polarization could improve the accuracy of the method.

Amitrano et al. (2015) [1] presented a framework for the treatment of multi-temporal Synthetic Aperture Radar (SAR) images that defines an intermediate product between L1 and L2 named L1–α through the fusion between the intensities of the reference and test images and their coherence into a false-color RGB image. The above-mentioned framework was applied to the assessment of morphological variations due to flood events [61]. The authors also verified the possibility of monitoring water bodies: lakes, wetlands, and rivers. For the case of rivers, water channels were automatically extracted by means of an intensity threshold, whereas active channels and sediment bars were visually outlined. Active channel widening and narrowing were highlighted [69].

Obida et al. (2019) [65] applied the K-means unsupervised methodology to cluster Sentinel–1 data for the purpose of extracting the river network of the Niger delta. Subsequently, the centerline of the river network was extracted and compared with manually derived centerlines from imagery acquired in the visible range.

Moharrami et al. [62] employed a simple Otsu algorithm applied to the histogram of an entire Sentinel–1 image to delineate the flooded areas in North Iran for the extreme event of March 2019. In this case, the estimation of the threshold value is particularly challenging, because the target class typically constitutes only a minor portion of the image, and therefore, the histogram does not exhibit a bimodal distribution.

Furthermore, the use of one single threshold for the entire image is not optimal for large areas because of inherent characteristics of SAR data. The imaging geometry of SAR, such as incidence angle variations, can significantly affect the radar backscatter, causing similar land cover types to exhibit different radar signatures depending on their orientation and the sensor's viewing geometry. This variability complicates the application of a uniform threshold across the image. Below, we explore a range of tiling approaches developed to tackle this specific challenge.

In order to parameterize the distribution functions from the histogram of the two classes (dry soil and water), Chini et al. [19] introduced a Hierarchical

Split-Based Approach (HSBA) to divide the image into tiles, each with an equal proportion of pixels belonging to the two classes of interest. To achieve this, they checked that the histogram was clearly bimodal, and the parametrization of the distribution function performed well. To cluster the image, they applied a Regional Growing (RG) algorithm. The threshold for the seeds and the tolerance criterion to stop the growing process were selected based on the distribution of the target class estimated by HSBA.

Ciecholewski [20] proposed a two-step global threshold approach for segmenting the river channels. Firstly, the polarimetric ALOS PALSAR image is clustered using a watershed using the immersion algorithm. Secondly, in order to reduce over-segmentation, surrounding sub-regions are iteratively merged by maximizing the average contrast. The algorithm was compared with three other approaches: multilevel image thresholding using Otsu's method (Otsu), Fast Random Walker (FRW), and Active Contour Without Edges (ACWE) on a reach of Sungai Kampar River channel.

Cao et al. [15] proposed subdividing the image into tiles of a fixed dimension $s \times s$ and applying the Bimodality Test (BT) to identify the tiles that exhibit a bimodal histogram. The histograms were smoothed using a Gaussian convolution kernel. The mode value of the water portion of the histogram was utilized as the threshold for identifying the core water area. Lastly, a region-growing algorithm (RGA) was employed to generate a spatially homogeneous water map.

Donchyts et al. [26] introduced an extension of non-parametric detection methods, such as the histogram-based Otsu thresholding algorithm. They incorporated the Canny edge filter to identify the edges between water and dry soil and subsequently computed the histogram using the pixels enclosed within an area surrounding those edges. In this particular case, the histogram obtained displayed a distinct bimodal shape, indicating the suitability of the Otsu thresholding algorithm.

Finally, Tan et al. [90] developed a self-adaptive thresholding algorithm, derived from the Otsu approach, for automatic water extraction using Sentinel–1 Synthetic Aperture Radar (SAR) imagery. This algorithm incorporates the side-looking characteristic of SAR data by subdividing the S1 scene into uniform tiles based on the distance to the orbit. The goodness of the classification was evaluated using the Jeffries–Matusita (JM) distance function. Compared to five other traditional segmentation algorithms (Otsu, Moments, Mean, Isodata, and Minerror), the proposed method achieved the highest overall accuracy.

1.3 Material and methods

This work proposes an unsupervised methodology based on the Google Earth Engine cloud infrastructure for the continuous monitoring of river dynamics during flood events using freely available Sentinel–1 imagery. The proposed method utilizes the Level 1 (L1) GRD product of Synthetic Aperture Radar (SAR) imagery acquired from Sentinel–1 in the Interferometric Wide swath (IW) mode. Sentinel–1 is a C–band active sensor operating at a center frequency of 5.405 GHz, which corresponds to a wavelength of ≈ 5.5 cm. The sensor returns images at a pixel spacing of 10 m, and the pixel values typically range between −35 decibels (dB) and slightly positive values. IW product is Sentinel–1's primary operational mode over land, and it is available in dual polarization, namely vertically emitted, vertically received (VV) or vertically emitted, horizontally received (VH). The vertical polarization, interacting with the Earth's surface, can return to the satellite sensor in the vertical plane or in the horizontal one. Before ingesting the imagery into the Engine's database, Google applies the required standard preprocessing to the Sentinel–1 Ground Range Detected (GRD) product. This preprocessing involves updating the orbit information, removing image border noise, modeling the thermal noise, calibrating the images radiometrically, and applying terrain correction.

This work proposes the implementation of a processing chain as follows:

- Enriching the image stack with hydrometric data;
- Applying the radiometric slope correction algorithm;
- Reducing speckle noise;
- Extracting the wet channel with a Self-Adaptive Thresholding Approach (SATA);
- Output functions.

Each function was structured in a main body and sub-functions with the purpose of allowing sequential calls needed from the time series of images.

GEE's architecture is based on a client/server programming model. Under this architecture, the client libraries provide a user-friendly programming environment, recording the computational chain and sending it to the server for the execution. This implies that it is impossible to combine Earth Engine library calls (server side) with local processing operations (client side). The procedure has three points where the client site and server side exchange inputs and outputs: the image query step, the upload of hydrometric data, and the output step, which can save scatter plots, time series of water masks, and data dictionaries (Figure 1.1).

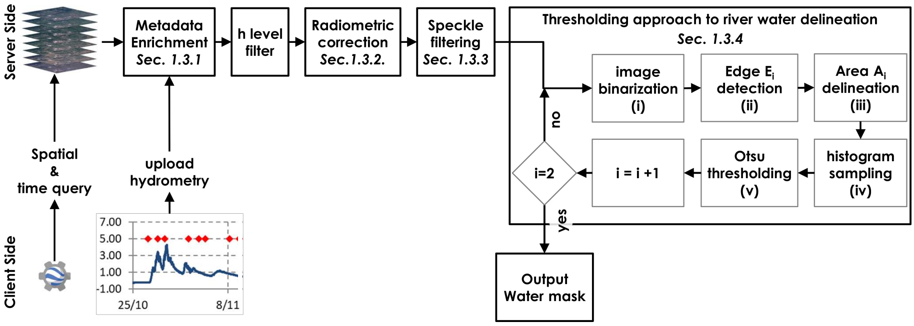

Figure 1.1: *Workflow diagram of the proposed framework for mapping the braided channel area at sub-event time scale using time series of Sentinel–1 imagery (red diamond). The time-varying water level is represented by the blue line.*

Previous research has demonstrated that, in scenarios characterized by non-windy conditions and the absence of stream water, VV polarization exhibits superior accuracy to VH polarization [95]. This is attributed to the sensitivity of VV polarization to water surface roughness. VH is generated from the interaction with the tree crowns (volumetric scattering), and part of the backscatter is redirected towards the water channel, causing misclassification [49]. In our study of large gravel bed rivers without vegetation in the active channel, the rippling water surface impedes the use of VV polarization, thus favoring the adoption of VH polarization.

1.3.1 Image Selection and Metadata Enrichment

Images are selected on the basis of a spatial query of the region of interest and a query of the time interval of the flood event. After the initial image query, the metadata of the images are enriched with the hydrometric level registered at the time of image acquisition. This operation is of utmost importance for subsequent analysis as it allows for the determination of inundation dynamics in conjunction with hydrometric levels. This, in turn, facilitates the inference of the relationship between flooded areas and water discharge.

The water–level time series, composed of the date in a string format and the water level in a decimal floating-point format, are firstly converted into a collection of images and then joined with the SAR image collection. In the present work, the hydrometric data recorded at the Venzone station were used. The gauging station is located approximately 20 km upstream from the studied reach. More details on the management of the station's hydrometric data are provided in Section 1.4. The resulting collection contains paired elements composed of the metadata and all the bands of the primary SAR collection and the matching element from the hydrometric level collection. The matching criterion is time–dependent, and SAR images are associated with the nearest water level value according to the following expression:

$$\text{Pixel} = \begin{cases} h_i & if \;\; t_{SAR} \in [t_i; t_{i+1/2}) \\ h_{i+1} & if \;\; t_{SAR} \in [t_{i+1/2}; t_{i+1}] \end{cases} \tag{1.1}$$

where h_i and h_{i+1} correspond to the water level at time t_i and t_{i+1}, respectively, t_{SAR} is the SAR acquisition time, and $t_{i+1/2} = (t_i + t_{i+1})/2$.

1.3.2 Radiometric Terrain Correction

Due to the side-looking configuration of SAR sensors, there are a number of geometric and radiometric distortions that arise from the 2D imaging processing of the 3D Earth surfaces and are intrinsically linked to the local orientation of the surface, which need correction and reduction. In the ideal case of a flat surface, the distortion is a specific geometric compression of the ground in the slant range, with increasing distortion moving from the furthest to the nearest range area. The conversion of the slant range to ground range is typically performed by the radar processor prior to image creation. This conversion facilitates accurate distance measurements by accounting for the radar geometry [33].

On the other hand, radiometric distortions caused by terrain orography need to be corrected using an analytical approach [98, 96, 60, 57, 42, 46]. Terrain slopes cause significant variations (radiometric distortions) on radar backscatter values, depending on the angle and aspect of the surface and on the radar configuration, in terms of frequency, polarization, and ascending or descending path. Foreshortening, layover, and shadowing can be included among these effects. The first two happen when the slope is facing towards the sensor, while shadowing occurs on the opposite side of the slope. Foreshortening occurs when the slope in the range direction (α_r) is less than the incidence angle (θ_i), whereas layover appears when the slope exceeds the incidence angle. Shading or shadowing of the opposite side of the slope occurs when the angle $\alpha_r > 90^o - \theta_i$.

In applications related to land monitoring, an accurate backscatter measurement has a central role and allows robust land-cover classification. Therefore, radiometric slope correction is needed in order to reduce these topographic effects on backscattering values and to provide imagery in which pixel values are properly related to the radar backscatter of the scene. In the literature, there are different approaches aiming at reducing radiometric distortion.

In this work, two physical models have been taken into account. These models propose an exact solution for the compensation of slope-induced variations in the backscattered energy. Hoekman et al. [43] consider the effects of forested reliefs on the radar backscatter, as an opaque volume composed of isotropic scatterer elements (Equation (1.2)), whereas Ulander et al. [96] derive an equation for the radiometric correction, projecting the 3D model of hillslope without vegetation into the 2D domain of the SAR images and thus considering it as a surface of isotropic scatterers (Equation (1.3)):

$$\gamma_f^0 = \gamma^0 \cdot \frac{\tan(\pi/2 - \theta_i)}{\tan(\pi/2 - \theta_i + \alpha_r)}, \tag{1.2}$$

$$\gamma_f^0 = \gamma^0 \cdot \frac{\cos(\alpha_{az}) \cdot \cos(\pi/2 - \theta_i + \alpha_r)}{\cos(\pi/2 - \theta_i + \alpha_r)}, \tag{1.3}$$

where γ_f^0 and γ^0 are, respectively, the backscatter on a flat terrain and the backscatter on a tilted terrain, α_{az} and α_r are the terrain slope in the azimuth direction and in the range direction. θ_i represents the incidence angle of the SAR signal with the Earth's surface.

1.3.3 Denoising

The goal of this framework step is to reduce the intrinsic noise of Sentinel–1 SAR images, a granular pattern distribution called speckle that affects the SAR images. This effect is due to the sum of constructive and destructive superpositions of the backscattered signal after the interaction with the target area. In general, the task of all despeckling methods is to reduce the speckle noise without losing fine details and edges of features. Among the approaches used for SAR images despeckling, Bayesian methods [54, 55, 34, 59, 8], non-Bayesian algorithms [72, 56, 58], hybrid approaches, and also new methodologies based on machine learning algorithms can be mentioned. Comprehensive recent reviews of these methodologies can be found in [5, 84, 7].

In this work, the non-Bayesian model proposed by Perona and Malik (1990) [72] was used, which is based on the Gaussian kernel convolution and maintains an accurate location of feature edges during the process of image smoothing and restoration, through the following definition of a scale space:

$$\begin{cases} I_t = \Delta\left(c(x, y, t)\nabla I\right) \\ I_{(t=0)} = I_0 \end{cases} \tag{1.4}$$

where $I_t = \partial I/\partial t$ is the partial time derivative of the intensity image, I_0 is the initial intensity image, and Δ and ∇ are divergence and gradient operators, respectively. The diffusion coefficient $c(x, y, t)$ is a function of the gradient magnitude of the image. The primary task of the diffusion coefficient is to prioritize smoothing within a region rather than smoothing across its boundaries. This objective can be accomplished by ensuring that the conduction coefficient is a monotonically decreasing function equal to 1 within the interior of each region and 0 at the boundaries. The setting of the diffusion coefficient function is discussed in the next paragraph.

As noticed by Hummel et al. and Koenderink et al. [45, 52], Gaussian kernel-based methods are equivalent to the solution to the diffusion Equation (Equation (1.4)), which, neglecting the hierarchy of the image levels, reduce both image noise and the definition of object boundaries. With the aim of overcoming these limitations, Perona and Malik [72] defined the diffusion coefficient as a function of the gradient magnitude of the image $c = g(||\nabla I||)$. This function, called the edge stopping function, ensures a higher rate of diffusion within homogeneous regions and avoids the blurring of the feature boundaries characterized by high values of $||\nabla I||$.

Three edge stopping functions were tested. The first two (Equations (1.5) and (1.6)) were proposed by Perona and Malik [72], and the third (Equation (1.7)) was proposed by Black et al. [11]:

$$c_1 = e^{-(||\nabla I||/K)^2}, \tag{1.5}$$

$$c_2 = \frac{1}{1 + (||\nabla I||/K)^2}, \tag{1.6}$$

$$c_3 = \begin{cases} \frac{1}{2}\left[1 - \left(\frac{||\nabla I||}{K\sqrt{2}}\right)^2\right]^2 : ||\nabla I|| \leq K\sqrt{2} \\ 0 : otherwise, \end{cases} \tag{1.7}$$

where $||\nabla I||$ is the gradient magnitude of the image I, and K is a constant parameter that allows for the adjustment of the noise filter. Its value is typically determined through experimental selection or by considering the noise characteristics present in the image. In the present work, it was set to 3. Figure 1.2 illustrates the distinct smoothing effects of the three functions mentioned earlier. The c_1 function stops the diffusion starting from a small gradient value, whereas c_2 needs a higher gradient value in order to stop diffusion. The c_3 function stops the diffusion at low gradient values, preserving very fine details. So c_2 privileges wide regions over small ones, c_1 privileges high contrast edges versus lower-contrast edges, and c_3 reduces the diffusion even more rapidly than c_1 and stops diffusion where the gradient is very low.

The most appropriate edge-stopping function in our case is c_1, as it adequately smooths homogeneous regions while preserving border lines.

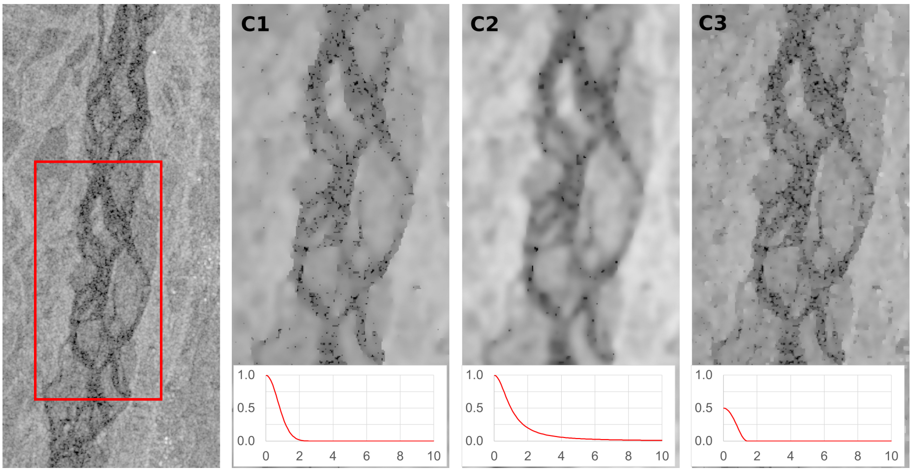

Figure 1.2: *Illustration of the varying smoothing effects of Perona and Malik's model using different edge-stopping functions on Sentinel–1 imagery. From left to right: original VH band, denoised images using Equations (1.5),* (1.6)*, and* (1.7)*. The three denoising functions are plotted in the bottom sub-panels as a function of the gradient magnitude of the image. The x-axis represents the gradient magnitude of I* $\|\nabla I\|$*, while the y-axis represents the value of* $c_{(\|\nabla I\|)}$.

1.3.4 Self-Adaptive Thresholding Approach (SATA) to River Water Delineation

Image segmentation is the process by means of which two or more classes or objects are identified in an image. Various techniques are widely used in research fields such as medical applications, the recognition and tracking of objects, and environmental analysis, including the delineation of river and waterbodies from optical, multispectral and radar data. Two groups can be mentioned: traditional methods (e.g., edge detection, clustering, random forest, support vector machine, Markov random field, statistical algorithm), and segmentation processes based on the latest Deep Learning (DL) methods (ANN, CNN, and others) [41].

As described in the introduction, in our case, the water class covers only a small portion of the entire scene, leading to a unimodal histogram that represents mainly the dry soil class. Such a histogram makes the Otsu thresholding method almost impossible to use. In order to obtain a bimodal distribution that allows the computation of a reliable threshold value, a suitable subset of the image (A_i) is needed. To this end, the proposed SATA is composed of two cycles ($i = 0, 1$) of the following steps (Figure 1.1):

(i) Image binarization process using the threshold value t_i;

(ii) Identification of the wet–dry edges E_i using the Canny Edge filter [14];

(iii) Delineation of the area A_i applying a buffer (B_d) around the edges E_i;

(iv) Histogram sampling within the area A_i;

(v) Evaluation of the threshold t_{i+1} applying the Otsu algorithm.

On the first run ($i = 0$), the threshold t_0 is manually set to −20 dB, representing an initial threshold attempt. After the second run ($i = 1$), the algorithm outputs the final threshold t_2, which is then used to extract the water mask. Figure 1.3 illustrates the conceptual scheme depicting the definition of the edges E_i and the area A_i for the i-th step.

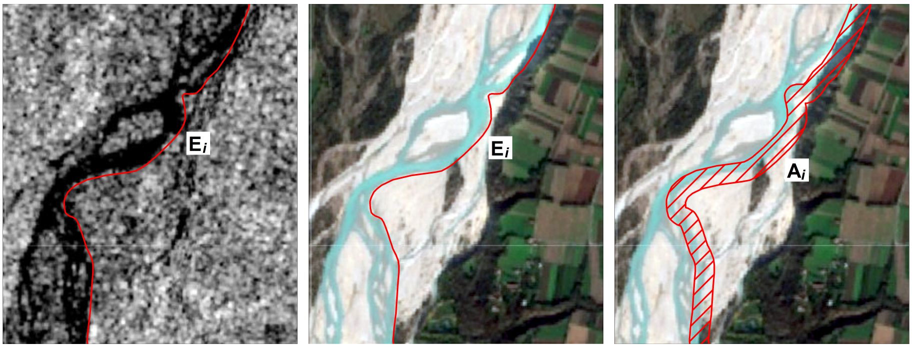

Figure 1.3: *Conceptual scheme illustrating an example of the thresholding algorithm applied to Sentinel–1 data acquired on 17.11.2018. Sentinel–2 imagery is utilized for a visual explanation of the thresholding steps. The first two panels depict the definition of the wet–dry edges, denoted as E_i, based on the threshold t_i. Meanwhile, the right panel illustrates the area A_i generated around these edges with a distance B_d, within which the Otsu algorithm is subsequently applied.*

After binarizing the image using t_i (step i of the procedure), the Canny Edge filter is applied to the resulting binary image (step ii of the procedure). Before the edge-detection step, the image is convolved with a Gaussian filter with the parameter σ set to 1. The edges are subsequently defined as those pixels where the magnitude of the gradient exceeds 1.

The area A_i, where the histogram is sampled, is defined by buffering the edges E_i by a distance B_d (step iii of the procedure). The choice of buffer amplitude B_d is bounded by the channel width. At low discharges, the channel width is narrow, whereas it is wider at high discharges. The optimal buffer amplitude is the one that samples half of its area in the channel and the remaining half on dry land, without including other land classes such as vegetation or urban areas with higher backscatter values. In Section 1.5.1, the impact of the choice of parameters will be presented and analyzed, specifically highlighting that the optimal selection for our specific case is $B_d = 50$ m.

To reduce the computational time and implement an efficient automatic procedure, we selected a thresholding method (step vs. procedure) with low consumption of computational resources, namely the Otsu thresholding algorithm [66], which is simple to implement and has a similar accuracy to more complex methods [50]. The Otsu thresholding algorithm, initially implemented by Donchyts et al. [26], was optimized with the aim of ingesting a stack of images. The algorithm is applied to the decibel (dB) histogram sampled into the area A_i of every SAR image and is based on the maximization of the inter-class variance, defined as

$$\sigma_B^2 = \omega_0 \cdot (\mu_0 - \mu_T)^2 + \omega_1 \cdot (\mu_1 - \mu_T)^2 \tag{1.8}$$

where σ_B^2 is the inter-class variance, ω_0 and ω_1 are the probabilities of class occurrence, μ_0, μ_1 are the class mean levels, and μ_T is the total mean level.

$$\mu_0 = \sum_{i=1}^{t} \frac{i \cdot p_i}{\omega_0}; \tag{1.9}$$

$$\mu_1 = \sum_{i=t+1}^{L} \frac{i \cdot p_i}{\omega_1} \tag{1.10}$$

$$\omega_0 = \sum_{i=1}^{t} p_i; \tag{1.11}$$

$$\omega_1 = \sum_{i=t+1}^{L} p_i; \tag{1.12}$$

where L is the number of levels and p_i is defined as the ratio n_i/N. n_i denotes the number of pixels at level i, and N is the total number of pixels.

As mentioned earlier, the successful application of the Otsu algorithm relies on the presence of a distinct bimodal distribution in the histogram. In the scenario where the edge E_i is placed in areas where portions of the image are occupied mainly by water with a small proportion of dry sediments, A_i will be formed mainly by the water class, resulting in a unimodal histogram (Figure 1.4–A). Similarly, if E_i is placed where mainly dry soil is present, A_i will be formed mainly through dry pixels (Figure 1.4–B). In both cases, the Otsu's thresholding algorithm will yield an unreliable threshold. To avoid this, the proposed SATA takes advantage of the second run to adjust the position of the wet–dry edges E_i until the sampling area A_i includes approximately 50% of pixels from each class (Figure 1.4–C). In Section 1.5.1, we will describe the gradual improvement in the bimodality characteristic of the histogram, which is achieved through two cycles of the procedure. Furthermore, we will report the threshold values and the corresponding relative binary masks for the specific case study.

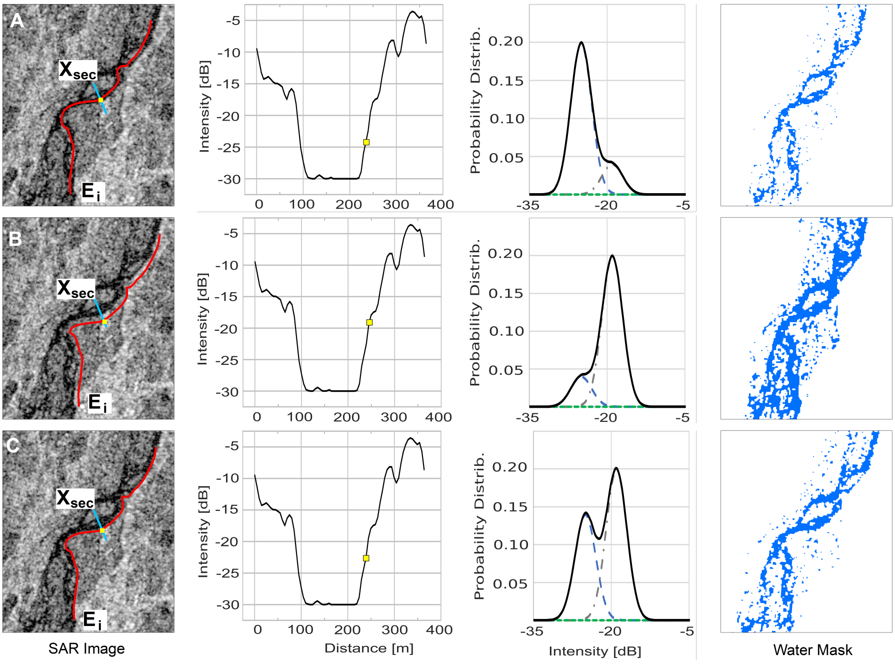

Figure 1.4: *Examples demonstrating the effect of positioning the wet–dry edges E_i on histogram sampling and the resulting water mask. Row (**A**) displays the unimodal histogram generated when the wet–dry edges E_i are positioned in areas of the image predominantly occupied by water, with a small proportion of dry sediments. Conversely, row (**B**) shows the unimodal histogram generated when E_i are placed in areas of the image predominantly occupied by dry sediments. Row (**C**) represents the case when E_i guarantees that the sampling area A_i includes approximately 50% of pixels from each class.*

1.4 Study Case

The proposed algorithm has been applied and tested on the Tagliamento river (north east Italy), a large gravel bed braided river recognized as a reference fluvial system for its near–natural dynamics [94]. Its catchment covers an area of about 2700 km^2 from the Italian Alps to the Adriatic Sea, with a total length of 178 km.

The study focuses on a 13 km long reach located in the foothill area of Friulian Pre-Alps, downstream of the Pinzano gorge (Figure 1.5). It has a mean longitudinal gradient equal to 3.4 m/km and the active channel reaches a width of 1000 m. During flood events, this section of the river shows significant variations in the water surface area, induced by the inundation of lateral channels and sediment bars. The reach is also morphologically active, showing frequent erosion of banks and vegetated islands.

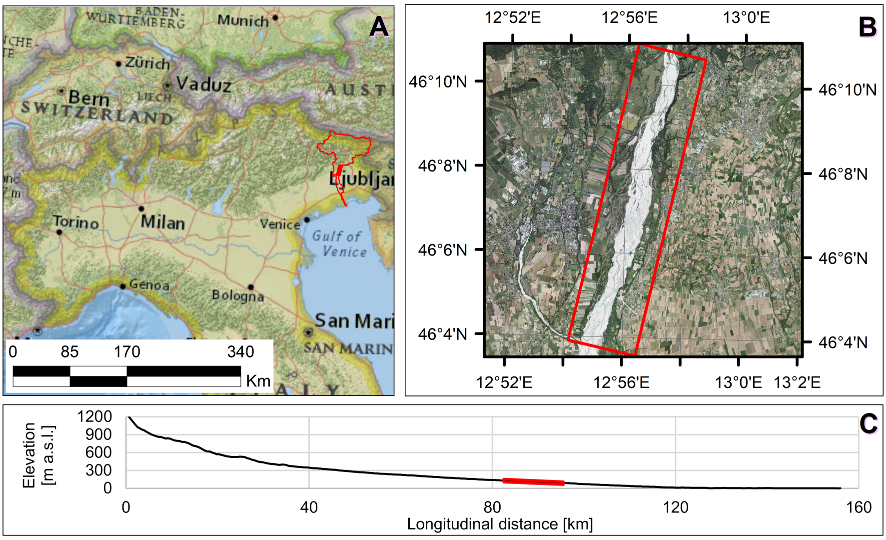

Figure 1.5: *Location of the Tagliamento catchment in north east Italy (frame* **A***) and aerial view of the study site (frame* **B***). Frame (***C***) displays the longitudinal profile of the river bed, with the red box highlighting the investigated reach.*

The hydrologic regime of the Tagliamento river can be classified as a pluvio-nival regime [94]. The snow melt during the spring season (April–June) sustains the discharge (Figure 1.6–A), ensuring a period of significant mobility of the riverbed, particularly when associated with rain events. Major floods generally occur in autumn, when heavy rains are more likely, with humid air masses moving north from the sea.

In the present work, we used data from the hydrometric station in Venzone, about 20 km upstream of the study reach, with a particular focus on the floods that occurred on October 2018, November 2019, and December 2020 (black arrows in Figure 1.6–B). Hydrometric data were shifted back by 1 h with respect to the image timing, to take into account the flood propagation from Venzone to the study reach. The 1 h shift has been evaluated, referring to a second gauging station and approximated hydraulic computations.

The new Digital Elevation Model (DEM) of Italy presented by [92] was used to implement the radiometric terrain correction. The DEM was generated through Delaunay tessellation of a heterogeneous dataset, coming from different Italian public bodies. Its vertical accuracy was assessed on an independent set of control points and, in the region of interest, is less than 2 m, which is considered sufficient for the study objectives. The spatial resolution is compatible with the 10 m pixel size of Sentinel–1 imagery.

The correction of the radiometric distortions was performed using the volumetric model (Equation (1.2)), as suggested by [42, 100], for case studies with predominant agricultural land use.

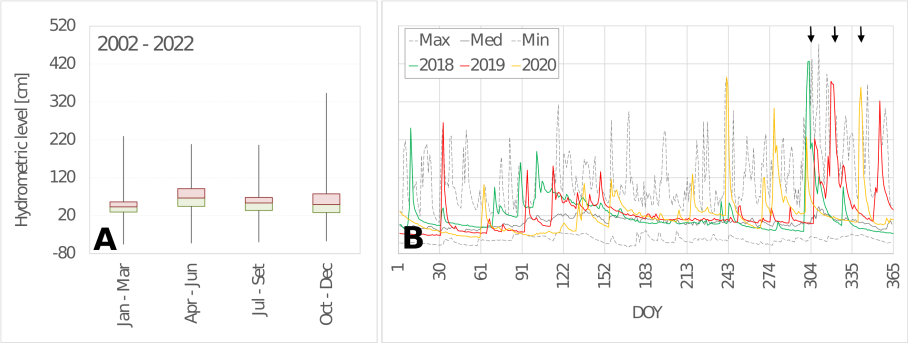

Figure 1.6: *(**A**) seasonal flow variation from 2002 to 2022, and (**B**) flow regime for the years 2018, 2019, and 2020, measured at the Venzone gauging station, aligned by Day Of the Year (DOY). In panel (**B**), the gray solid line and the two gray dashed lines are the median, the maximum, and the minimum value for every single day in the period 2002–2022, respectively.*

1.5 Results

In this section, we start by presenting the sensitivity analysis of the thresholding parameters; then, the calibrated procedure is applied to three flood events in October 2018, November 2019, and December 2020, with return intervals of approximately 10, 4 and 3 years, respectively. In particular, we quantified (i) the area inundated by water as a function of the water level and (ii) the lateral bank erosion rate.

1.5.1 Sensitivity Analysis

Three hundred Sentinel–1 images entirely covering the study reach were analyzed, in the time spans from January 2014 to June 2021. During this period, the hydrometric level at the Venzone gauging station ranged from a low flow up to 4.27 m, which was reached during the flood event named Vaia, which occurred at the end of October 2018. At low flow, particularly during summer, the river bed is often completely dry, due to a natural down-welling process in the huge alluvial sediment deposit [25]. To avoid issues with a completely dry reach, we selected images with a corresponding water level at Venzone larger than 0.25 m.

For each image, the procedure outlined in Section 1.3 and Figure 1.1 was applied, obtaining a classified map of the water surface extension and the estimated value of the threshold t_i that better differentiates between water and dry sediments.

The influence of the buffer amplitude B_d on the threshold t_i was investigated through a sensitivity analysis, varying the buffer amplitude from 50 m to 300 m. The 300 values of t_i were then interpolated using a non-parametric kernel distribution with a Gaussian normal distribution function with mean equal to t_i and a bandwidth of 0.25 dB.

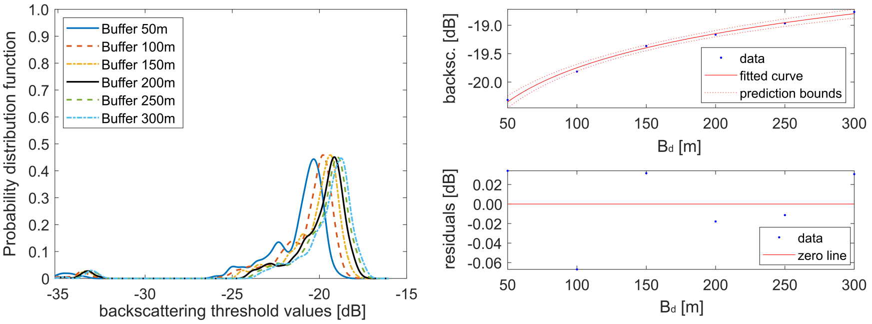

Figure 1.7: *Comparison of the interpolated probability density functions obtained in the six cases, with B_d varying from 50 to 300 m (**left**) and fitting of the most likely threshold values with prediction bounds and residuals (**right**).*

Figure 1.7 shows the effect of increasing the buffer distance from 50 m to 300 m. It is worth pointing out that the active corridor width is about 1000 m, with single channels of the braided network being 50 m to several hundred meters wide. It is therefore reasonable to expect a buffer distance in the proposed range. The comparison between the six probability distribution functions and the fitting curve of the most likely threshold values (Figure 1.7) shows that, for increasing values of the buffer amplitude, the mode shifts towards positive values. This effect is due to the progressive inclusion of pixels representing other land classes, such as vegetation, characterized by volume backscattering, and thus with a stronger backscatter than water and dry sediments. Most probable values of the threshold t_i range between -19 and -20 dB, with a maximum mode difference of about 1.5 dB. A higher value of the threshold results in more pixels classified as water. Differences are, however, limited, in terms of mapping of the main channels. To keep the procedure simple and automated, our suggestion is to select the lower value of the buffer distance to avoid including a significant number of pixels belonging to other land use classes.

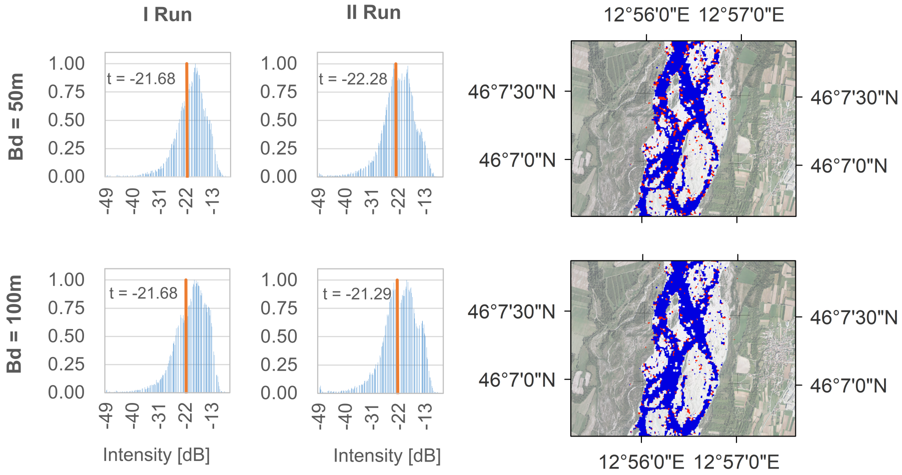

Figure 1.8: *Histograms and the corresponding threshold values obtained after the first and second run of the Otsu thresholding algorithm (first and second column, respectively) in the cases of buffer width* B_d *set to 50 and 100 m (first and second row, respectively). The panels on the right illustrate the classification differences between the first and second run. The red pixels represent areas that changed from being classified as water after the first run to being classified as dry soil after the second run.*

Moreover, the influence of the first value VH_0 was tested for B_d equal to 50 and 100 m, running a second cycle of the thresholding algorithm and imposing the threshold estimate in the first cycle as the initial value. Figure 1.8 shows the histograms of the pixels included in the area A_h with the estimated threshold t_i represented by the red vertical line. The second run shows a better separation of the two classes, with a clearly bimodal distribution. However, the values of the threshold are only slightly different, resulting in an estimated area of the water surface that differs mainly because of sparse, isolated pixels (red pixels in the right panel in Figure 1.8). The histograms in the case of B_d equal to 100 m further confirm that, with a wider buffer it is likely the area A_h that includes a third class of land use (vegetation in this case), represented by the third peak at -14 dB that appears clearly on the right of the histograms after the second run.

In summary, the sensitivity analysis indicated that running the algorithm with a buffer width B_d of 50 m yielded favorable results. Additionally, it confirmed the advantages of using a double cycle approach, as it produced histograms with a more distinct bimodal characteristic and reduced the dependence on the initial VH_0 value.

1.5.2 Inundation Dynamics

The results of the classification of the water surface area for the 300 images from 2014 to 2021 are shown in Figure 1.9, in terms of the proportion of total active corridor area inundated by water as a function of the hydrometric level at the Venzone gauging station. As described in section 1.4, hydrometric data were shifted back by 1 h with respect to the image timing, to take into account the flood propagation from Venzone to the study reach.

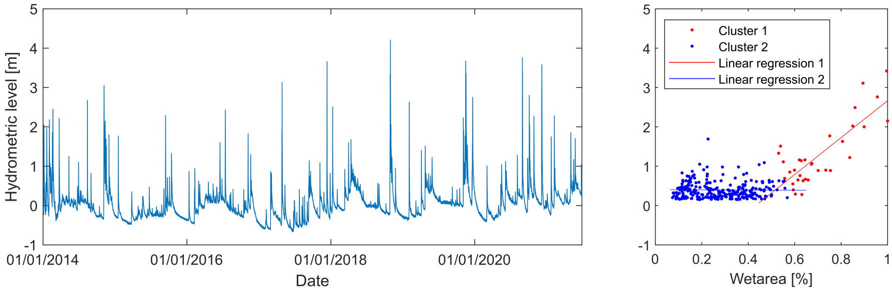

Figure 1.9: *(**A**) Water level recorded at the gauging station of Venzone from 2014 to 2021; (**B**) wet area proportion for the 300 analyzed images.*

Figure 1.9 shows two distinct behaviors: (i) for a water level between 0.25 m and 1 m (blue points), the proportion of wet areas increases markedly from 20% to 60%; (ii) for a water level higher than 1 m (red points) the proportion of wet areas increases less rapidly, reaching 100%, i.e., full inundation of the active corridor, for a water level of about 3 m. At flow levels lower than 1 m, the number of channels increases significantly, with the activation of lateral channels and submergence of low bars. For higher water levels, channels start to merge, and the higher bars and vegetated islands are submerged. The values observed from this analysis are similar to what has been observed on shorter reaches by [97, 101], who used field surveys and fixed cameras. The large variability of the blue points in Figure

1.9–B shows that, particularly at low flow, the channel network configuration may change not only in terms of the location of the channel, but also in terms of the total wet area.

The potentiality of the SAR images mapping is well expressed by the analysis at the single flood scale, for the events in the October 2018, November 2019, and December 2020. Figure 1.10 shows the hydrographs (blue line) registered at the Venzone gauging station and the corresponding time evolution of wet area proportion evaluated at the reach scale (magenta line), for the three events. At the top of each panel, the red points show the acquisition time of the SAR Sentinel–1 images, whereas green points show the available multi-spectral Sentinel–2 images, highlighting the impossibility of evaluating the during-flood dynamics with this passive sensor.

The analysis shows that in all three events, the entire active corridor was inundated (values of the wet area have a proportion up to 1). Moreover, despite the observed changes in the local configuration of the channel network, the analysis shows little variations in the wet area's proportion before and after the flood, indicating a sort of equilibrium at the reach scale.

Figure 1.11 reports with more details the inundation dynamics observed during the event in 2019. November 2019 was a very rainy month, with high flows occurring during the entire month, and five subsequent peaks, with the highest reaching more than 3.5 m. The first five panels show 5 of the 14 classified SAR images for this month, with water level ranging from 0.31 m to 3.29 m. The images help to visualize the increase in the wet area for higher values of the flow level. Moreover, the classified maps show the changes in the channel network before and after the flood, with several channels formed/closed at high flow. The red box in the bottom-left part of the reach highlights a local example of lateral bank erosion. To better observe the morphological changes, a zoomed-in image in the red box is reported in the right panel of Figure 1.11, with the channel location before the flood mapped in blue and the channel after the flood in red. Bank erosion occurred along 340 m, with an average retreat of about 130 m.

The high temporal resolution of the Sentinel–1 images allows a detailed investigation of the processes of bank erosion. In Figure 1.12, the time evolution of the cumulative bank erosion (in red) and the erosion velocity (in green) are reported, compared to the flow level (in blue). The analysis shows no erosion during the first three smaller floods, with the bank retreat starting during the major peak. In this phase, the bank was eroded at a rate larger than 1 m/h. The erosion continued for several days, with a rate of tens of cm per hour, even if the flow level decreased to values lower than those of the first three floods. These observations support previous studies, pointing out the role of major floods and bank saturation for the initiation of bank erosion [82].

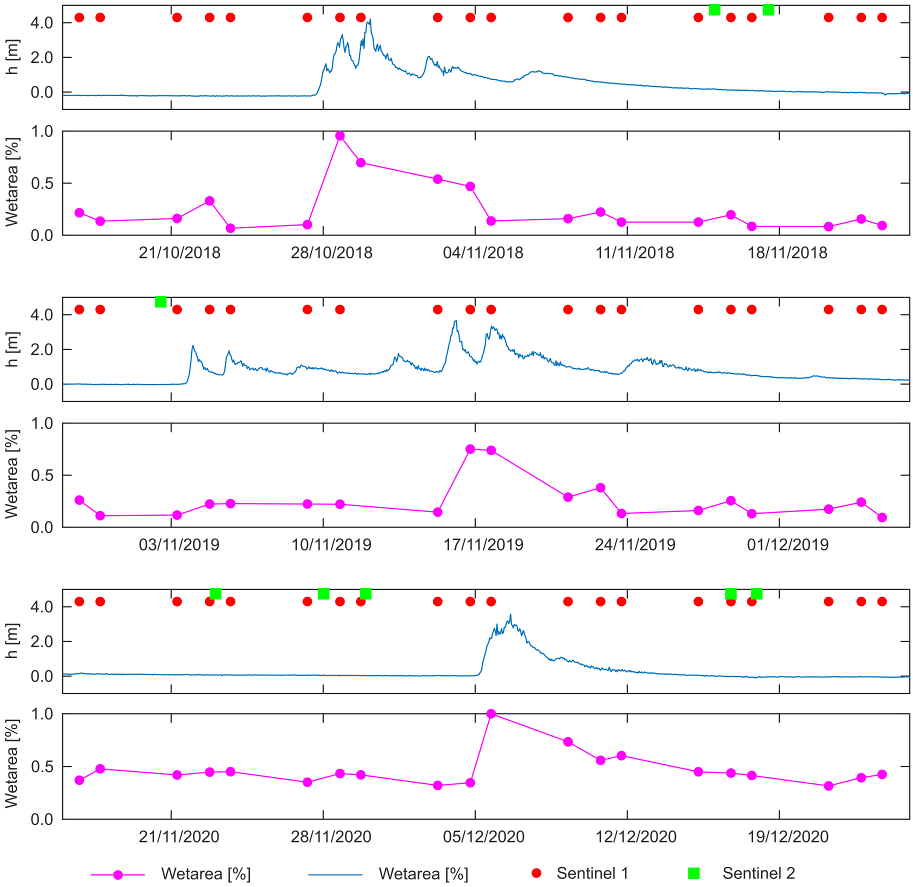

Figure 1.10: *Temporal evolution of water level (blue line) and the corresponding proportion of wet area (magenta line) for the three floods in October 2018, November 2019, and December 2020 (top to bottom panels, respectively). Red dots are the available Sentinel–1 images and the green dots are the Sentinel–2 available images with cloud cover less than 15%.*

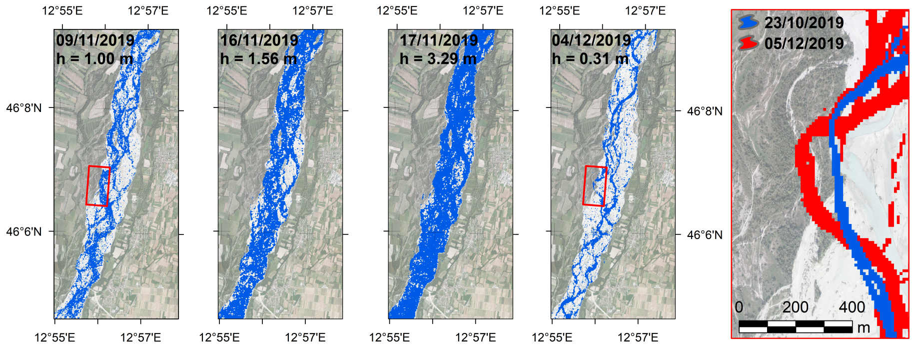

Figure 1.11: *Maps of the estimated wet area during the floods in November 2019, for different values of the water level. The red box locates a major lateral bank erosion event highlighted in the last panel on the right.*

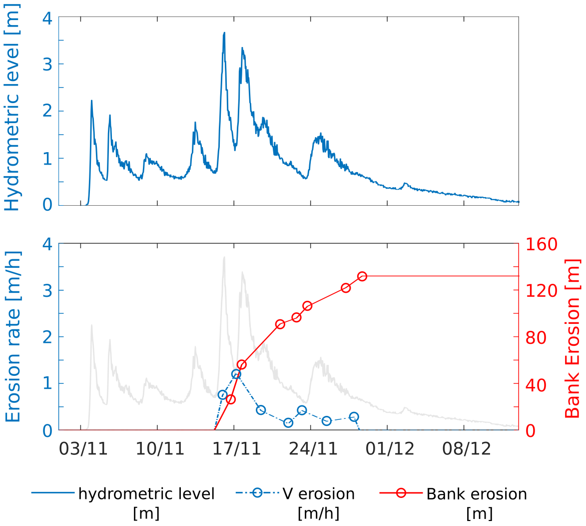

Figure 1.12: *Time evolution of the cumulative lateral erosion (red line) and erosion rate (green line), compared to the flow level measured at the Venzone gauging station (blue line).*

1.6 Discussion

1.6.1 Potential Implications for Fluvial Geomorphology and River Management

The framework was tested on a 13 km long section of the Tagliamento River, a large and dynamic gravel bed river, where significant changes in the channel network occur frequently. This gave us the opportunity to test the advantages of SAR data to investigate river dynamics at the sub-flood temporal scale. Indeed, SAR imagery is not affected by cloud cover, and this is a foremost advantage when considering flood dynamics. Figure 1.10 shows the significant difference in usable images considering Sentinel–1 and Sentinel–2 missions, with the latter negatively affected by clouds. Multi-spectral Sentinel–2 imagery provides only before–after flood mapping, rarely allowing for detailed monitoring during floods.

The application was successful in computing the relation between the proportion of the wet area in the active channel and flow level, using 300 images over a period of 7 years. Similar analysis on close-by reaches made in the past [97, 101] involved time-consuming field measurements and the installation of fixed cameras to overcome the lack of remotely sensed imagery at a high flow. The possibility of easily extending this application to other reaches on the same river and in other catchments opens up new perspectives for river managers, as it provides the opportunity to assess changes caused by human intervention or by natural processes, in both the inundation dynamics and temporal evolution of the morphology.

From a management perspective, the proposed method has a twofold relevance for both environmental protection and hydraulic risk mitigation. Indeed, the relationship between the time-varying wet area and the river flood stage can be considered as a proxy for assessing the availability and temporal dynamics of aquatic habitats in the target reach. This is particularly relevant in braided or multi-thread rivers, where habitat evaluation with standard, field-based methods still poses relevant challenges [30]. Information made available through the proposed method can support decision-making processes associated with ecological flow design because it readily quantifies the maximum possible spatial extent of aquatic available habitat under a broad set of flow conditions.

Furthermore, its capability to provide high temporal resolution information on channel inundation during floods can have a positive impact on the flood risk management plan. Indeed, within the conceptual framework of the flood disaster cycle (Fig. 1.13), numerous actions can significantly benefit from the proposed methodology. In the post–flood event phase, the proposed algorithm, once appropriately implemented to address the presence of other types of coverage such as urban areas and vegetation, can assist in hazard assessment. This, in turn, helps identify the elements exposed to the flood, allowing for an evaluation of the overall risk associated with that event. Within the prevention and mitigation phase, the updates of flood hazard maps, along with the analysis of past events, play a central role. The dynamics of floods and their corresponding extents, captured using SAR data, can be useful both for validating bidimensional numerical models and for delineating Areas with a Potential Significant Flood Risk (APSFR) [29]. In conclusion, in the global context of increasing anthropogenic stressors on river systems at multiple scales [9], as well as the rising impact of climate stressors that can influence flood frequency, duration, and intensity, the proposed algorithm can be critical in disentangling those relations. It is particularly valuable during periods when other remote sensing sources may be limited, especially during flood events.

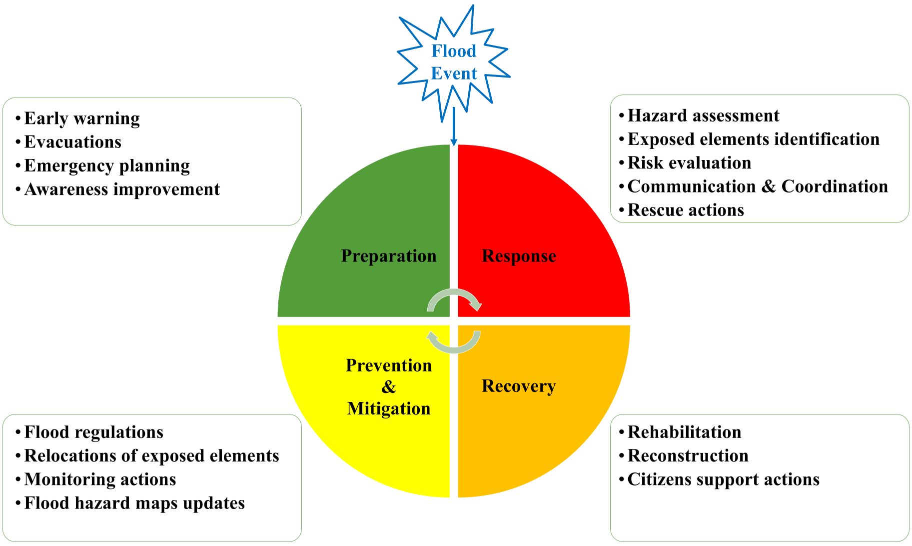

Figure 1.13: *Flood Risk Management Cycle. Overview of Key Actions Across the Four Phases of Management.*

Furthermore, the proposed mapping procedure proved valid in quantifying river bank erosion rates at the scale of single floods. Bank erosion is a relevant morphological process that affects river evolution and ecology [32]. Predicting and modeling river bank erosion is a challenging task because it strongly depends on local effects as well as a combination of hydraulic and geotechnical processes of the river and the bank itself, including the root reinforcement in the presence of riparian vegetation. To improve our ability to model this process, more observations and quantitative data are essential. Recently, [53] proposed a global inventory of riverbank erosion, based on Landsat imagery of the last 20 years, confirming channel width as the main control but also highlighting large variability among rivers. Our application showed that SAR data can be successfully used to quantify riverbank erosion at the event scale, producing valuable information on the erosion rate at a daily scale, compared to the monthly/yearly scale of previous remote sensing applications. This allowed for an accurate evaluation of when the bank erosion process started, as well as the relationship with the flow level and its variations in time. Similarly to what has been discussed for the mapping of wet areas, the proposed procedure has the potential to detect bank erosion events at a much finer temporal scale, providing highly valuable data for river management but also for the calibration and validation of morphological numerical models. These observations can help with understanding the response of rivers with complex morphology to climate and anthropogenic stressors, quantifying the lateral shift of channels and their morphological dynamics.

This algorithm is focused on the analysis at the flood-event time scale, while the river management shall also consider longer-term effects. It is known that the river morphology can be heavily modified because of anthropogenic stressors and also due to climate variability. Despite the possibility of extracting multi annual time-series of the wet area also covering flood events for the same reach, the application of our algorithm can also provide relevant information at those longer time scales.

1.6.2 Advantages, Limitations, and Further Development of the Proposed Procedure

This work introduces an unsupervised, cloud-based algorithm developed using the Python API of Google Earth Engine, enabling the automatic detection of river flood dynamics and associated morphological evolution from a Sentinel–1 image stack. As recently pointed out by [12], GEE is a computing platform that can help geomorphologists (and other scientists) using huge amounts of spatially and temporally rich data (in the order of petabytes), overcoming the limitations caused by computing and data storage costs. Remote sensing data significantly transformed fluvial geomorphology in the last decade [76], with most applications involving multi-spectral passive aerial or satellite imagery [10]. Active SAR satellite data such as Sentinel–1 imagery have been demonstrated to provide a valuable asset to map inundated areas [21, 65, 102], with high accuracy of the water mapping when compared to other sources.

Our investigation confirms the potential of this technique and shows that an unsupervised, cloud-based algorithm produces accurate results, with limited need for parameter calibration. In particular, the analysis pointed out the effect of the buffer distance from the estimated edges B_d and of the starting value of the backscattering threshold VH_0 needed to compute the initial wet–dry edges. We showed that a relatively small buffer width (compared to the channel width) seems more appropriate to avoid including other land classes in the area of interest where the histograms will be produced. Furthermore, through the sensitivity analysis, we demonstrated that, with a second cycle of the Otsu function [66], and with the first computed threshold as starting point for the second run, we can increase the accuracy of the model, making the threshold value independent of the initial attempt value VH_0 and producing a more clearly bimodal histogram. In this way, the selected Otsu thresholding algorithm is most efficient. However, differences are not large, and a cost/benefit analysis depends on the objectives of the study. Our approach extends the method proposed by Donchyts et al. [26] and differs from those presented by Chini et al. [19], Cao et al. [15], and Tan et al. [90]. Indeed, after the tiling process of the images, their methods need to identify the tiles that are more suitable for evaluating the threshold. This was achieved by applying methods such as the Jeffries–Matusita (JM) distance function [88], the Bimodality Test (BT) [24], and the KMM algorithm proposed by Ashman [6]. The self-adaptive Otsu algorithm proposed in this paper adjusts the sampling area in such a way that the number of wet pixels is approximately equal to the number of dry pixels. Therefore, the method does not require a bimodality check of the histogram.

Moreover, the proposed procedure is designed to enrich the imagery metadata through flow levels at the time of image acquisition. Wherever such flow data are available, the GEE procedure automatically extracts images above, below, or in between the defined thresholds, allowing for correlations to be established between the wet area and flow rate and last but not least significantly reducing the computation time and the operator intervention. This approach can be also applied to other fields of research. Integrating data coming from the near-daily monitoring of river surface temperature (RST) using satellite-based observations could provide valuable support for analyzing the impact of climate change on rivers [44], the study of the interaction between hydro-thermopeaking downstream the hydropower plants and summer heatwaves [31], and the improvement in the quality monitoring of river water [89].

As described in Section 1.3.3, the value of K was set manually at a fixed value. However, an alternative approach suggests choosing K based on the estimation of the noise level present in the image. As highlighted by Singh et al. [84], the distribution that best represents the statistical distribution of speckle noise in SAR images is a generalized Gamma probability distribution [47, 27]. We propose modifying the fixed–value approach by considering K as a function of the variance of the generalized Gamma distribution function.

The planimetric output for the flooded areas exhibits jaggedness as a result of speckling in SAR data caused by both existing vegetation and water motion, which creates a rippling effect on the water surface. Despite the application of denoising operations, the inherent variability of the backscatter signal has made it challenging to achieve continuous classification, thereby posing a challenge for future development of the methodology. The uncertainty in SAR–based flood mapping related to the speckle phenomenon has been addressed in many studies [38, 17]. The methodologies that address this issue range from denoising approaches in the preprocessing phase to complex and computationally intensive clustering techniques. Another technique that can help reduce fragmentation in water classification without loss of performance is regional growing (RG). As outlined in [39], this method enhances the accuracy of water body delineation by expanding recognized water pixels into adjacent areas through an iterative sequence of thresholding and region growing until a given tolerance level is reached.

Furthermore, another element of uncertainty in the delineation of flooded areas is related to the presence in silico of nearby dense canopy cover that induces a higher frequency of misclassification. This is due to the interaction of the C-band SAR signal with the treetops, which prevents the signal from reaching the water's surface [16]. As outlined by Pierdicca et al. [75], coupling SAR data with different wavelengths, C-band and L-band, has the potential to enhance the accuracy and robustness of the flood area delineation process.

Another element that influences the accuracy and robustness of the water surface delineation, while also reducing planimetric fragmentation of the braided river network, is the ground resolution of the SAR data. Sentinel–1 images, with a ground resolution of 5 m × 20 m and pixel spacing of 10 m × 10 m, limit the application to rivers larger than a few hundred meters, thereby excluding channels smaller than pixel size. Higher ground-resolution satellites already exist (e.g., COSMO SkyMed and ICEYE) although they are not easily available as Sentinel–1. In Chapter 2, an application involving the detection of wet channels, followed by a subsequent analysis of morphometric indices using COSMO-SkyMed imagery, is described.

The rapidly increasing number of satellite missions, along with technological improvements that enable the swift publication of acquired images, will soon provide imagery at meter or sub-meter resolution. This opens the possibility of integrating data from multiple missions and achieving sub-daily monitoring of river dynamics during flood events.

Currently, the processing chain is implemented for the VH band of Sentinel–1 data. With the aim of enhancing the accuracy and robustness of the flood area delineation process, the two bands VH and VV may be coupled within the processing chain.

The current process requires minimal computational effort, enabling the analysis of 15–20 images of a flood event within a few minutes.

1.7 Conclusions

The study introduces an unsupervised and cloud–based algorithm developed on the platform of Google Earth Engine (GEE), and based on the time series of Sentinel–1 SAR data. The algorithm introduces a novel feature: a Self-Adaptive Thresholding Approach based on the Otsu methodology. This feature dynamically adjusts the threshold value for each Synthetic Aperture Radar (SAR) image, facilitating the extraction of a more reliable channel pattern. The proposed algorithm (i) enriches the image stack metadata with water level values, (ii) applyes the radiometric slope correction algorithm, (iii) reduces speckle noise using the Perona Malick model, (iv) extracts the wet channel pattern with a Self-Adaptive Thresholding Approach (SATA).

The algorithm underwent testing over a 13 km section of the Tagliamento River, showcasing the benefits of utilizing Synthetic Aperture Radar (SAR) data for analyzing river dynamics during flood conditions. Unlike optical data affected by clouds, SAR imagery provides continuous flood observations.

The method allowed for successful correlation wet area proportion in the active channel with flow levels, using Sentinel–1 SAR data spanning seven years, avoiding the limitations of optical or multispectral sensors. This approach offers essential insights to river managers for evaluating changes attributed to natural processes and anthropogenic stressors. It provides support, offering high temporal resolution data on channel inundation dynamics during floods, for designing flood risk management measures. Additionally, it supplies information on channel morphodynamics related to flow variations, aiding in the planning of hydro-ecological river restorations.

The system enabled the quantitative evaluation of riverbank erosion on a finer temporal scale following the 2019 flood event, providing valuable information for understanding river responses to flooding.

Future advancements involve integrating different SAR wavelengths and higher-resolution satellites for more comprehensive flood monitoring.

References

[1] Donato Amitrano, Gerardo Di Martino, Antonio Iodice, Daniele Riccio, and Giuseppe Ruello. A new framework for sar multitemporal data rgb representation: Rationale and products. *IEEE Transactions on Geoscience and Remote Sensing*, 53:117–133, 2015. doi: 10.1109/TGRS.2014.2318997.

[2] Donato Amitrano, Gerardo Di Martino, Antonio Iodice, Daniele Riccio, and Giuseppe Ruello. An end-user-oriented framework for the classification of multitemporal sar images. *International Journal of Remote Sensing*, 37:248–261, 2016. doi: 10.1080/01431161.2015.1125550.

[3] Donato Amitrano, Gerardo Di Martino, Antonio Iodice, Daniele Riccio, and Giuseppe Ruello. Unsupervised rapid flood mapping using sentinel-1 grd sar images. *IEEE Transactions on Geoscience and Remote Sensing*, 56(6):3290–3299, 2018. doi: 10.1109/TGRS.2018.2797536.

[4] Elizabeth P. Anderson, Sue Jackson, Rebecca E. Tharme, Michael Douglas, Joseph E. Flotemersch, Margreet Zwarteveen, Chicu Lokgariwar, Mariana Montoya, Alaka Wali, Gail T. Tipa, Timothy D. Jardine, Julian D. Olden, Lin Cheng, John Conallin, Barbara Cosens, Chris Dickens, Dustin Garrick, David Groenfeldt, Jane Kabogo, Dirk J. Roux, Albert Ruhi, and Angela H. Arthington. Understanding rivers and their social relations: A critical step to advance environmental water management. *WIREs Water*, 6(6):1–21, 2019. ISSN 2049-1948. doi: 10.1002/wat2.1381.

[5] Fabrizio Argenti, Alessandro Lapini, Tiziano Bianchi, and Luciano Alparone. A tutorial on speckle reduction in synthetic aperture radar images. *IEEE Geoscience and Remote Sensing Magazine*, 1:6–35, 2013. doi: 10.1109/MGRS.2013.2277512.

[6] Keith Ashman, Christina Marie Bird, and Stephen E. Zepf. Detecting bimodality in astronomical datasets. *arXiv: Astrophysics*, 1994.

[7] Satyakam Baraha, Ajit Kumar Sahoo, and Sowjanya Modalavalasa. A systematic review on recent developments in nonlocal and variational methods for sar image despeckling. *Signal Processing*, 196:108521, 2022. doi: https://doi.org/10.1016/j.sigpro.2022.108521.

[8] A. Baraldi and F. Parmiggiani. A refined gamma map sar speckle filter with improved geometrical adaptivity. *IEEE Transactions on Geoscience and Remote Sensing*, 33:1245–1257, 1995. doi: 10.1109/36.469489.

[9] Jim Best. Anthropogenic stresses on the world's big rivers. *Nature Geoscience*, 12:7–21, 2019. doi: 10.1038/s41561-018-0262-x.

[10] S. Bizzi, L. Demarchi, R.C Grabowski, C. J. Weissteiner, and W. Van de Bund. The use of remote sensing to characterise hydromorphological properties of european rivers. *Aquatic Sciences*, 78(1):57–70, 2016. doi: 10.1007/s00027-015-0430-7. URL `https://link.springer.com/article/10.1007/s00027-015-0430-7#citeas`.

[11] M.J. Black, G. Sapiro, D.H. Marimont, and D. Heeger. Robust anisotropic diffusion. *IEEE Transactions on Image Processing*, 7:421–432, 1998. doi: 10.1109/83.661192.

[12] R. J. Boothroyd, R. D. Williams, T. B. Hoey, B. Barrett, and O. A. Prasojo. Applications of google earth engine in fluvial geomorphology for detecting river channel change. *WIREs Water*, 8(1):e21496, 2021. doi: https://doi.org/10.1002/wat2.1496. URL `https://wires.onlinelibrary.wiley.com/doi/abs/10.1002/wat2.1496`.

[13] G. Robert Brakenridge, James Clinton Knox, Earnest D. Paylor, and Francis J. Magilligan. Radar remote sensing aids study of the great flood of 1993. *Eos, Transactions American Geophysical Union*, 75:521–527, 1994. doi: 10.1029/EO075I045P00521.

[14] John Canny. A computational approach to edge detection. *IEEE Transactions on Pattern Analysis and Machine Intelligence*, PAMI-8:679–698, 1986. doi: 10.1109/TPAMI.1986.4767851.

[15] Han Cao, Hong Zhang, Chao Wang, and Bo Zhang. Operational flood detection using sentinel-1 sar data over large areas. *Water*, 11(4), 2019. doi: 10.3390/w11040786.

[16] Bruce Chapman, Kyle McDonald, Masanobu Shimada, Ake Rosenqvist, Ronny Schroeder, and Laura Hess. Mapping regional inundation with spaceborne l-band sar. *Remote Sensing*, 7(5):5440–5470, 2015. doi: 10.3390/rs70505440.

[17] Manel Chehibi, Ahlem Ferchichi, and Imed Riadh Farah. Representing and modeling spatio-temporal uncertainty using belief function theory in flood extent mapping. *Expert Systems with Applications*, 209:118212, 2022. doi: https://doi.org/10.1016/j.eswa.2022.118212.

[18] Lifu Chen, Peng Zhang, Jin Xing, Zhenhong Li, Xuemin Xing, and Zhihui Yuan. A multi-scale deep neural network for water detection from sar images in the mountainous areas. *Remote Sensing*, 12, 2020. doi: 10.3390/rs12193205.

[19] Marco Chini, Renaud Hostache, Laura Giustarini, and Patrick Matgen. A hierarchical split-based approach for parametric thresholding of sar images: Flood inundation as a test case. *IEEE Transactions on Geoscience and Remote Sensing*, 55(12):6975–6988, 2017. doi: 10.1109/TGRS.2017.2737664.

[20] Marcin Ciecholewski. River channel segmentation in polarimetric sar images: Watershed transform combined with average contrast maximisation. *Expert Systems with Applications*, 82:196–215, 2017. doi: https://doi.org/10.1016/j.eswa.2017.04.018.

[21] M.A. Clement, C.G. Kilsby, and P. Moore. Multi-temporal synthetic aperture radar flood mapping using change detection. *Journal of Flood Risk Management*, 11(2):152–168, 2018. doi: https://doi.org/10.1111/jfr3.12303. URL `https://onlinelibrary.wiley.com/doi/abs/10.1111/jfr3.12303`.

[22] Dov Corenblit, Eric Tabacchi, Johannes Steiger, and Angela M. Gurnell. Reciprocal interactions and adjustments between fluvial landforms and vegetation dynamics in river corridors: A review of complementary approaches. *Earth-Science Reviews*, 84(1):56–86, 2007. ISSN 0012-8252. doi: https://doi.org/10.1016/j.earscirev.2007.05.004. URL `https://www.sciencedirect.com/science/article/pii/S0012825207000682`.

[23] Silvana Dellepiane, Elena Angiati, and Gianni Vernazza. Processing and segmentation of cosmo-skymed images for flood monitoring. In *2010 IEEE International Geoscience and Remote Sensing Symposium*, pages 4807–4810. IEEE, 2010. doi: 10.1109/IGARSS.2010.5653960.

[24] Omer Demirkaya and Musa H. Asyali. Determination of image bimodality thresholds for different intensity distributions. *Signal Processing: Image Communication*, 19:507–516, 2004. doi: https://doi.org/10.1016/j.image.2004.04.002.

[25] M. Doering, U. Uehlinger, A. Rotach, D. R. Schlaepfer, and K. Tockner. Ecosystem expansion and contraction dynamics along a large alpine alluvial corridor (tagliamento river, northeast italy). *Earth Surface Processes and Landforms*, 32(11):1693–1704, 2007. doi: https://doi.org/10.1002/esp.1594.

[26] Gennadii Donchyts, Jaap Schellekens, Hessel Winsemius, Elmar Eisemann, and Nick Van de Giesen. A 30 m resolution surface water mask including estimation of positional and thematic differences using landsat 8, srtm and openstreetmap: A case study in the murray-darling basin, australia. *Remote Sensing*, 8, 2016. doi: 10.3390/rs8050386.

[27] Hector M. Escamilla and Eugenio R. Méndez. Speckle statistics from gamma-distributed random-phase screens. *Journal of The Optical Society of America A-optics Image Science and Vision*, 8:1929–1935, 1991. doi: 10.1364/JOSAA.8.001929.

[28] European Commission. Water framework directive, 2000. `https://eur-lex.europa.eu/eli/dir/2000/60/oj`.

[29] European Commission. Flood directive, 2007. `https://eur-lex.europa.eu/eli/dir/2007/60/oj`.

[30] David Farò, Katharina Baumgartner, Paolo Vezza, and Guido Zolezzi. A novel unsupervised method for assessing mesoscale river habitat structure and suitability from 2d hydraulic models in gravel-bed rivers. *Ecohydrology*, 15(7):e2452, 2022. doi: https://doi.org/10.1002/eco.2452.

[31] Meili Feng, Guido Zolezzi, and Martin Pusch. Effects of thermopeaking on the thermal response of alpine river systems to heatwaves. *Science of The Total Environment*, 612:1266–1275, 2018. doi: https://doi.org/10.1016/j.scitotenv.2017.09.042.

[32] Joan L. Florsheim, Jeffrey F. Mount, and Anne Chin. Bank Erosion as a Desirable Attribute of Rivers. *BioScience*, 58(6):519–529, 2008. ISSN 0006-3568. doi: 10.1641/B580608. URL `https://doi.org/10.1641/B580608`.

[33] A. Freeman. Sar calibration: an overview. *IEEE Transactions on Geoscience and Remote Sensing*, 30(6):1107–1121, 1992. doi: 10.1109/36.193786.

[34] Victor S. Frost, Josephine Abbott Stiles, K. S. Shanmugan, and Julian C. Holtzman. A model for radar images and its application to adaptive digital filtering of multiplicative noise. *IEEE Transactions on Pattern Analysis and Machine Intelligence*, PAMI-4:157–166, 1982. doi: 10.1109/TPAMI.1982.4767223.

[35] Kirstie A. Fryiers and Gary J. Brierley. *Geomorphic Analysis of River Systems*, pages 1–345. John Wiley and Sons, Ltd, 2012. ISBN 9781118305454. doi: https://doi.org/10.1002/9781118305454. URL `https://onlinelibrary.wiley.com/doi/abs/10.1002`.

[36] Kirstie A Fryirs. River sensitivity: a lost foundation concept in fluvial geomorphology. *Earth Surface Processes and Landforms*, 42(1):55–70, 2017. doi: https://doi.org/10.1002/esp.3940. URL `https://onlinelibrary.wiley.com/doi/abs/10.1002/esp.3940`.

[37] Christos Giannaros, Stavros Dafis, Stefanos Stefanidis, Theodore Giannaros, Ioannis Koletsis, and Christina Oikonomou. Hydrometeorological analysis

of a flash flood event in an ungauged mediterranean watershed under an operational forecasting and monitoring context. *Meteorological Applications*, 29, 2022. doi: 10.1002/met.2079.

[38] L. Giustarini, H. Vernieuwe, J. Verwaeren, M. Chini, R. Hostache, P. Matgen, N.E.C. Verhoest, and B. De Baets. Accounting for image uncertainty in sar-based flood mapping. *International Journal of Applied Earth Observation and Geoinformation*, 34:70–77, 2015. doi: https://doi.org/10.1016/j.jag.2014.06.017.

[39] Laura Giustarini, Renaud Hostache, Patrick Matgen, Guy J.-P. Schumann, Paul D. Bates, and David C. Mason. A change detection approach to flood mapping in urban areas using terrasar-x. *IEEE Transactions on Geoscience and Remote Sensing*, 51(4):2417–2430, 2013. doi: 10.1109/TGRS.2012.2210901.

[40] Vitor C. F. Gomes, Gilberto R. Queiroz, and Karine R. Ferreira. An overview of platforms for big earth observation data management and analysis. *Remote Sensing*, 12, 2020. doi: 10.3390/rs12081253.

[41] Zhishun Guo, Lin Wu, Yabo Huang, Zhengwei Guo, Jianhui Zhao, and Ning Li. Water-body segmentation for sar images: Past, current, and future. *Remote Sensing*, 14, 2022. doi: 10.3390/rs14071752.

[42] D.H. Hoekman and Johannes Reiche. Multi-model radiometric slope correction of sar images of complex terrain using a two-stage semi-empirical approach. *Remote Sensing of Environment*, 156:1–10, 2015. doi: 10.1016/j.rse.2014.08.037.

[43] Dirk Herman Hoekman. *Radar remote sensing data for applications in forestry*. Wageningen University and Research, 1990.

[44] Masahiro Hori. Near-daily monitoring of surface temperature and channel width of the six largest arctic rivers from space using gcom-c/sgli. *Remote Sensing of Environment*, 263:112538, 2021. doi: https://doi.org/10.1016/j.rse.2021.112538.

[45] R. Hummel and R. Moniot. Reconstructions from zero crossings in scale space. *IEEE Transactions on Acoustics, Speech, and Signal Processing*, 37:2111–2130, 1989. doi: 10.1109/29.45555.

[46] Pasquale Imperatore and Gerardo Di Martino. Sar radiometric calibration based on differential geometry: From theory to experimentation on saocom imagery. *Remote Sensing*, 15(5), 2023. doi: 10.3390/rs15051286.

[47] Sathit Intajag and Sakreya Chitwong. Speckle noise estimation with generalized gamma distribution. In *2006 SICE-ICASE International Joint Conference*, pages 1164–1167, 2006. doi: 10.1109/SICE.2006.315296.

[48] Furkan Isikdogan, Alan Bovik, and Paola Passalacqua. Rivamap: An automated river analysis and mapping engine. *Remote Sensing of Environment*, 202:88–97, 2017. doi: https://doi.org/10.1016/j.rse.2017.03.044.

[49] Eric Pottier Jong-Sen Lee, editor. *Polarimetric Radar Imaging*. CRC Press, 2009. doi: https://doi.org/10.1201/9781420054989.

[50] Narges Kheradmandi and Vida Mehranfar. A critical review and comparative study on image segmentation-based techniques for pavement crack detection. *Construction and Building Materials*, 321:126162, 2022. doi: https://doi.org/10.1016/j.conbuildmat.2021.126162.

[51] Sascha Klemenjak, Björn Waske, Silvia Valero, and Jocelyn Chanussot. Automatic detection of rivers in high-resolution sar data. *IEEE Journal of Selected Topics in Applied Earth Observations and Remote Sensing*, 5:1364–1372, 2012. doi: 10.1109/JSTARS.2012.2189099.

[52] J.J. Koenderink. The structure of images. *Biological Cybernetics*, 50:363–370, 1984. doi: https://doi.org/10.1007/BF00336961.

[53] Theodore Langhorst and Tamlin Pavelsky. Global observations of riverbank erosion and accretion from landsat imagery. *Journal of Geophysical Research: Earth Surface*, 128(2):e2022JF006774, 2023. doi: https://doi.org/10.1029/2022JF006774. URL `https://agupubs.onlinelibrary.wiley.com/doi/abs/10.1029/2022JF006774`.

[54] Jong-Sen Lee. Digital image enhancement and noise filtering by use of local statistics. *IEEE Transactions on Pattern Analysis and Machine Intelligence*, PAMI-2:165–168, 1980. doi: 10.1109/TPAMI.1980.4766994.

[55] Jong-Sen Lee. Refined filtering of image noise using local statistics. *Computer Graphics and Image Processing*, 15:380–389, 1981. doi: https://doi.org/10.1016/S0146-664X(81)80018-4.

[56] Jong-Sen Lee. Digital image smoothing and the sigma filter. *Comput. Vis. Graph. Image Process.*, 24:255–269, 1983.

[57] Jong-Sen Lee, D.L. Schuler, and T.L. Ainsworth. Polarimetric sar data compensation for terrain azimuth slope variation. *IEEE Transactions on Geoscience and Remote Sensing*, 38(5):2153–2163, 2000. doi: 10.1109/36.868874.

[58] Jong-Sen Lee, Jen-Hung Wen, Thomas L. Ainsworth, Kun Shan Chen, and Abel J. Chen. Improved sigma filter for speckle filtering of sar imagery. *IEEE Transactions on Geoscience and Remote Sensing*, 47:202–213, 2009. doi: 10.1109/TGRS.2008.2002881.

[59] A. Lopes, E. Nezry, R. Touzi, and H. Laur. Maximum a posteriori speckle filtering and first order texture models in sar images. In *10th Annual International Symposium on Geoscience and Remote Sensing*, pages 2409–2412. IEEE, 1990. doi: 10.1109/IGARSS.1990.689026.

[60] A.J. Luckman. Correction of sar imagery for variation in pixel scattering area caused by topography. *IEEE Transactions on Geoscience and Remote Sensing*, 36(1):344–350, 1998. doi: 10.1109/36.655350.

[61] Francesco Mitidieri, Maria Nicolina Papa, Donato Amitrano, and Giuseppe Ruello. River morphology monitoring using multitemporal sar data: preliminary results. *European Journal of Remote Sensing*, 49:889–898, 2016. doi: 10.5721/EuJRS20164946.

[62] Meysam Moharrami, Mohammad Hassan Javanbakht, and Sara Attarchi. Automatic flood detection using sentinel-1 images on the google earth engine. *Environmental Monitoring and Assessment*, 193, 2021. doi: 10.1007/s10661-021-09037-7.

[63] Federico Monegaglia, Guido Zolezzi, Inci Güneralp, Alexander J. Henshaw, and Marco Tubino. Automated extraction of meandering river morphodynamics from multitemporal remotely sensed data. *Environmental Modelling and Software*, 105:171–186, 2018. doi: https://doi.org/10.1016/j.envsoft.2018.03.028.

[64] Deborah Nykanen, Efi Foufoula-Georgiou, and Victor Sapozhnikov. Study of spatial scaling in braided river patterns using synthetic aperture radar imagery. *Water Resources Research*, 34:1795–1808, 1998. doi: 10.1029/98WR00940.

[65] Christopher B. Obida, George A. Blackburn, James D. Whyatt, and Kirk T. Semple. River network delineation from sentinel-1 sar data. *International Journal of Applied Earth Observation and Geoinformation*, 83, 2019. doi: https://doi.org/10.1016/j.jag.2019.101910.

[66] Nobuyuki Otsu. A threshold selection method from gray level histograms. *IEEE Transactions on Systems, Man, and Cybernetics*, 9:62–66, 1979. doi: 10.1109/TSMC.1979.4310076.

[67] M. Pai, Vaibhav Mehrotra, Ujjwal Verma, and Radhika Pai. Improved semantic segmentation of water bodies and land in sar images using generative adversarial networks. *International Journal of Semantic Computing*, 14: 55–69, 2020. doi: 10.1142/S1793351X20400036.

[68] Manohara M.M. Pai, Vaibhav Mehrotra, Shreyas Aiyar, Ujjwal Verma, and Radhika M. Pai. Automatic segmentation of river and land in sar images: A deep learning approach. In *2019 IEEE Second International Conference on Artificial Intelligence and Knowledge Engineering (AIKE)*, pages 15–20, 2019. doi: 10.1109/AIKE.2019.00011.

[69] Maria Nicolina Papa, Giuseppe Ruello, Francesco Mitidieri, and Donato Amitrano. Advanced technologies for satellite monitoring of water resources. In Vincenzo Naddeo, Malini Balakrishnan, and Kwang-Ho Choo, editors, *Frontiers in Water-Energy-Nexus—Nature-Based Solutions, Advanced Technologies and Best Practices for Environmental Sustainability*, pages 157–160, Cham, 2020. Springer International Publishing. doi: 10.1007/978-3-030-13068-8_38.

[70] Tamlin M. Pavelsky and Laurence C. Smith. Rivwidth: A software tool for the calculation of river widths from remotely sensed imagery. *IEEE Geoscience and Remote Sensing Letters*, 5:70–73, 2008. doi: 10.1109/LGRS.2007.908305.

[71] J.-F Pekel, Andrew Cottam, Noel Gorelick, and Alan Belward. High-resolution mapping of global surface water and its long-term changes. *Nature*, 540:–, 12 2016. doi: 10.1038/nature20584.

[72] P. Perona and J. Malik. Scale-space and edge detection using anisotropic diffusion. *IEEE Transactions on Pattern Analysis and Machine Intelligence*, 12: 629–639, 1990. doi: 10.1109/34.56205.

[73] Danielle Katharine Petsch, Vivian de Mello Cionek, Sidinei Magela Thomaz, and Natalia Carneiro Lacerda dos Santos. Ecosystem services provided by river-floodplain ecosystems. *Hydrobiologia*, 2022. doi: https://doi.org/10.1007/s10750-022-04916-7. URL `https://doi.org/10.1007/s10750-022-04916-7`.

[74] J. D. Phillips. Evolutionary geomorphology: thresholds and nonlinearity in landform response to environmental change. *Hydrology and Earth System Sciences*, 10(5):731–742, 2006. doi: 10.5194/hess-10-731-2006. URL `https://hess.copernicus.org/articles/10/731/2006/`.

[75] Nazzareno Pierdicca, Marco Chini, and Luca Pulvirenti. Enhanced land cover and flood mapping at c- and l-band. In *IGARSS 2020 - 2020 IEEE International Geoscience and Remote Sensing Symposium*, pages 4061–4064, 2020. doi: 10.1109/IGARSS39084.2020.9324233.

[76] Hervé Piégay, Fanny Arnaud, Barbara Belletti, Mélanie Bertrand, Simone Bizzi, Patrice Carbonneau, Simon Dufour, Frédéric Liébault, Virginia Ruiz-Villanueva, and Louise Slater. Remotely sensed rivers in the anthropocene: state of the art and prospects. *Earth Surface Processes and Landforms*, 45 (1):157–188, 2020. doi: https://doi.org/10.1002/esp.4787. URL `https://onlinelibrary.wiley.com/doi/abs/10.1002/esp.4787`.

[77] Jordan Powers, Joseph Klemp, William Skamarock, Christopher Davis, Jimy Dudhia, David Gill, Janice Coen, David Gochis, Ravan Ahmadov, Steven Peckham, Georg Grell, John Michalakes, Samuel Trahan, Stanley Benjamin, Curtis Alexander, Geoffrey Dimego, Wei Wang, Craig Schwartz, Glen Romine, and Michael Duda. The weather research and forecasting (wrf) model: Overview, system efforts, and future directions. *Bulletin of the American Meteorological Society*, 98:–, 2017. doi: 10.1175/BAMS-D-15-00308.1.

[78] L. Pulvirenti, M. Chini, N. Pierdicca, L. Guerriero, and P. Ferrazzoli. Flood monitoring using multi-temporal cosmo-skymed data: Image segmentation and signature interpretation. *Remote Sensing of Environment*, 115:990–1002, 2011. doi: 10.1016/j.rse.2010.12.002.

[79] Luca Pulvirenti, Nazzareno Pierdicca, Marco Chini, and Leila Guerriero. Monitoring flood evolution in vegetated areas using cosmo-skymed data: The tuscany 2009 case study. *IEEE Journal of Selected Topics in Applied Earth Observations and Remote Sensing*, 6(4):1807–1816, 2013. doi: 10.1109/JSTARS.2012.2219509.

[80] Luca Pulvirenti, Frank Silvio Marzano, Nazzareno Pierdicca, Saverio Mori, and Marco Chini. Discrimination of water surfaces, heavy rainfall, and wet snow using cosmo-skymed observations of severe weather events. *IEEE Transactions on Geoscience and Remote Sensing*, 52(2):858–869, 2014. doi: 10.1109/TGRS.2013.2244606.

[81] Markus Reichstein, Gustau Camps-Valls, Bjorn Stevens, Martin Jung, Joachim Denzler, Nuno Carvalhais, and Prabhat. Deep learning and process understanding for data-driven earth system science. *Nature*, 566: 195–204, 2019. doi: https://doi.org/10.1038/s41586-019-0912-1. URL `https://www.nature.com/articles/s41586-019-0912-1`.

[82] Massimo Rinaldi and Stephen E. Darby. 9 modelling river-bank-erosion processes and mass failure mechanisms: progress towards fully coupled simulations. In *Gravel-Bed Rivers VI: From Process Understanding to River Restoration*, volume 11 of *Developments in Earth Surface Processes*, pages 213–239. Elsevier, 2007. doi: https://doi.org/10.1016/S0928-2025(07)11126-3.

[83] Shiblu Sarker, Tanni Sarker, Olkeba Tolessa Leta, Sarder Udoy Raihan, Imran Khan, and Nur Ahmed. Understanding the planform complexity and morphodynamic properties of brahmaputra river in bangladesh: Protection and exploitation of riparian areas. *Water*, 15, 2023. doi: 10.3390/w15071384.

[84] Prabhishek Singh, Manoj Diwakar, Achyut Shankar, Raj Shree Pandey, and Manoj Kumar. A review on sar image and its despeckling. *Archives of Computational Methods in Engineering*, 28:4634–4653, 2021. doi: 10.1007/s11831-021-09548-z.

[85] Laurence Smith, Bryan Isacks, Richard Forster, A. Bloom, and Ilana Preuss. Estimation of discharge from braided glacial rivers using ers 1 synthetic aperture radar: First results. *Water Resources Research*, 31:1325–1329, 1995. doi: 10.1029/95WR00145.

[86] LC Smith. Satellite remote sensing of river inundation area, stage, and discharge: A review. *Hydrological Processes*, 11:1427–1439, 1997. doi: 10.1002/(SICI)1099-1085(199708)11:10<1427::AID-HYP473>3.0.CO;2-S.

[87] D. Spada, P. Molinari, W. Bertoldi, A. Vitti, and G. Zolezzi. Multi-temporal image analysis for fluvial morphological characterization with application to albanian rivers. *ISPRS International Journal of Geo-Information*, 7, 2018. doi: 10.3390/ijgi7080314.

[88] P. Swain and R. King. Two effective feature selection criteria for multispectral remote sensing. *LARS TechnicalReports*, 1973.

[89] Ratnakar Swain and Bhabagrahi Sahoo. Improving river water quality monitoring using satellite data products and a genetic algorithm processing approach. *Sustainability of Water Quality and Ecology*, 9-10:88–114, 2017. doi: https://doi.org/10.1016/j.swaqe.2017.09.001.

[90] Jianbo Tan, Yi Tang, Bin Liu, Guang Zhao, Yu Mu, Mingjiang Sun, and Bo Wang. A self-adaptive thresholding approach for automatic water extraction using sentinel-1 sar imagery based on otsu algorithm and distance block. *Remote Sensing*, 15, 2023. doi: 10.3390/rs15102690.

[91] Muhammad Atiq Ur Rehman Tariq, Rashid Farooq, and Nick van de Giesen. A critical review of flood risk management and the selection of suitable measures. *Applied Sciences*, 10, 2020. doi: 10.3390/app10238752.

[92] Simone Tarquini, Ilaria Isola, Massimiliano Favalli, Francesco Mazzarini, Marina Bisson, M. Pareschi, and Enzo Boschi. Tinitaly/01: a new triangular irregular network of italy. *Annals of Geophysics*, 50, 2007. doi: 10.4401/ag-4424.

[93] Klement Tockner and Jack A. Stanford. Riverine flood plains: present state and future trends. *Environmental Conservation*, 29(3):308–330, 2002. doi: 10.1017/S037689290200022X.

[94] Klement Tockner, James V Ward, David B Arscott, Peter J Edwards, Johannes Kollmann, Angela M Gurnell, Geoffrey E Petts, and Bruno Maiolini. The tagliamento river: a model ecosystem of european importance. *Aquatic Sciences*, 65:239–253, 2003. doi: 10.1007/s00027-003-0699-9.

[95] André Twele, Wenxi Cao, Simon Plank, and Sandro Martinis. Sentinel-1-based flood mapping: a fully automated processing chain. *International Journal of Remote Sensing*, 37:2990–3004, 2016. doi: 10.1080/01431161.2016.1192304.

[96] L. M. H. Ulander. Radiometric slope correction of synthetic-aperture radar images. *IEEE Transactions on Geoscience and Remote Sensing*, 34:1115–1122, 1996. doi: 10.1109/36.536527.

[97] D. van der Nat, A. P. Schmidt, K. Tockner, P. J. Edwards, and J. V. Ward. Inundation dynamics in braided floodplains: Tagliamento river, northeast italy. *Ecosystems*, 5(7):636–647, 2002. doi: 10.1007/s10021-002-0170-0.

[98] J.J. van Zyl, B.D. Chapman, P. Dubois, and J. Shi. The effect of topography on sar calibration. *IEEE Transactions on Geoscience and Remote Sensing*, 31(5): 1036–1043, 1993. doi: 10.1109/36.263774.

[99] Ujjwal Verma, Arjun Chauhan, Manohara Pai M.M., and Radhika Pai. Deep-rivwidth : Deep learning based semantic segmentation approach for river identification and width measurement in sar images of coastal karnataka. *Computers & Geosciences*, 154:104805, 2021. doi: https://doi.org/10.1016/j.cageo.2021.104805.

[100] Andreas Vollrath, Adugna Mullissa, and Johannes Reiche. Angular-based radiometric slope correction for sentinel-1 on google earth engine. *Remote Sensing*, 12, 2020. doi: 10.3390/rs12111867.

[101] Matilde Welber, Walter Bertoldi, and Marco Tubino. The response of braided planform configuration to flow variations, bed reworking and vegetation: The case of the tagliamento river, italy. *Earth Surface Processes and Landforms*, 37:572–582, 2012. doi: 10.1002/esp.3196.

[102] Xuan Wu, Zhijie Zhang, Shengqing Xiong, Wanchang Zhang, Jiakui Tang, Zhenghao Li, Bangsheng An, and Rui Li. A near-real-time flood detection method based on deep learning and sar images. *Remote Sensing*, 15(8), 2023. ISSN 2072-4292. doi: 10.3390/rs15082046. URL `https://www.mdpi.com/2072-4292/15/8/2046`.

[103] Da Yuan, Chao Wang, Lin Wu, Xu Yang, Zhengwei Guo, Xiaoyan Dang, Jianhui Zhao, and Ning Li. Water stream extraction via feature-fused encoder-decoder network based on sar images. *Remote Sensing*, 15, 2023. doi: 10.3390/rs15061559.

[104] Jinsong Zhang, Mengdao Xing, Guang-Cai Sun, Jianlai Chen, Mengya Li, Yihua Hu, and Zheng Bao. Water body detection in high-resolution sar images with cascaded fully-convolutional network and variable focal loss. *IEEE Transactions on Geoscience and Remote Sensing*, 59:316–332, 2021. doi: 10.1109/TGRS.2020.2999405.

[105] Sulong Zhou, Pengyu Kan, Janet Silbernagel, and Jiefeng Jin. Application of image segmentation in surface water extraction of freshwater lakes using radar data. *ISPRS International Journal of Geo-Information*, 9, 2020. doi: 10.3390/ijgi9070424.

Chapter 2

Detection of wet channel with COSMO–SkyMed SAR data and morphometric indices analysis

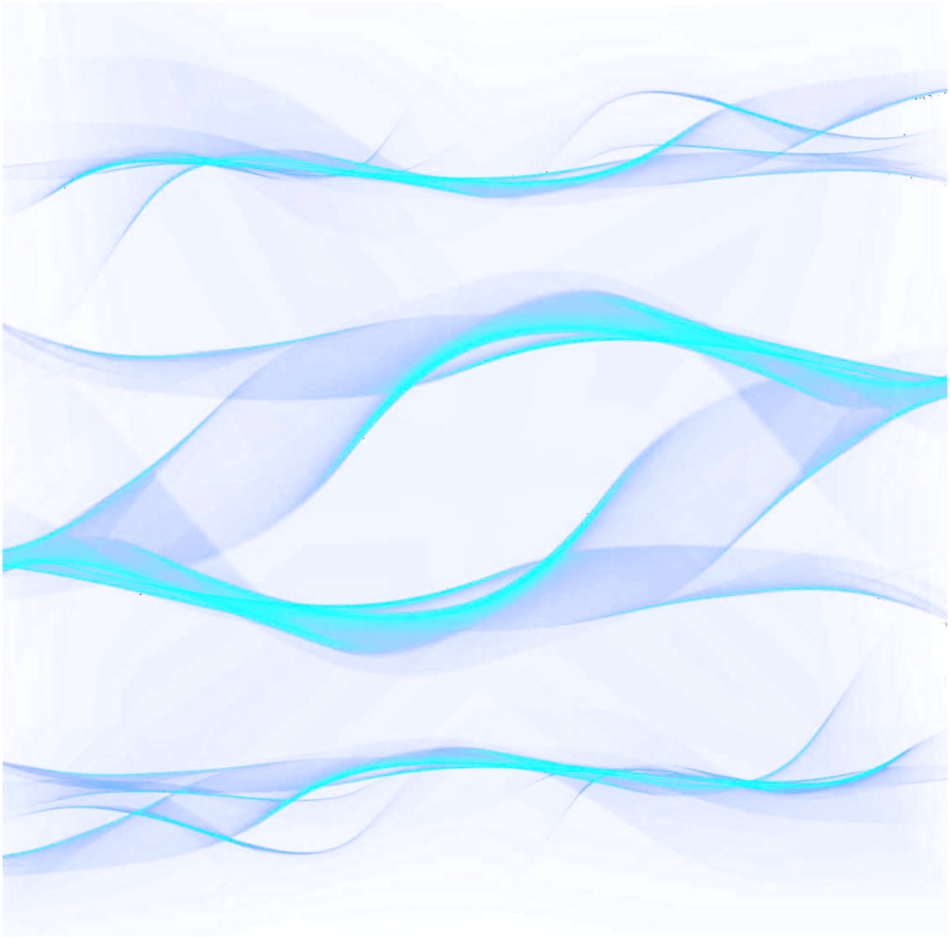

Abstract

Braided rivers demonstrate a unique profile marked by numerous unstable channels, transient bars, and very active channel processes, stemming from intensive bed-load transport. Notably, significant morphological adjustments occur not only as response of bankfull flood but even with moderate flow pulses. The empirical investigation of the dynamics of a multi-thread river, can be performed using various metrics. Bar growth, channel length, braiding index (defined as the number of branches in a cross-section), and other indicators, are employed to investigate the response of the braiding system to diverse stressors, such as floods, sediment abstraction, agricultural and hydropower water usage, as well as restoration operations. However, only few investigations have been performed to identify the relationship between the indices and the unsteady discharges that occur during extreme events in natural braided rivers. In this chapter, we utilize the unsupervised methodology based on the Google Earth Engine cloud infrastructure with the Self-Adaptive Thresholding Approach (SATA) algorithm, previously introduced (Chapter 1), to (i) obtain from the COSMO-SkyMed images the temporal evolution of the braiding system, and to assess and evaluate (ii) the temporal evolution of the Total Braiding Intensity (TBI) index defined as the number of active channels, (iii) the oscillation length of the Maximum Channel Distance (MCD) defined as the distance between the most external channels, and (iv) the oscillation length of the Cross-Sectional Cumulative Wetted Area (WA) defined as the sum of the wet area of all chanels in a cross section. In this study, the spatially explicit water masks obtained from Sentinel-1 and COSMO-SkyMed SAR data, acquired simultaneously, are also compared. The analysys confirmed that high-resolution SAR data represent an excellent dataset for the detection of braided river systems, allowing the detection of small secondary channels. Indeed, this allowed to highlight that the TBI index shifts after the flood towards higher values and that dimensionless wavelengths λ of both the Maximum Channel Distancce (MCD) and of the Cross-Sectional Cumulative Wetted Area (WA) depends from the hydrometric level (h).

2.1 Introduction

Flow variations and floods represent two pivotal factors in the formation of braided fluvial patterns. The mutual interaction between unsteady water discharge and bed load sediment transport engenders the creation of multiple branches within the active channel. The complexity of braided riverbeds' conformation, as represented by appropriate morphometric indices, reveals direct relationships between the flow rate and the current transport capacity [2]. This study seeks to examine changes in braided river patterns by assessing the temporal evolution of morphometric indices in response to a flood event using high ground resolution SAR images. The images, processed by leveraging the previously developed processing chain for the Level 1 (L1) Ground Range Detected (GRD) product of Sentinel-1 SAR imagery (Chapter 1), yielded temporally distinct water masks of the braiding system. The morphometric indices thus obtained, appropriately analyzed using Wavelet Transform (WT) provided insights into fluvial spatial scales [33].

Past works have highlighted how flow variations play a primary role in fluvial ecology, conveying organic matter and causing slight plano-altimetric changes, whereas floods have the greatest impact on braided rivers and their plano-altimetric setup. This morphological pattern were analysed at an intermediate to extended temporal scale [11], typically failing to discriminate between the impacts associated with flow variations from those attributed to floods.

Some studies have more effectively addressed this challenge by placing a focused emphasis on the relationship between morphological changes and flood events, utilizing digital single-lens reflex (SLR) cameras to capture high-definition images of relatively short sections of rivers, approximately 1.0 km long. This allowed for a clearer understanding of the response of morphological features and the related indices to flow variations and floods [3, 31].

The monitoring of morphological evolution through remote sensing techniques primarily relies on spectral data to detect water surfaces. These methods include simple thresholding index approaches, such as the Normalized Difference Water Index (NDWI) [18, 28], or more complex approaches that integrate them with additional indices like the Land Surface Water Index (LSWI) and Vegetation Indexes (NDVI or EVI). The application of Index Change Detection (ICD) techniques [27], or the use of Expert Systems (ES), are also useful to categorize each pixel into one of three designated classes: water, land, or an invalid land class [24].

All these techniques highlight the capabilities of optical and multispectral data in providing essential information for comprehensive river monitoring. However, challenges such as cloud cover, the necessity for daylight conditions, and the opportunity to increase the length of the studied river section beyond what is possible with in situ monitoring systems, necessitate the complementary use of Synthetic Aperture Radar (SAR) technologies. Therefore, to address the significant limitations imposed by adverse atmospheric conditions, which are often prevalent during flood events, and with the aim of extending the monitored river reach to up to 13 km, this study proposes the utilization of high-resolution COSMO-SkyMed (CSM) synthetic aperture radar data.

The unsupervised, cloud-based methodology, developed on the cloud infrastructure of Google Earth Engine, was applied to the twelve COSMO-SkyMed acquisitions spanning from 7 October to 25 November 2018. The computational chain involves the following steps:

- Enriching the image stack with hydrometric data;
- Applying the radiometric slope correction algorithm;
- Reducing speckle noise;
- Extracting the wet channel with a Self-Adaptive Thresholding Approach (SATA);
- Output functions.

This process resulted in twelve distinct water masks of the braiding system. After delineating the braided system for each CSM acquisition within the studied reach, the temporal evolution of certain indices was evaluated. Morphological indices are quantitative measures that characterize and analyze the physical form or structure of natural rivers and water bodies. These indices are pivotal in assessing the geomorphic dynamics, hydrological processes, and environmental health of river systems, offering a comprehensive view of river morphological evolutions and their interactions with both natural and anthropogenic factors. Table 2.1 presents a concise and non-exhaustive list of indices regarding braided river systems, as proposed by various authors. The indices considered in this study include the Total Braiding Intensity index (TBI) [2], defined as the number of wetted channels per cross-section, for its best trade–off between rapidity of application & accuracy with respect to results [7]; the Cross-Sectional Cumulative Wetted Area (WA), defined as the sum of the wet area of all channels; and the Maximum Channel Distance (MCD), determined by the distance between the most external channels. The later, when the bankfull discharge condition is reached, represents the width of the whole area subjected to morphological processes.

The data collection unveiled an oscillatory behavior that is both spatially varying and non-stationary along the river reach, and was observed in key metrics such as the Maximum Channel Distance (MCD) and the Cross-Sectional Cumulative Wetted Area (WA). This complex behavior underscores the necessity of a detailed investigation due to the presence and significance of multiple wavelengths within the data. Fourier Transform (FT) analysis offers a distinct advantage in this context, as it adeptly represents the energy contained within each frequency component of a signal over a specified time or spatial interval. However, the resolution of FT analysis is inherently constrained by the width of the window function, limiting its ability to simultaneously capture both local and global information contained within the signal [15, 14].

Table 2.1: *Indexes related to braided river systems.*

Index	**Equation**	**Notes**	**Ref.**
Braiding Index (B_I)	$\frac{2\sum L_b}{L_r}$	L_b = lengths of islands and (or) bars in reach; L_r = length of reach.	[4]
Braiding Index (B_I)	$\frac{2\sum L_b}{L_r} + \frac{2\sum N_b}{L_r}$	N_b = number of bars.	[12]
Braiding Index (B_I)	$\frac{\sum N_l}{1.25L'}$	N_l = number of braids; L' = distance between successive confluence and bifurcation.	[26]
Braiding Index (B_I)	$\frac{L_{Ctot}}{L_{Cmax}}$	L_{Ctot} = sum of the lengths of all segments of the primary channel; L_{Cmax} = length of the widest channel.	[10]
Braiding Index (B_I)	$\frac{\sum L_i}{L_{Main}}$	$\sum L_i$ = total length of bankfull channels cut into the floodplain; L_{Main} = main channel length.	[22]
Total Braiding Index (TB_I)	$\sum WC_i$	sum of wetted channels per cross-section	[2]
Width ratio Index (W_r)	$\frac{\sum b}{B}$	b = width of an individual wet channel; B = total width of the active channel.	[17]
Sinuosity Index (S_I)	$\frac{\sum L_l}{L_r}$	L_l = length of an individual channel segment in the reach; L_r = length of reach.	[17]

The Continuous Wavelet Transform (CWT) analysis emerged as a solution designed to surpass the inherent limitations associated with Fourier Transform (FT) analysis, particularly in handling signals that exhibit both local and global characteristics. Initially, CWT found its primary application in the analysis of time-series data, especially those characterized by time-varying, non-stationary signals. Subsequently, its utility extended into geophysical studies, notably in seismic signal processing, demonstrating its versatility and effectiveness. More recently, CWT has been applied in the analysis of spatial series, particularly in examining the complex dynamics of meandering river planforms [33], underscoring its broad applicability across different scientific domains. Reviews on the use of wavelet analysis and future perspectives can be fond in decades Kumar & Foufoula-Georgiou 1997 [19], Mallat 2008 [21], Guido 2022 [14], Guo et al. 2022 [15] and Tary et al. 2014 [29].

2.2 Material and Methods

2.2.1 Study Area

As shown in Chapter 1, the Tagliamento River is a large gravel bed braided river located in the southern part of the Italian Alps. Despite some human alterations like water diversions and gravel mining, the Tagliamento River remains one of the few unmanaged river systems in Europe, offering a valuable opportunity to study natural morphological processes during flow and floods.

Its catchment area of approximately 2700 km^2 spans a transition from Alpine to Mediterranean climatic regimes, characterized by a pluvio-nival hydrological regime. The river, flowing approximately 178 km from its source near Mauria pass in the dolomitic Alps to the Adriatic Sea, exibits an extensive morphologically active zone of around 150 km^2 with a braided pattern and variable vegetated islands.

The Tagliamento River experiences a pluvio-nival hydrological regime, where snowmelt in the spring season (April–June) contributes to discharge, resulting in notable riverbed mobility during spring rain events. Major floods predominantly occur in the autumn (October–November), when humid air masses moving north from the sea generate spatially widespread heavy rains. The resulting floods have a very rapid water level increase that lasts for some days.

The river undergoes morphological alterations during both regular flow, characterized by minor plano-altimetric changes, and floods, which induce significant changes. Flow rate changes and floods predominantly occur in spring and autumn.

2.2.2 Data source for river delineation

In this work, the algorithm described in Chapter 1 [25] was employed to identify the braided channel network of the studied reach of the Tagliamento River using images acquired by the COnstellation of Small Satellites for Mediterranean Basin Observation COSMO-SkyMed (CSM). The CSM is an Italian Earth-imaging constellation, which comprises four identical Earth-imaging satellites, launched sequentially between 2007 and 2010. In this study, acquisitions in the Stripmap HIMAGE mode were employed, which have a ground resolution of 3 x 3 meters. The individual CSM satellite within the constellation has a near revisit time of approximately five days. When considering the full constellation (four satellites) the potential revisit time drop to a few hours on a global scale. The substantial swath width covered by each satellite in the Stripmap HIMAGE mode is 40 km. While Sentinel–1 operates as a C–band active sensor with a center frequency of 5.405 GHz, corresponding to a wavelength of approximately 5.5 cm, COSMO-SkyMed operates in the X-band with a center frequency of 9.6 GHz, corresponding to a shorter wavelength of 3.1 cm.

In this work, the available CSM images acquired during the 2018 event flood were used. Figure 2.1 demonstrates that, although the COSMO–SkyMed constellation provides higher resolution, it achieves a lower acquisition frequency than the Sentinel–1 constellation. The figure also presents the only acquisition by the Sentinel–2 satellite in the visible and near-infrared spectrum with cloud cover under 15%, underscoring the limitation of using this data for event-scale monitoring.

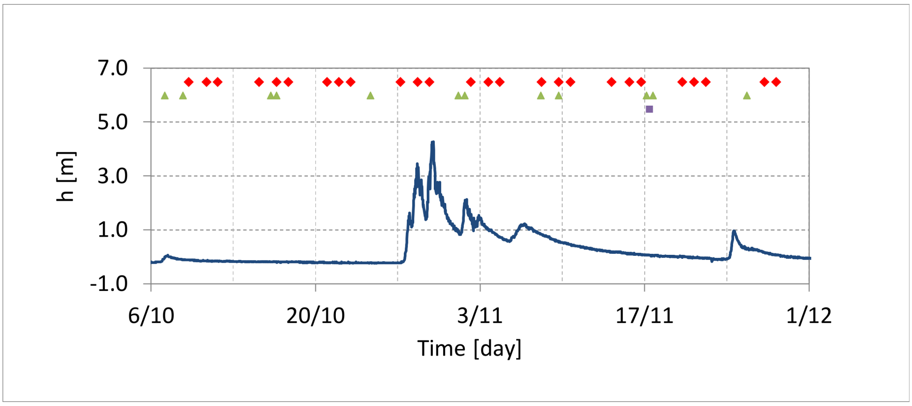

Figure 2.1: *Hydrometric water level recorded at the Venzone gauging station (blue solid line) with indication of COSMO–SkyMed acquisitions (green dots), Sentinel–1 acquisitions (red dots) and Sentinel–2 acquisitions with cloud cover less then 15% (purple dots).*

Before importing the CSM data into GEE, it was necessary to carry out the last three preprocessing steps (Table 2.2). For the Sentinel–1 satellite, the first three processes are essential, whereas they are not applicable to the CSM images. Orbit information, typically found in SAR product metadata, often lacks precision. Consequently, orbit auxiliary data, which detail Sentinel-1's exact position during acquisition, are released after a few days, enabling precise image positioning. Additionally, GRD border noise removal addresses specific artifacts arising from azimuth and range compression, which lead to radiometric distortions along the image's borders. Finally, thermal noise removal is employed to normalize the backscatter signal, aiming to reduce the additive thermal noise prevalent in the cross-polarization channel.

Standard SAR data processing typically omits radiometric corrections, resulting in substantial radiometric bias. Consequently, applying radiometric correction is essential to ensure that pixel values accurately reflect the surface's radar backscatter. Terrain correction and orthorectification adjust for distortions caused by topographical variations and the satellite's tilt. Additionally, the linear to dB operator transforms the bands into decibel (dB) units.

Table 2.2: *Preprocessing steps for Sentinel–1 and COSMO–SkyMed.*

Description	**Sentinel–1**	**COSMO–SkyMed**
Apply orbit file	X	–
GRD border noise removal	X	–
Thermal noise removal	X	–
Radiometric calibration	X	X
Terrain correction orthorectification	X	X
Linear to dB	X	X

2.2.3 Extraction of braiding parameters

The studied river reach was subdivided longitudinally into sections orthogonal to the river's centerline (c), spaced 50 meters apart, resulting in a series of braiding indexes data x'_n with $n = 0 \ldots N-1$. The total number of measurement points is 268. The total length of the reach is approximately 14 kilometers, exceeding ten times the wetted width required to ensure effective sampling. This sampling strategy provides a comprehensive representation of braiding intensity, as highlighted by Egozi and Ashmore (2009) [8].

The process of tracing the river cross–sections was automatically performed in a Geographic Information System (GIS). The Total Braiding Intensity index (TBI), the Cross-Sectional Cumulative Wetted Area (WA), and the Maximum Channel Distance (MCD), Figure 2.2, were derived through a semi–automatic procedure from the twelve water masks of the river's braiding system obtained applying the unsupervised and cloud based methodology detailed in Chapter 1.

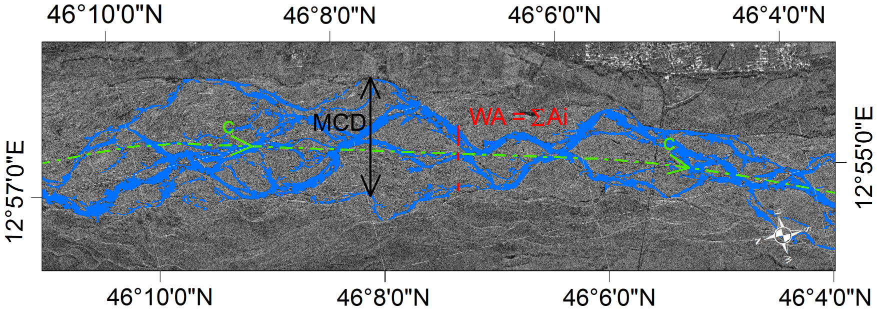

Figure 2.2: *Definition of the Maximum Channel Distance (MCD) as the distance between the most external channels and the Cross-Sectional Cumulative Wetted Area (WA) as the sum of the wet area of all channels.The geen dot dashed line is the curvilinear coordinate (c) of the center axis of the riverbed.*

Before the analysis with the CWT, the spatial series of measurements x'_n were normalized by their standard deviation. Therefore, any variables analyzed subsequently should be assumed to be normalized according to the equation 2.1.

$$x_n = \frac{(x'_n - \bar{x'_n})}{\sigma} \tag{2.1}$$

To facilitate the comparison of the Continuous Wavelet Transform (CWT) wavelength outcomes with other study cases, we introduce the concept of dimensionless wavelength, denoted as $\lambda = \Lambda / W$; here, Λ represents the wavelength derived from the CWT analysis for the variable of interest, and W is the average width of the river reach.

2.2.4 Continuous Wavelet Transform (CWT)

In the past decade, wavelet theory, as a versatile and rigorous mathematical tool, has seen numerous applications for non-stationary physical processes and was subject to continuous development, contributing to notable achievements in physics and related sciences. Analysing time or space series is possible to extract information about the dominant modes in the corresponding time–frequency or space–frequency domain. This decomposition enables the identification of dominant modes of variability and the observation of how these modes change over time or space.

Wavelet analysis has been successfully used in geophysics, with relevant results in meandering river geomorphology [33], in hydrological analysis [1, 20], stream flow forecasting and alteration analysis [16, 34]. In this study, we employed the Continuous Wavelet Transform (CWT) to analyze the oscillatory characteristics inherent in the spatial series of the Maximum Channel Distance (MCD) defined as the distance between the most external channels, and the Cross-Sectional Cumulative Wetted Area (WA) defined as the sum of the wet area of all channels (Figure 2.2). The Maximum Channel Distance (MCD) and the cross-sectional cumulative Wetted Area (WA) were assessed on cross sections equally spaced along the curvilinear coordinate (c) of the riverbed center axis, with a distance of 50 meters between each section.

Wavelet transform – theoretical basis

Given a series of measurements (x'_n with $n = 0...N-1$), equally spaced in the spatial or temporal domain (Δ_x), of any physical quantity, the function $\Psi_0(\eta)$ is considered an admissible wavelet function if it has a zero mean and is defined in the space–frequency (or time–frequency) domain [9]. In our case, measurements are carried out in the spatial domain defined by the curvilinear coordinate (c) of the riverbed center axis (Figure 2.2), with a frequency of Δ_c. Defined the wavelet scale s, the dimensionless space η of the wavelet function is defined as c/s. In this study, the Morlet mother wavelet [13], denoted as:

$$\Psi_0(\eta) = \pi^{-1/4} \cdot e^{i\omega_0\eta} \cdot e^{-\eta^2/2} \tag{2.2}$$

is employed. Here, ω_0 represents the non-dimensional frequency, and it was set to the default value for the Morlet mother wavelet of 6. In the limit of continuity, the Fourier transform of the equation 2.2 results in the wavelet function $\Psi_0(s\omega)$. This function is then normalized (Eq. 2.3) to have unit energy ($\int_{-\infty}^{+\infty} \hat{\Psi}(\omega')\, d\omega' = 1$) and thus facilitate the comparison of the Wavelet Transform (WT) with the transforms of other measurements.

$$\hat{\Psi}(s\omega_k) = \left(\frac{2\pi s}{\Delta_c}\right)^{1/2} \cdot \hat{\Psi}_0(s\omega_k) \tag{2.3}$$

The Continuous Wavelet Transform (CWT) of a discrete sequence of measures x_n involves convolving it with a scaled and translated wavelet function $\hat{\Psi}(s\omega_k)$. Torrence & Compo [30], defined the continuous wavelet transform of x_n as follows:

$$W_n(s) = \sum_{n'=0}^{N-1} X_{n'} \cdot \hat{\Psi}^* \left[\frac{(n'-n)\,\Delta_c}{s}\right] \tag{2.4}$$

In this notation, the $*$ denotes the complex conjugate operator, $(n'-n)\,\Delta_c$ is the term that translates the wavelet along the space domain, and s represents the wavelet scale. The smaller the scaling factor, the more "compressed" the wavelet is. The CWT provides a visual representation of how the amplitude, at different values of wavelet scale (s), varies in space.

Since the wavelet function is complex, its transform is also complex and can be subdivided into the real $\Re(W_n(s))$ and imaginary parts $\Im(W_n(s))$. The amplitude and the phase of the wavelet transform are:

$$\begin{aligned} A &= \sqrt{\Im^2 + \Re^2} \\ P &= \arctan\left(\Im / \Re\right) \end{aligned} \tag{2.5}$$

The Wavelet Power Spectrum is defined as the square of the amplitude of the wavelet transform namely $|W_n(s)|^2$.

In this study, the spatial series of MCD and WA exhibit sufficient smoothness to justify the use of a nonorthogonal wavelet function with a continuous wavelet transform.

An important aspect of the wavelet analysis is the choise of the set of scales s used in the continuous wavelet transform (Eq. 2.4). The set of scales is defined as:

$$s_j = s_0 \cdot 2^{j \cdot \Delta_j} \;\; with \;\; j \in [0, 1, ..., J] \tag{2.6}$$

where s_0 is the smalest scale in this work set to $2 \cdot \Delta_c$, Δ_j represents the number of sub–octaves per octave placed equal to 1/24, and J defines the largest scale through the following:

$$J = \frac{log_2\left(N \cdot \Delta_c / s_0\right)}{\Delta_j} \tag{2.7}$$

In the present case, the total number of spatial measurements for MCD and WA is $N = 286$, corresponding to $\Delta_c = 0.05$ km. This results in the smallest scale $s_0 = 0.1$ km, and a total of 93 scales ranging from 0.1 to 1.4 kilometers.

2.3 Results

2.3.1 Planimetrical evolution of braiding system

This section presents the results of the assessment of the planimetric evolution of the braiding system along the 14km reach of the Tagliamento River under study. Figures 2.5, 2.6, and 2.7 detail the inundation dynamics observed during the 2018 flood event. October and November of 2018 experienced significant rainfall, culminating in the exceptional Vaia storm flood event between October 27 and 30, 2018. The peak water level recorded at the Venzone gauging station exceeded 4.16 meters. These 12 panels facilitate visualization of the wet area's expansion and contraction in response to flow level variations, also highlighting the braiding system's alterations during the flood event.

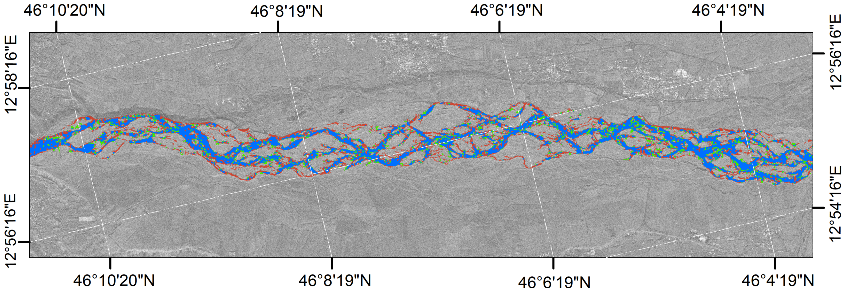

Figure 2.3: *Comparative analysis of S1 and CSM outputs for the 09/11/2018 acquisition. Blue pixels indicate areas classified as water by both S1 and CSM. Red pixels represent areas identified as water by CSM but not by S1, while green pixels denote areas classified as water by S1 but not by CSM.*

Figure 2.3 presents a comparison between the outputs obtained from S1 and CSM. The observed differences in the area classified as water are attributed to 'mixed pixels,' which contain elements of both water and dry soil. Sentinel–1, due to its ground resolution of 5 x 20 meters (resulting in 10 m pixel spacing), has a higher incidence of pixels that fall within regions mixing water and dry soil, leading to potential misclassification. The higher ground resolution of COSMO–SkyMed (3 x 3 meter) made it possible to identify secondary channels otherwise not visible in coarser resolution data like Sentinel–1. Indeed, the energy content of each pixel in a SAR image reflects the backscatter interactions from objects within that pixel. The increased spatial detail provided by the COSMO–SkyMed images allowed for a more accurate delineation of the braided channel network, capturing finer geomorphic features and improving the overall precision of the analysis. With CSM, the wetted channel area amounts to $4.0km^2$, while Sentinel–1 estimates it at $3.0km^2$, with a difference in the classification of about -25%. This discrepancy highlights the advantage of CSM data in providing a more detailed delineation of wet channels and the braiding system, thereby facilitating the assessment of key metrics such as the Total Braiding Intensity index (TBI), the Maximum Channel Distance (MCD), and the Cross-Sectional Cumulative Wetted Area (WA).

The TBI index was evaluated at reach scale from the 12 water masks of the river's braiding system. The right panels of Figures 2.5, 2.6, and 2.7 illustrate the probability density function (PDF), fitted using a normal kernel probability distribution, representing the frequency of the number of wetted channels per cross-section (TBI) in the studied reach of the Tagliamento River.

Before the flood's peak, when the water level presents low values, the most probable value of the Total Braiding Intensity (TBI) index was observed to range between 2.0 and 2.3. After the flood's peak, during its descending phase, a shift in the TBI index towards higher values can be noticed. The probability density function (PDF) indicates an increase of the most probable value of the

TBI index which falls between 3.0 and 3.7. The data acquired on 1 November 2018, corresponding to a hydrometric level of approximately 2.05 meters, suggest full inundation of the riverbed (bankfull conditions), resulting in a braiding index nearing unity.

The linear regression of the most likely TBI values, as shown in Figure 2.4, demonstrates a clear dependence of the Total Braiding Intensity (TBI) index on the dimensionless water level $\widehat{h} = (h_i - h_{min})/(h_{max} - h_{min})$. There's a direct linear correlation between the TBI index and increasing water levels. The boxplot, positioned at the top of Figure 2.4, provides a visual comparison of the TBI index before and after (Af) flooding, illustrating how morphological and hydrological conditions influence the index. Initially, the pre-flood TBI index values show a compact distribution with a lower median (2.2), indicating a narrower range of variation under low flow conditions. Following the flood (Af), there is a noticeable increase in the TBI index. This shift is evident in the higher median value (3.0) post-flood, indicating a wider variation in the TBI index influenced by the altered hydrological and morphological conditions.

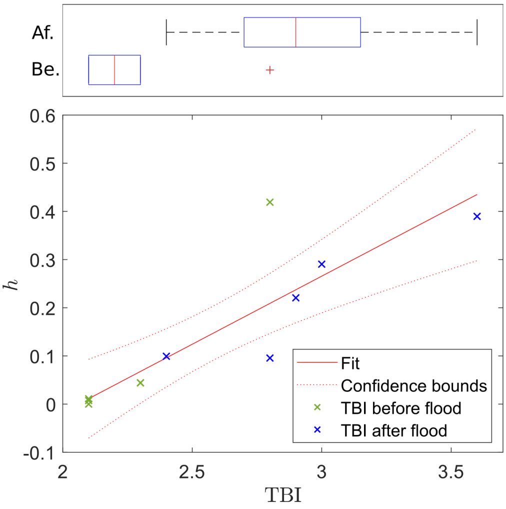

Figure 2.4: *Boxplot: comparison of the TBI index before (be) and after (Af) the flood, illustrating the significant increase in index values due to changes in river morphology and hydrological conditions. Bottom: Linear regression of the most probable TBI values, encompassing 95% confidence intervals.*

Similar results were observed by Bertoldi et al. [2] who analyzed the plano-altimetric evolutions of braided morphology during laboratory experiments. These experiments were conducted using a physical model under stationary flow conditions, thereby linking variations of the TBI index to the different braided morphologies that arise from specific formative flow conditions.

The present work, however, relates the variation of TBI index to the unsteady water levels of the 2018 flood, with discharges spanning from low to formative conditions. Thus, the TBI $-\ \widehat{h}$ relationship explains the differential response of the TBI index to varying discharge levels across two distinct braided river morphologies: pre-flood and post-flood conditions.

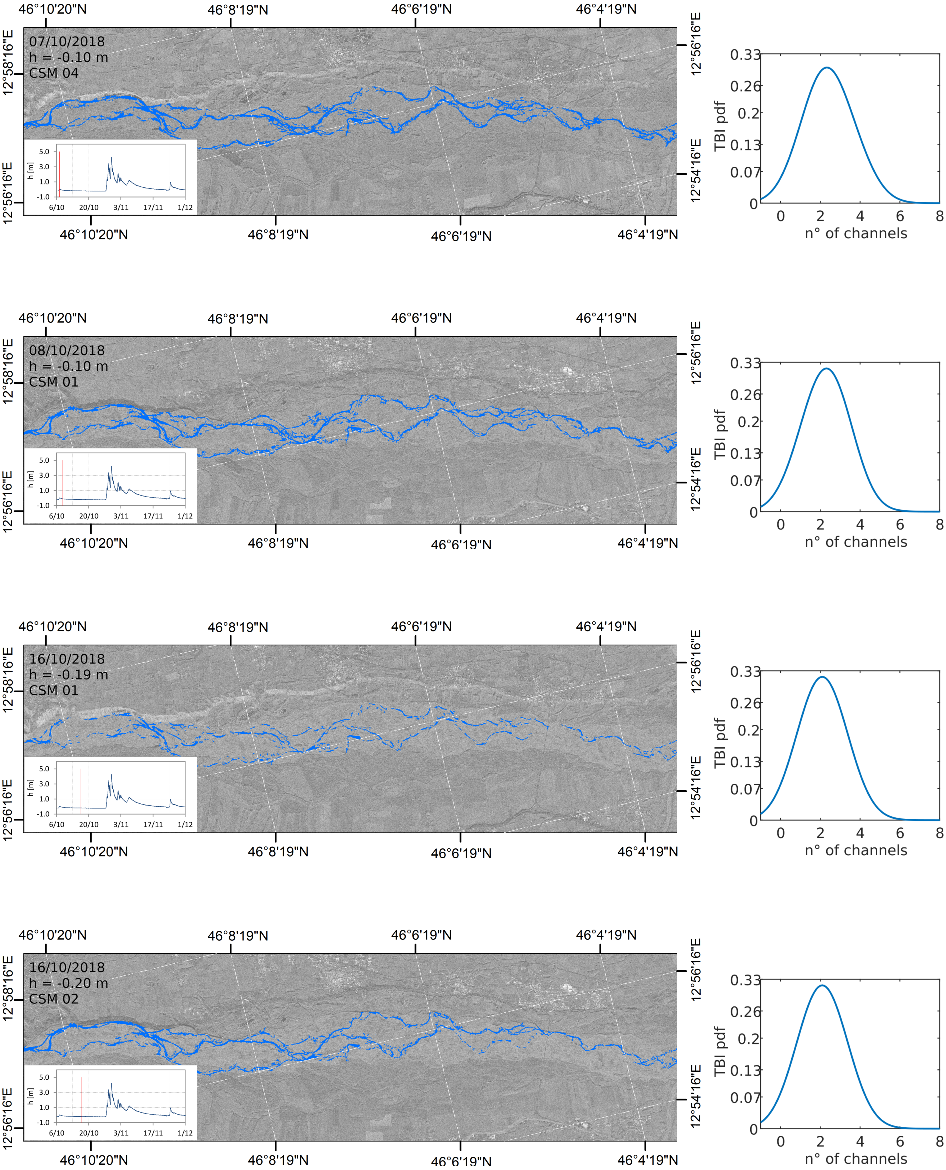

Figure 2.5: *Left: planimetrical evolution of braiding system from 07/10/2018 to 16/10/2018. Right: Probability density function (PDF) representing the frequency of the number of wetted channels per cross-section (TBI), fitted with a normal kernel probability distribution.*

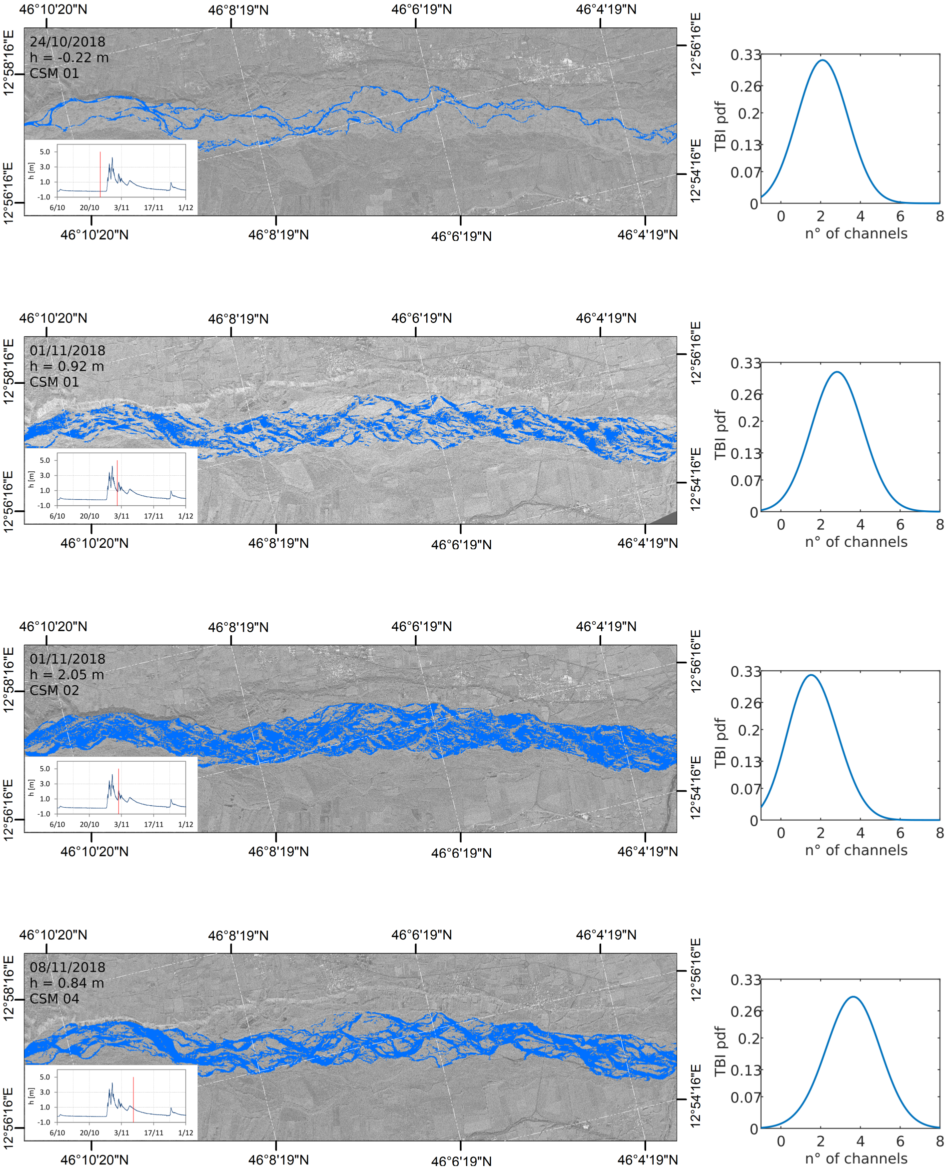

Figure 2.6: *Left: planimetrical evolution of braiding system from 24/10/2018 to 08/11/2018. Right: Probability density function (PDF) representing the frequency of the number of wetted channels per cross-section (TBI), fitted with a normal kernel probability distribution.*

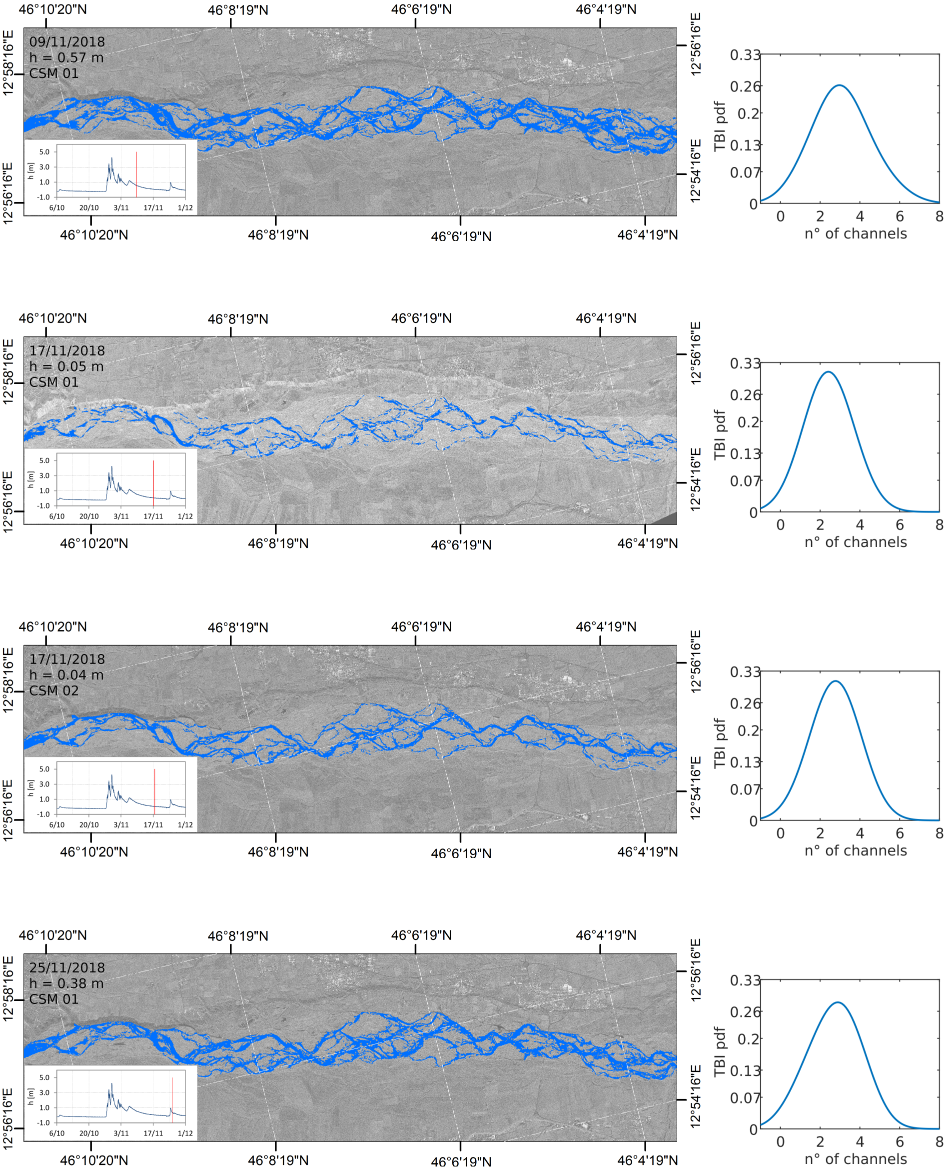

Figure 2.7: *Left: planimetrical evolution of braiding system from 09/11/2018 to 25/11/2018. Right: Probability density function (PDF) representing the frequency of the number of wetted channels per cross-section (TBI), fitted with a normal kernel probability distribution.*

2.3.2 Test cases of sinusoidal oscillations

This section presents the outcomes from the Continuous Wavelet Transform (CWT) analysis conducted on four synthetic sinusoidal oscillation test cases, applied to a hypothetical river with an active width of 800 meters. The results reported here provide a benchmark for subsequent analyses conducted on the real case (Section 2.3.3).

The first two cases exhibit a regular spatial planform oscillation, with the oscillation wavelength set to 0.2 km for the first test and 1.6 km for the second one, corresponding respectivelly to 1/4 and 2.0 times the channel whidth. The Wavelet Power Spectrum (WPS) depicted in mid–panel **b** of figures 2.8i and 2.8ii provides insights into the energy content inherent in the sinusoidal oscillations. As can be noticed, the bulk of the energy is concentrated within a relatively compact region around the dimensionless wavelengths $\lambda = 0.25$ and $\lambda = 2.0$, respectively. The white dashed line delineates the region, known as the Cone of Influence (COI), where edge effects become significant due to the finite length of the spatial measurement. In this region, the wavelet power spectrum is considered less reliable. In the mid-right panels **c**, the Space–averaged Wavelet Power, also known as as a Global Wavelet Spectrum (GWS), conveys the information on the mean energy content of the WPS for the different wavelength, giving a useful measure of the background spectrum. Comparing the Space–averaged Wavelet Power obtained from the first and the second case, it can be seen that the global power spectrum tends to amplify the power of longer wavelengths. This property had been highlighted in the past by Wu and Liu 2005 [32]. In the bottom panels **d**, the Scale-Averaged Wavelet Power illustrates the variations in power across a specific range of scales. The Scale-Averaged Wavelet Power graph thus enables us to discern whether there are variations in the oscillation amplitude of the morphometric index within the studied watercourse segment. In Figure 2.8iii, the hypothetical morphometric index exhibits spatial modulation of the amplitude along the watercourse. Conversely, in Figure 2.8iv, the hypothetical morphometric index demonstrates a decrease in power along the watercourse.

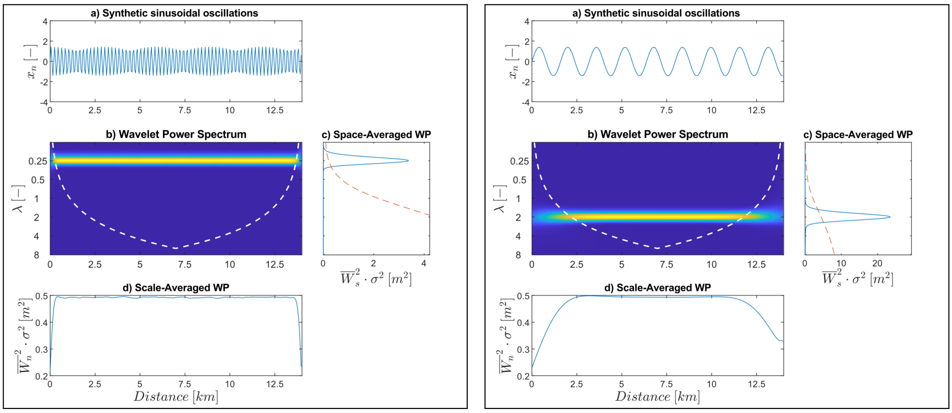

(i) *Wavelet analysis of the synthetic sinusoidal oscillations generated by a sine wave with a wavelength of 0.2 km, corresponding to 1/4 of the channel whidth set equal to 0.8 km.*

(ii) *Wavelet analysis of the synthetic sinusoidal oscillations generated by a sine wave with a wavelength of 1.6 km, corresponding to 2 times the channel whidth set equal to 0.8 km.*

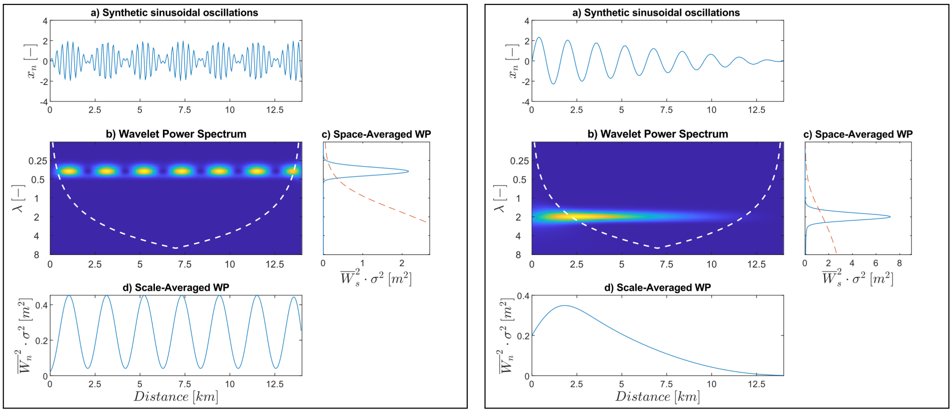

(iii) *Wavelet analysis of the synthetic sinusoidal oscillations depicted in the* ***i*** *panel with a spatial spatial modulation of the amplitude.*

(iv) *Wavelet analysis of the synthetic sinusoidal oscillations depicted in the* ***ii*** *panel with amplitude decreasing with the longitudinal distance.*

Figure 2.8: *The top panels* ***a)*** *display the synthetic sinusoidal planform oscillations; the middle panels* ***b)*** *plot the Wavelet Power Spectrum WPS (obtained using the Morlet wavelet) for the specific case; the mid-right panels* ***c)*** *illustrate the space-averaged wavelet power; the bottom panels* ***d)*** *showcase the scale-averaged Wavelet Power.*

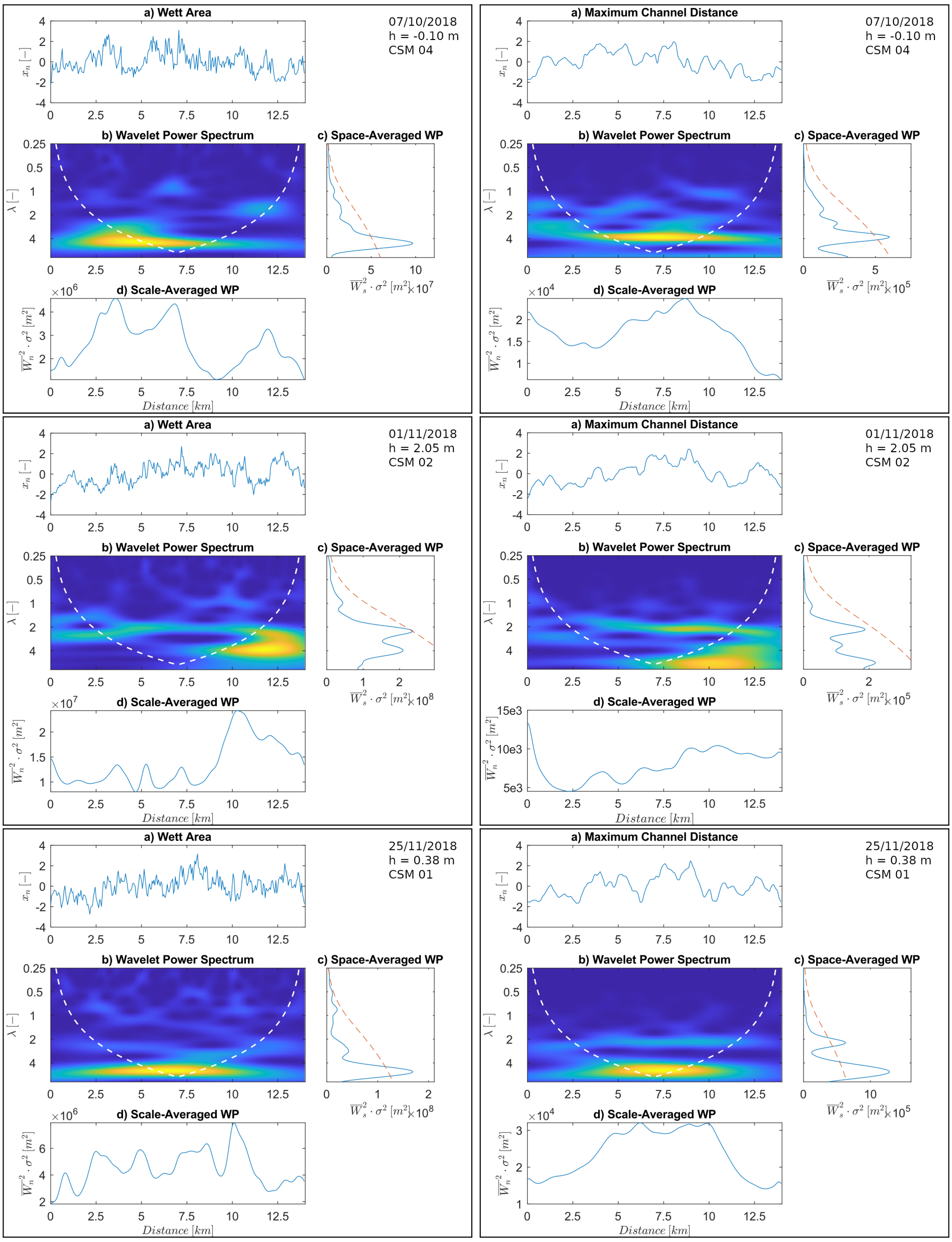

Figure 2.9: *This figure selectively presents the CWT outputs for three out of the twelve acquisitions, for the key stages: 07/10 prior to the flood peak, 01/11 during the flood event, and 25/11 following the flood event. The indices analyzed are the Cross-Sectional Cumulative Wetted Area (WA) in the left column and the Maximum Channel Distance (MCD) in the right column.*

2.3.3 CWT of Maximum Channel Distance (MCD) and Wet Area (WA)

Figure 2.9 displays the outcomes of the Continuous Wavelet Transform (CWT) analysis for two indices Cross-Sectional Cumulative Wetted Area (WA) and the Maximum Channel Distance (MCD), across three pivotal acquisitions: one representing the pre-flood state, another during the flood event, and the last at the event's conclusion.

Figure 2.10 provides a summary of the Continuous Wavelet Transform (CWT) analysis performed on the two indices, the Maximum Channel Distance (MCD) and the Cross-Sectional Cumulative Wetted Area (WA). These indices were derived from the braiding system, identified using the unsupervised and cloud-based methodology outlined in Section 1. This algorithm was applied on the twelve COSMO-SkyMed acquisitions, spanning from 7 October to 25 November 2018, and resulting in twelve distinct braiding system masks.

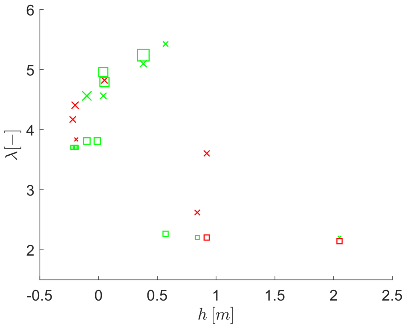

Figure 2.10: *Dimensionless wavelength number for the Maximum Channel Distance (MCD) index – square marker, and the Cross-Sectional Cumulative Wetted Area (WA) index – cross marker. Marker size and color denote distance from the significance limit line, with size reflecting the ratio defined in equation 2.8 and proportionality to distance from the confidence line. Red markers indicate a ratio* $R < 1$, *and green markers signify* $R > 1$.

Each pair of values $(\lambda_i; h_i)$, where i ranges from 1 to 12, corresponds to one of the twelve distinct braiding system masks. These pairs are derived by associating the value of λ_i at which the Global Wavelet Spectrum (GWS) reaches its maximum, with the value of h_i related to the i-th CSM image used.

The size and color of each marker are indicative of its distance from the significance limit line. The size of each marker represents the ratio of equation 2.8 and is proportional to the distance from the confidence line.

$$R = \frac{max\left(\bar{W}_s^2 \cdot \sigma^2\right)}{S_v} \tag{2.8}$$

where S_v is the value assumed by the significance line at the dimensionless wavelength value λ_i. Red markers signify that the ratio R is less than one, while green markers indicate a ratio greater than one. Square points correspond to the Maximum Channel Distance (MCD) index, and crosses pertain to the Cross-Sectional Cumulative Wetted Area (WA) index.

These findings underscore that the dimensionless wavelengths λ for both the Maximum Channel Distance (MCD) and the Cross-Sectional Cumulative Wetted Area (WA) are dependent on the hydrometric level (h). As the water level increases, the dimensionless wavelengths (λ) range from 3.5 to 5.5. Upon exceeding a water level of 0.6 meters, the dimensionless wavelengths approximately return to values around 2.2.

2.4 Discussion

The study presented herein highlights the potential of using high-resolution Synthetic Aperture Radar (SAR) data to detect the dynamics of braided river systems at a sub-event time scale. By applying the unsupervised Self-Adaptive Thresholding Approach (SATA), initially developed for Sentinel–1 data, to the COSMO-SkyMed SAR images in this study, we captured the temporal evolution of a 14 km long braided river reach of the Tagliamento with unprecedented planimetric details, overcoming problems highlighted in previous research [23], and operating at smaller scales than big floods detection [6], [5].

From the spatially fine detailed water channel braiding system, the temporal evolution of the Total Braiding Intensity (TBI) index, the Maximum Channel distance (MCD), and the Cross-Sectional Cumulative Wetted Area (WA) were evaluated with a spatial discretization of 50 meters along the river's centerline. These indices have revealed the pronounced sensitivity of braided rivers to variations in flow, and particularly in response to flood events.

Bertoldi et al. (2009) [2] demonstrated through laboratory flume experiments that the Total Braiding Intensity (TBI) increases with higher water discharge values under stationary, formative flow conditions. "Consequently, this study establishes a connection between the variations in the TBI index and the diverse braided morphologies resulting from specific formative flow conditions.

In this study, we have established a correlation between the TBI index and the varying water levels observed during the 2018 flood, with discharge values ranging from extremely low to formative contitions. This correlation, represented by the TBI – $\widehat{h}$ relationship, illustrates how the TBI index responds to unsteady discharge conditions for the distinct braided morphologies; the one present before the flood and the one created by the flood.

Despite variations attributable to disparate study conditions, both sets of findings concur in delineating a trend where the TBI index increases in response to increased discharge.

Analysis of the boxplot in Figure 2.4 reveals that the mean TBI index value increases post-flood, accompanied by a broader variance. This observation supports the hypothesis that prolonged periods without flooding lead to a sclerotic braided morphology characterized by fewer, more incised channels (indicative of a lower TBI). Conversely, the occurrence of a flood event triggers substantial sediment mobilization, fostering the development of a new morphology with a greater number of less incised channels than those observed prior to the flood.

The application of wavelet analysis to morphometric indices of braided rivers, notably the Maximum Channel Distance (MCD) and the Cross-Sectional Cumulative Wetted Area (WA), has revealed an interesting behavior of the dominant wavelength. Specifically, as water levels rise from low values to 0.6 meters, the spatial dimensionless wavelength (λ) increases from 3.5 to 5.5. At water levels exceeding 0.6 meters, the dimensionless wavelength drops within the range of 2.0 to 2.5. This wavelength represents the comprehensive oscillation within the river corridor, suggesting that morphological structures recur at intervals of 2.0 to 2.5 times the mean active width. This periodicity indicates a systematic repetition of morphological features along the river, underscoring the inherent spatial patterns in river morphology. From the river management perspective, this implies that in renaturalization projects, respecting the natural wavelength of oscillation may ensures a longer morphological stability for the chosen plano-altimetric design of the projected riverbed.

References

[1] B. Andreo, P. Jiménez, J.J. Durán, F. Carrasco, I. Vadillo, and A. Mangin. Climatic and hydrological variations during the last 117–166 years in the south of the iberian peninsula, from spectral and correlation analyses and continuous wavelet analyses. *Journal of Hydrology*, 324:24–39, 2006. doi: https://doi.org/10.1016/j.jhydrol.2005.09.010.

[2] Walter Bertoldi, Luca Zanoni, and Marco Tubino. Planform dynamics of braided streams. *Earth Surface Processes and Landforms*, 34(4):547–557, 2009. doi: https://doi.org/10.1002/esp.1755.

[3] Walter Bertoldi, Luca Zanoni, and Marco Tubino. Assessment of morphological changes induced by flow and flood pulses in a gravel bed braided river: The tagliamento river (italy). *Geomorphology*, 114:348–360, 2010. doi: https://doi.org/10.1016/j.geomorph.2009.07.017.

[4] James Coble Brice. *Channel patterns and terraces of the Loup Rivers in Nebraska*. US Government Printing Office, –, 1964.

[5] Han Cao, Hong Zhang, Chao Wang, and Bo Zhang. Operational flood detection using sentinel-1 sar data over large areas. *Water*, 11(4), 2019. doi: 10.3390/w11040786.

[6] Francisco Carreño Conde and María De Mata Muñoz. Flood monitoring based on the study of sentinel-1 sar images: The ebro river case study. *Water*, 11(12), 2019. doi: 10.3390/w11122454.

[7] Roey Egozi and Peter Ashmore. Defining and measuring braiding intensity. *Earth Surface Processes and Landforms*, 33(14):2121–2138, 2008. doi: https://doi.org/10.1002/esp.1658.

[8] Roey Egozi and Peter Ashmore. Experimental analysis of braided channel pattern response to increased discharge. *Journal of Geophysical Research: Earth Surface*, 114(F2):–, 2009. doi: https://doi.org/10.1029/2008JF001099.

[9] Marie Farge. Wavelet transforms and their applications to turbulence. *Annual Review of Fluid Mechanics*, 24:395–457, 1992. doi: 10.1146/annurev.fl.24.010192.002143.

[10] P. Friend and Rajiv Sinha. Braiding and meandering parameters. *Geological Society, London, Special Publications*, 75:105–111, 1993. doi: https://doi.org/10.1144/GSL.SP.1993.075.01.05.

[11] P. Gao, Z. Li, Y. You, Y. Zhou, and H. Piégay. Assessing functional characteristics of a braided river in the qinghai-tibet plateau, china. *Geomorphology*, 403:108180, 2022. doi: https://doi.org/10.1016/j.geomorph.2022.108180.

[12] Dru Germanoski and S. A. Schumm. Changes in braided river morphology resulting from aggradation and degradation. *The Journal of Geology*, 101(4): 451–466, 1993. doi: 10.1086/648239.

[13] P. Goupillaud, A. Grossmann, and J. Morlet. Cycle-octave and related transforms in seismic signal analysis. *Geoexploration*, 23(1):85–102, 1984. doi: https://doi.org/10.1016/0016-7142(84)90025-5.

[14] Rodrigo Capobianco Guido. Wavelets behind the scenes: Practical aspects, insights, and perspectives. *Physics Reports*, 985:1–23, 2022. doi: https://doi.org/10.1016/j.physrep.2022.08.001.

[15] Tiantian Guo, Tongpo Zhang, Enggee Lim, Miguel López-Benítez, Fei Ma, and Limin Yu. A review of wavelet analysis and its applications: Challenges and opportunities. *IEEE Access*, 10(–):58869–58903, 2022. doi: 10.1109/ACCESS.2022.3179517.

[16] S. Jasim Hadi and M. Tombul. Monthly streamflow forecasting using continuous wavelet and multi-gene genetic programming combination. *Journal of Hydrology*, 561:674–687, 2018. doi: https://doi.org/10.1016/j.jhydrol.2018.04.036.

[17] Le Ba Hong and T. R. H. Davies. A study of stream braiding. *GSA Bulletin*, 90:1839–1859, 1979. doi: 10.1130/GSAB-P2-90-1839.

[18] Faezeh Khalifeh Soltanian, Mozhgan Abbasi, and hamid reza riyahi bakhtyari. Flood monitoring using ndwi and mndwi spectral indices: a case study of aghqala flood-2019, golestan province, iran. *ISPRS - International Archives of the Photogrammetry, Remote Sensing and Spatial Information Sciences*, XLII-4/W18:605–607, 10 2019. doi: 10.5194/isprs-archives-XLII-4-W18-605-2019.

[19] Praveen Kumar and Efi Foufoula-Georgiou. Wavelet analysis for geophysical applications. *Reviews of Geophysics*, 35(4):385–412, 1997. doi: https://doi.org/10.1029/97RG00427.

[20] D. Labat, R. Ababou, and A. Mangin. Rainfall–runoff relations for karstic springs. part ii: continuous wavelet and discrete orthogonal multiresolution analyses. *Journal of Hydrology*, 238:149–178, 2000. doi: https://doi.org/10.1016/S0022-1694(00)00322-X.

[21] S. Mallat. *A Wavelet Tour of Signal Processing, The Sparse Way*. Acad. Press. , Burlington, Mass., –, 2008.

[22] M. Paul Mosley. Semi-determinate hydraulic geometry of river channels, south island, new zealand. *Earth Surface Processes and Landforms*, 6(2):127–137, 1981. doi: https://doi.org/10.1002/esp.3290060206.

[23] Maria Nicolina Papa, Giuseppe Ruello, Francesco Mitidieri, and Donato Amitrano. Advanced technologies for satellite monitoring of water resources. In Vincenzo Naddeo, Malini Balakrishnan, and Kwang-Ho Choo, editors, *Frontiers in Water-Energy-Nexus—Nature-Based Solutions, Advanced Technologies and Best Practices for Environmental Sustainability*, pages 157–160, Cham, 2020. Springer International Publishing. doi: 10.1007/978-3-030-13068-8_38.

[24] J.-F Pekel, Andrew Cottam, Noel Gorelick, and Alan Belward. High-resolution mapping of global surface water and its long-term changes. *Nature*, 540:–, 12 2016. doi: 10.1038/nature20584.

[25] D. Rossi, G. Zolezzi, W. Bertoldi, and A. Vitti. Monitoring braided river-bed dynamics at the sub-event time scale using time series of sentinel-1 sar imagery. *Remote Sensing*, 15:–, 2023. doi: 10.3390/rs15143622.

[26] Brian R Rust. A classification of alluvial channel systems. *Fluvial Sedimentology*, –:187–198, 1977. doi: --.

[27] Toshihiro Sakamoto, Nhan Van Nguyen, Akihiko Kotera, Hiroyuki Ohno, Naoki Ishitsuka, and Masayuki Yokozawa. Detecting temporal changes in the extent of annual flooding within the cambodia and the vietnamese mekong delta from modis time-series imagery. *Remote Sensing of Environment*, 109(3): 295–313, 2007. doi: https://doi.org/10.1016/j.rse.2007.01.011.

[28] Ramesh Sivanpillai, Kevin Jacobs, Chloe Mattilio, and Ela Piskorski. Rapid flood inundation mapping by differencing water indices from pre- and post-flood landsat images. *Frontiers of Earth Science*, 15:1–11, 03 2021. doi: 10.1007/s11707-020-0818-0.

[29] Jean Baptiste Tary, Roberto Henry Herrera, Jiajun Han, and Mirko van der Baan. Spectral estimation—what is new? what is next? *Reviews of Geophysics*, 52(4):723–749, 2014. doi: https://doi.org/10.1002/2014RG000461.

[30] Christopher Torrence and Gilbert P. Compo. A practical guide to wavelet analysis. *Bulletin of the American Meteorological Society*, 79(1):61 – 78, 1998. doi: https://doi.org/10.1175/1520-0477(1998)079<0061:APGTWA>2.0.CO;2.

[31] Matilde Welber, Walter Bertoldi, and Marco Tubino. The response of braided planform configuration to flow variations, bed reworking and vegetation: The case of the tagliamento river, italy. *Earth Surface Processes and Landforms*, 37:572–582, 2012. doi: 10.1002/esp.3196.

[32] Shu Wu and Qinyu Liu. Some problems on the global wavelet spectrum. *Journal of Ocean University of China*, 4:398–402, 10 2005. doi: 10.1007/s11802-005-0062-y.

[33] G. Zolezzi and I. Güneralp. Continuous wavelet characterization of the wavelengths and regularity of meandering rivers. *Geomorphology*, 252:98–111, 2016. doi: https://doi.org/10.1016/j.geomorph.2015.07.029.

[34] G. Zolezzi, A. Bellin, M. C. Bruno, B. Maiolini, and A. Siviglia. Assessing hydrological alterations at multiple temporal scales: Adige river, italy. *Water Resources Research*, 45:–, 2009. doi: https://doi.org/10.1029/2008WR007266.

Chapter 3

Assessing grain size of bed sediments for a comprehensive understanding of river dynamics

Abstract

Gravel–bed braided rivers are typically found in foothill regions worldwide, where the combination of high sediment supply, frequent flood events, and specific topography ensures significant morphological dynamics. One of the most important variable governing the riverine dynamics is the bed sediment size. Classical techniques for the grain size assessment necessitate extensive and time-consuming fieldwork, enabling the acquisition of grain size curves at specific points along the entire reach. Information obtained from specific points does not reflect the spatial pattern of the sediment, and thus, geostatistical techniques must be employed for spatialization. For these reasons, this study proposes the use of orthophotos produced through drone flights for the creation of riverbed roughness maps. This method enables a reduction in the time required to extract riverbed roughness data and facilitates the acquisition of spatially continuous roughness maps.

A grain size map of the Piave River bed was produced by (i) collecting 1x1 meter digital images of ground truths, from which the granulometric curve is derived using an image segmentation-based method; (ii) conducting a flight with an unmanned aerial vehicle (UAV) to acquire an orthophoto with a ground resolution of 2.5 cm; (iii) performing texture analysis utilizing both the co–occurrence matrix and the autocorrelation function methods on $1m^2$ orthophoto tiles extracted at the same location of digital images; (iv) conducting a regression analysis between the texture properties derived from orthophoto's tiles and the D_{50}, D_{84}, D_{90}, and D_{95} grain size characteristics obtained from the digital images; (v) deriving the map of the spatial pattern of grain size at the river reach scale.

The analysis demonstrates that the co–occurrence matrix, characterized by the statistical property of correlation, constitutes a statistically robust predictive model to predict grain size caracteristic. The validation process indicates that the model has overall accuracies for the three grain size characteristics D_{50}, D_{84}, and D_{90}, respectively, of 68.8%, 76.6%, and 76.6%. These results are promising, especially considering the complexities involved in predicting sediment grain size distribution. The high accuracy rates for D_{84} and D_{90} suggest that the model is particularly reliable in estimating larger grain sizes, which are critical for understanding sediment transport dynamics and riverbed stability. Moving forward, further refinement of the model could focus on improving D_{50} accuracy, potentially enhancing its applicability for comprehensive sediment management and engineering projects.

The method presented here, which provides the spatial pattern of grain size variation, offers considerable support for the implementation of detailed hydraulic models. Therefore, hydraulic models enriched with detailed grain size information can be integrated with ecological frameworks that require the same data, giving the opportunity to plann restoration projects.

3.1 Introduction

One of the most distinctive features of gravel–bed braided rivers is their multi–thread channel system. These rivers consist of numerous interweaving channels that separate and rejoin around bars or islands of gravel and sediment. The channels of gravel–bed braided rivers are highly dynamic. They frequently shift, erode, and deposit sediment, which changes their course over relatively short time periods. This dynamism is primarily driven by flow variations and sediment bed–load. The flow energy and the sediment layer characteristics (grain size and cohesiveness) determine the degree of channel sinuosity [1]. Traditionally, the assessment of grain size distribution of riverbed materials has been conducted by counting pebbles of various sizes along grids (Wolman, 1954 [11]), or over surface areas of 1 m^2 (Bunte, 2001 [4]). Employing these methods requires detailed and labor-intensive on-site investigations, which allow the collection of grain size distributions at designated locations throughout the river reach. However, data gathered from these isolated locations fail to capture the spatial distribution of sediments, necessitating the use of geostatistical methods to achieve spatial representation.

For this reason in the last decade, digital sieving from digital images and orthophotos has attracted increasing interest from the scientific community. The approaches for grain classification predominantly fall into two categories: texture-based image analysis and segmentation-based image processing. Techniques utilizing texture analysis are primarily aimed at estimating grain size from orthophotos captured via drone flights, whereas image segmentation techniques are mainly used for deriving the granulometric curve from digital photos acquired during field surveys.

One of the first milestone works using texture image analysis, and specifically the semivariogram approach, was that of Butler et al. (2001) [18], on which the subsequent works of Carbonneau et al. (2003) [24] and (2004) [6] were grafted. Alternative methodologies leverage the versatility of wavelet analysis to derive the grain size curve of sediment samples [5]. More recently, with the emergence of Unmanned Aerial Vehicles (UAVs) and the introduction of Structure from Motion techniques (SfM), analyses based on image textures have been integrated with 3D topographic data and the SfM point cloud [31] [30].

Methods designed for mapping and segmenting all grain features in images hold an advantage over texture-based approaches, as they do not require calibration specific to the site. The first successful attempts in using a treshold or multiple threshold steps applied to the grayscale images, date back to 2004 - 2005 with the works of Weichert et al. [29], and Graham et al. [12], [13]. Detert et al. (2012) [10] introduced enhancements to the watershed approach, targeting a reduction in grain over-segmentation and thereby mitigating the underestimation of the grain size curve. Purinton et al. (2019) [25] proposed an alternative methodology to the traditional watershed segmentation approach, which relies on intensity discontinuities between grains. Instead, they introduced a segmentation method utilizing k-means clustering for grain differentiation.

A recent trend in grain size assessment is the application of novel Deep Learning (DL) techniques [20], Convolutional Neural Networks (CNNs) [19], and Feedback Pulse Couple Neural Network (FPCNN) [9].

In this study, a grain size map for a 2.0 km long reach of the Piave River is obtained by correlating grayscale orthophoto roughness with the commonly used percentiles D_{50}, D_{84} and D_{90} of the Grain Size Curve (GSC) through a regression model. The free tool Basegrain [10] is utilized to evaluate the Grain Size Curve (GSC) of digital images acquired during field surveys. The roughness of the grayscale orthophoto is calculated over 1 m^2 tiles using the autocorrelation function and the co–occurrence matrix. The riverbed area, including dry exposed river bars, totals 1.25 km^2, implying that the total number of 1 m^2 tiles analyzed reaches 1.25 million. To manage the extensive computational demand, the orthophoto was divided into six macro areas by the computational chain. Tiles within these areas were then analyzed using a parallel computing approach. To summarize the information content of each tile, the integral length scale and five different statistics were employed for the autocorrelation function and the co–occurrence matrix, respectively.

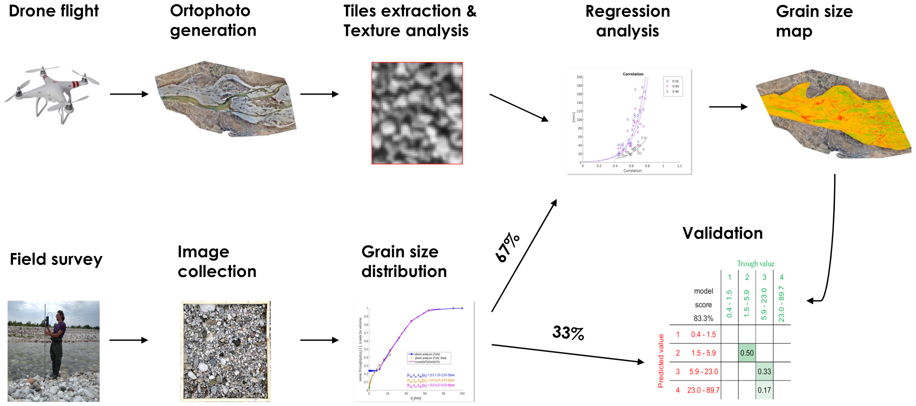

Figure 3.1: *Methodological workflow for the generation of the grain size map.*

3.2 Material and Methods

This chapter outlines the essential phases of the workflow depicted in Figure 3.1, resulting in the production of a map delineating the grain size classes of the studied section of the Piave River.

3.2.1 Study area

The study area encompasses a section of the Piave River, approximately 2 km long, with multi-thread characteristics (Figure 3.2). Its catchment covers an area of about 4000 km^2 from the Italian Alps to the Adriatic Sea, with a total length of 231 km. The average slope of the river is 3.3 meters per kilometer, and the width of the active channel extends up to 600 meters. In times of flooding, this particular segment of the river undergoes notable changes in water surface area, resulting from the overflow into side channels and sediment bars. Moreover, this specific section of the Piave River is characterized by highly dynamic morphology, marked by frequent erosion of riverbanks and islands.

Originating from the Carnic Alps at Monte Peralba, the Piave River first crosses Friuli–Venezia Giulia and then flows through the Veneto region. Its water flow is significantly altered by extractions for agricultural and energy needs, modifying its natural hydrological regime and transforming the Piave into one of the most heavily modified rivers in Europe [3].

Typically, the Piave River experiences peak flows in spring, driven by rainfall and snowmelt, and in autumn, when Atmospheric Rivers (ARs) interact with local moisture sources (e.g., the Mediterranean) and secondary circulation features of smaller spatial scale [28].

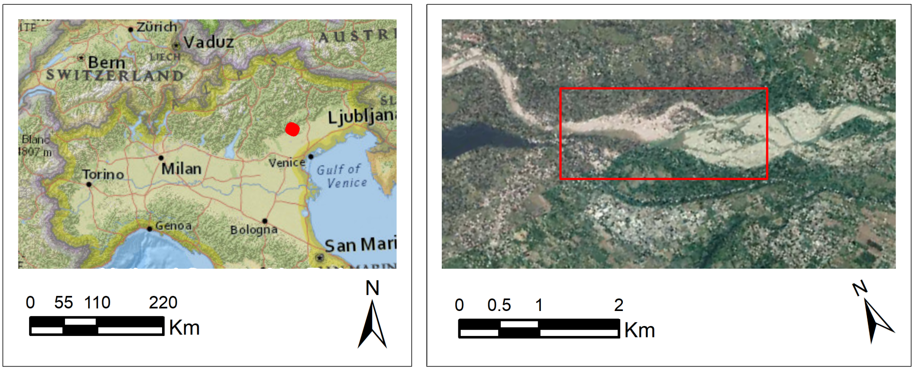

Figure 3.2: *Location of the study area along the Piave river.*

3.2.2 Digital images collection and grain size distribution

Collecting ground truth data is a crucial component of the current workflow. Twenty seven digital images were captured during the field survey using a smartphone's digital camera with a CCD resolution of 12MP, a simple yet widely used tool today. The camera was placed in a nadiral position, inclined 90° to the horizontal, capturing the images from above a wooden square, measuring 1x1 meter, placed as a dimensional reference. The images were georeferenced using a STONEX RTK-GPS for image geolocalization with centimeter accuracy. The photos were then manually rectified using speciphic tools of the free & open source image editor Gimp. Figure 3.3 displays several photographs of surface patches subsequently used for estimating the Grain Size Curve.

Grain size distribution

In this study, the grain size distribution was assessed utilizing the segmentation-based image processing tool, Basegrain [10], which is designed for the Matlab environment. This free tool allows the evaluation of the grain size curve derived from digital images captured during field surveys. The grain size curves represent thus the ground truths for the subseguent step of analysis. The approach followed for object-oriented segmentation of grains is as follows:

- detection of intensity discontinuity by means of a double grayscale threshold algorithm;
- enhancement of interstice detection using the bottom–hat transform;
- detection of grain edges with Canny and Sobel gradient filters;
- extraction of grains area combining the informtions of Canny edges and watershed bridges;
- obtain properties of the segmented grains.

Given that Basegrain exhibits limitations due to rock veins and texture variations, leading to the over–segmentation of pebbles and, consequently, an underestimation of grain sizes (Miazza et al., 2024 [21]), hand fusion operations were performed on those grains that were over–segmented.

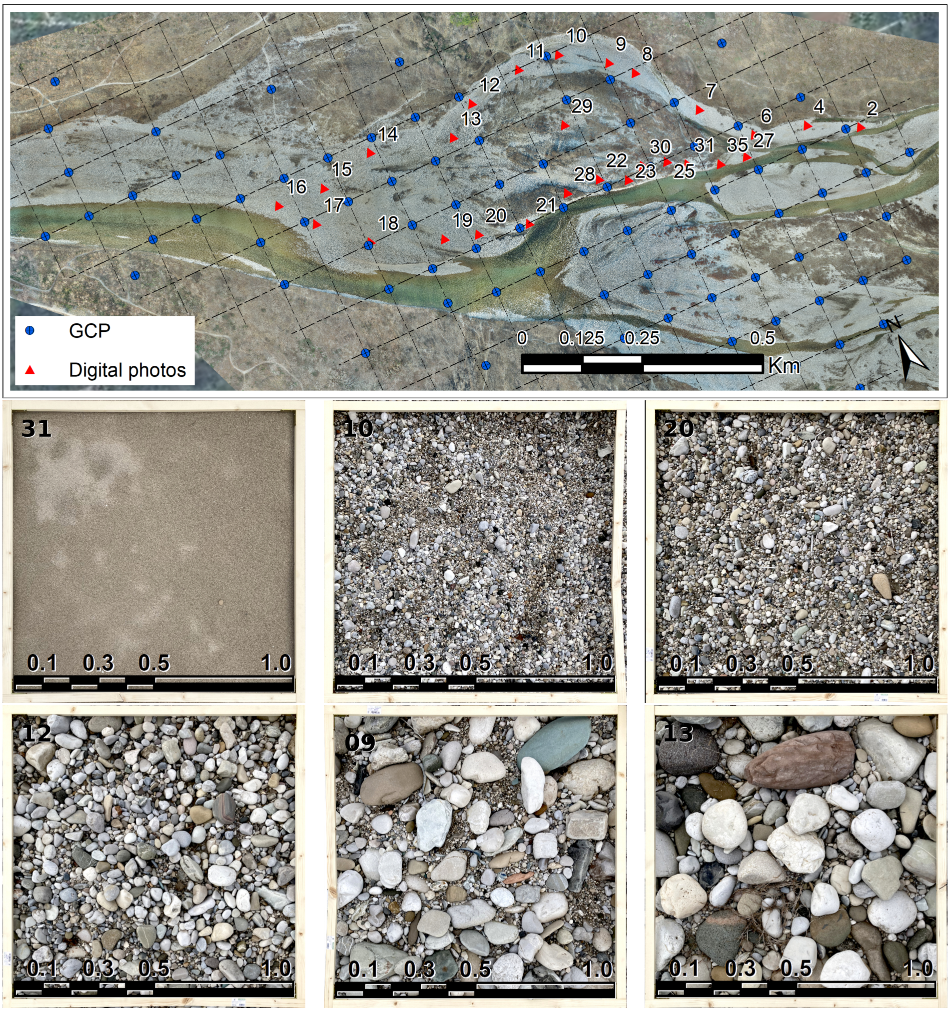

Figure 3.3: *At the top, the study site is depicted, along with the Ground Control Points (GCPs) used for image orthorectification from UAV acquisitions (blue dots), and the locations of photographs taken during the field survey (red triangle markers). Below, six of the twenty seven 1 m^2 digital images are displayed, each depicting various grain size patches.*

3.2.3 Drone flights and texture analysis

Drone flights were conducted in February 2022, using a Phantom 4 RTK GNSS at double–frequency, under weather conditions that were optimal for image acquisition. To enhance the quality of image localization, the differential correction techniques were used.

The UAV images were captured with a longitudinal overlap of 77% and a transversal overlap of 75%. Flying at an altitude of 68 meters above the ground, a Ground Sampling Pixel (GSP) of 1.86 cm was achieved.

The sixty six Ground Control Points (GCPs) were positioned in a regular mesh (Figure 3.3), achieving geolocalization with RMS errors of 4.28 centimeters for the x-coordinate, 5.14 centimeters for the y-coordinate, and 5.45 centimeters for the z-coordinate. The angle of acquisition of the camera was set to 70 degrees with respect to the horizontal.

The postprocessing of all UAV images was conducted using the commercial software Pix4Dmapper version 4.5.6, resulting in an orthophoto with a spatial resolution of 2.5 cm and a Digital Terrain Model (DTM) with a spatial resolution of 10 cm.

The spatial resolution of the orthophoto is comparable to the grain size variability of the study site. On the other hand, the quality of the geolocation is worse than the dimensions of the riverbed cobbles. However, this aspect will not affect the results in terms of grain size variability at the reach scale. It is important to note that despite these limitations, the methodology remains effective for analyzing overall sediment distribution patterns.

To extract useful information for classifying the orthophoto image in terms of grain size, texture analysis techniques were applied in this study. In general, the analysis of image textures enables the examination of the spatial pattern of the image's intensities, serving as a widely used technique for image segmentation or classification. In current literature many types of texture measures have been proposed. The most known of them are statistical approaches, autocorrelation tecniques, spatial frequency analysis, co–occurrence matrix, and texture segmentation [17]. In the present work, the autocorrelation function and the co–occurrence matrix are applied.

Autocorrelation function

The autocorrelation function measures the degree of spatial similarity of an environmental variable, essentially being the result of convolving this variable with itself. The analytical form of the autocorrelation for an image with dimensions M x N is given by:

$$\rho_{\tau_i,\tau_j} = \sum_{m=0}^{M-1} \sum_{n=0}^{N-1} I_{m,n} * I_{m+\tau_i,n+\tau_j} \tag{3.1}$$

where $\tau_i \in [0, 1, ..., M]$ and $\tau_j \in [0, 1, ..., N]$, $I_{m,n}$ represents the image intensity at position (m, n), $I_{m+\tau_i,n+\tau_j}$ denotes the image intensity at the position (m, n) translated by the lags τ_i and τ_j, and $*$ indicates the convolution operator.

Rather than employing Equation 3.1, the autocorrelation function can be calculated more efficiently through the use of the Fourier transform. Indeed, the convolution theorem delineates the convolution between two functions as $r_{(x)} = \{u * v\}_{(x)}$, asserting that for the functions $u_{(x)}$ and $v_{(x)}$ with Fourier transforms defined as:

$$\begin{aligned} U_{(f)} &= F\{u\}_{(f)} \\ V_{(f)} &= F\{v\}_{(f)} \end{aligned} \tag{3.2}$$

the Fourier transform F of the convolution $r_{(x)}$ is equal to the product of their Fourier transforms $F\{r\}_{(f)} = U_{(f)}V_{(f)}$. This, upon applying the inverse Fourier transform, yields:

$$r_{(x)} = iFFT\{U_{(f)}V_{(f)}\} \tag{3.3}$$

Therefore, the autocorrelation function between two images (Equation 3.1) can be computed using the Fourier transform and its inverse:

$$\rho_{\tau_i,\tau_j} = iFFT\left(F\{I\}F^*\{I\}\right) \tag{3.4}$$

where $iFFT$ is the inverse of Fourier transform and $*$ denotes the complex conjugate of the Fourier Transform of I. To ensure the problem is properly formulated before applying the Fast Fourier Transform (FFT) and its inverse, the images were normalized by:

$$\widehat{I_{m,n}} = \frac{I_{m,n} - \bar{I}}{\sqrt{\sum(I_{m,n} - \bar{I})^2}} \tag{3.5}$$

The mean radial value of the Auto Correlation Function (RACF) was assessed at predetermined radial intervals. For grain size estimation, the integral length scale, denoted as $\lambda = \int_0^{r_1} RACF_{(r)}dr$, where r_1 represents the first zero crossing of RACF, was calculated. Figure 3.4 displays the Autocorrelation Function and the corresponding mean radial value for a 1 m^2 tile of orthophoto.

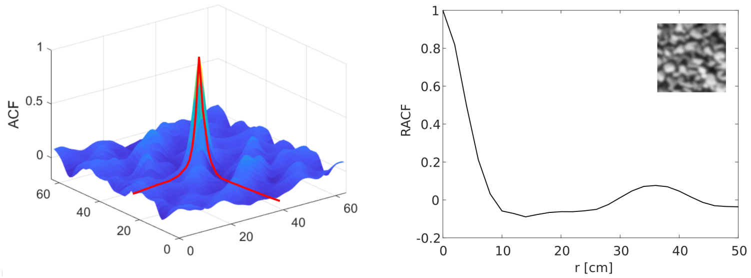

Figure 3.4: *Left: The Auto Correlation Function is calculated using Equation 3.4; Two sections are delineated by a solid red line, from which the values for calculating the mean radius of the Autocorrelation Function are derived. Right: The mean radial value of the Auto Correlation Function is presented. Top right: The grayscale tile of the orthophoto utilized for the analysis is displayed.*

Co–occurrence Matrix

This approach was sucessfully used to estimate the grain size at catchment spatial scale [6], to delineate sand patches [8], and to classify agricoltural crops [16]. particular developments concern the implementation of a multilayer and multiscale approach to the co–occurrence matrix [26], [22].

The Gray Level Co–occurrence Matrix (GLCM) results from comparing pixel gray level values and counting gray level pairs [15]. It quantifies the frequency of occurrence of a pixel with intensity $I_{(x;y)}$ at a specified distance (dx, dy) from another pixel with intensity $J_{(x+dx;y+dy)}$. The GLCM has dimension L x L, where L corresponds to the resampling gray levels of the original image. Given that the original image can be resampled to 8, 16, or 32 gray levels, the GLCM's dimensions can vary from a minimum of $8x8$ to a maximim of $32x32$ elements. Figure 3.5 illustrates a schema of the evaluation of the Gray Level Co–occurrence Matrix.

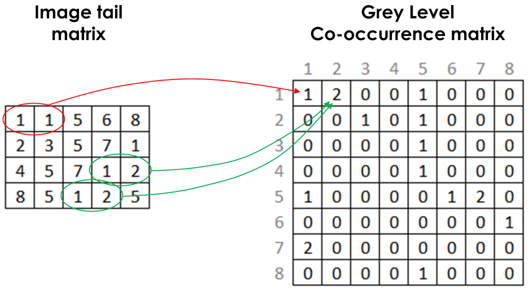

Figure 3.5: *Schema of the evaluation of the Gray Level Co–occurrence Matrix. On the right is represented the gray level image. On the left is reported the GLCM.*

To condense the Gray Level Co–occurrence Matrix's information content into a single numerical value, the statistical features of contrast (eq. 3.6 – [14]), correlation (eq. 3.7 – [2], energy (eq. 3.8 – [14]), homogeneity (eq. 3.9 – [14]) and entropy (eq. 3.10 – [8]) were applied. In the equations $P_{i,j}$ is the Co–occurrence matrix, i and j are the gray levels in the Co–occurrence matrix, μ_i and μ_j are the mean value of the i-th row and j-th column, and σ_i and σ_j are the standard deviation of the i-th row and j-th column.

$$Contrast = \sum_{i,j}^{L} (i-j)^2 \cdot P_{i,j} \tag{3.6}$$

$$Correlation = \sum_{i,j}^{L} \frac{(i-\mu_i)(j-\mu_j) \cdot P_{i,j}}{\sigma_i \sigma_j} \tag{3.7}$$

$$Energy = \sum_{i,j}^{L} P_{i,j}^2 \tag{3.8}$$

$$Homogeneity = \sum_{i,j}^{L} \frac{P_{i,j}}{1+|i-j|} \tag{3.9}$$

$$Entropy = \sum_{i,j}^{L} P_{i,j} \cdot log(P_{i,j}) \tag{3.10}$$

3.2.4 Non–linear regression model

A non–linear regression model was used to describe the functional relationship between grain size and orthophoto texture. The grain size characteristics, as represented by the D_{50}, D_{84}, D_{90} and D_{95} percentile pass rates derived from the digital images (Sec. 3.2.2), and the texture informations (integral length scale, contrast, correlation, energy, homogeneity, entropy) derived from the tiles of the gray leveled ortophoto (Sec. 3.2.3), were modeled using the power objective function $\Upsilon = A^X$. Υ is the dependent variable vector of grain sizes, whereas X is the independent variable vector of the texture informations, and A is the coefficient vector. The choice of non-linear regression was motivated by the inherently non-linear relationship between the variables. The goodness of fit, indicating how well the statistical model represents the set of observations, was assessed using the coefficient of determination R^2, defined as:

$$R^2 = 1 - \frac{\sum(y_i - \widehat{y_i})}{\sum(y_i - \overline{y})} \tag{3.11}$$

where $\sum(y_i - \widehat{y_i})$ represents the sum of squared residuals (SSR), and $\sum(y_i - \overline{y})$ is the total sum of squares (TSS). In this context, y_i denotes the observed values, $\widehat{y_i}$ the predicted values from the model, and $\overline{y}$ the mean of the observed values.

The second mertic used to evaluate the quality of the predictive model's outputs was the normalized root mean square error $NRMSE$, defined as:

$$NRMSE = \frac{1}{\overline{y}} \sqrt{\frac{(y_i - \widehat{y_i})^2}{N - 1}} \tag{3.12}$$

where N is the number of observations.

3.2.5 Model validation

To assess the model's predictive capability, the cross-validation technique was employed. This technique is extensively recognized within the fields of statistics and machine learning for determining the generalizability of statistical analysis outcomes to independent datasets. The method entails distributing the N data across K folds, each comprising N/K of the original dataset to form the validation subset. The remaining $N \cdot (1 - 1/K)$ of the data constitutes the training set, which is utilized to train the non-linear model. In the present case, the training subset comprised 67% of the data, while the remaining 33% of the data was allocated for the validation subset.

Sequentially, each fold is excluded, and the remaining dataset is employed to re–fit the regression model. This process was repeated eight times, enabling predictions for the excluded observations and allowing for the assessment of the model's predictive accuracy. Four grain size classes were utilized to verify the correspondence between actual and predicted grain size values. The mean value of the eight accuracy matrices was considered the overall predictive accuracy of the model. Figure 3.6 illustrates the process of validation.

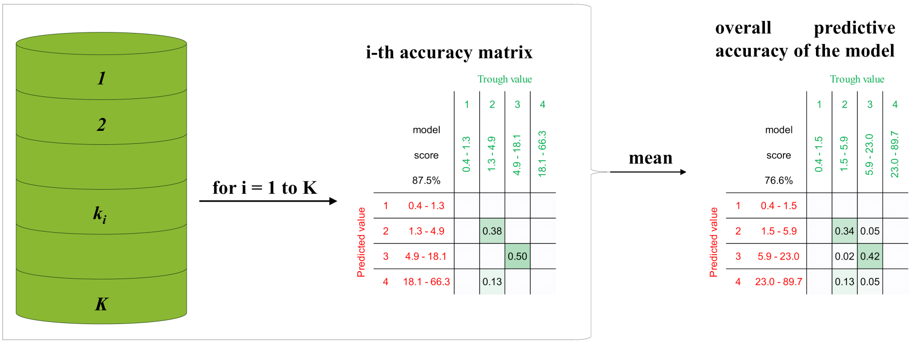

Figure 3.6: *The validation process involving a Leave-One-Out step that produces K accuracy matrices. Subsequently, a mean operator is applied to these matrices, resulting in the overall predictive accuracy matrix of the model.*

3.3 Results

In this section, the results of the grain size assessment conducted on the Piave River reach are detailed. Table 3.1 reports the values of coefficient of determination R^2 (Eq. 3.11) and Normalized Root Mean Square Error $NRMSE$ (Eq. 3.12) obtained from the analysis using the integral length scale of the autocorrelation function, along with the five statistics applied to the co–occurrence matrix. The statistical property of the co–occurrence matrix that exhibited the highest performance was correlation (Table 3.1).

Table 3.1: *Coefficient of determination R^2 and Normalized Root Mean Square Error $NRMSE$ of Autocorrelation function and Co–occurrence matrix.*

			D_{50}	D_{84}	D_{90}	D_{95}
Autocorrelation	λ	R^2	0.046	0.046	0.045	0.040
		NRMSE	0.44	0.56	0.57	0.53
Co–occurrence	Cont.	R^2	0.198	0.214	0.228	0.252
		NRMSE	0.40	0.51	0.51	0.47
	Corr.	R^2	0.613	0.652	0.648	0.665
		NRMSE	0.29	0.35	0.35	0.32
	Ener.	R^2	0.277	0.346	0.359	0.377
		NRMSE	0.39	0.48	0.48	0.44
	Homo.	R^2	0.206	0.254	0.265	0.284
		NRMSE	0.40	0.50	0.50	0.46
	Entr.	R^2	0.303	0.362	0.373	0.393
		NRMSE	0.37	0.46	0.46	0.42

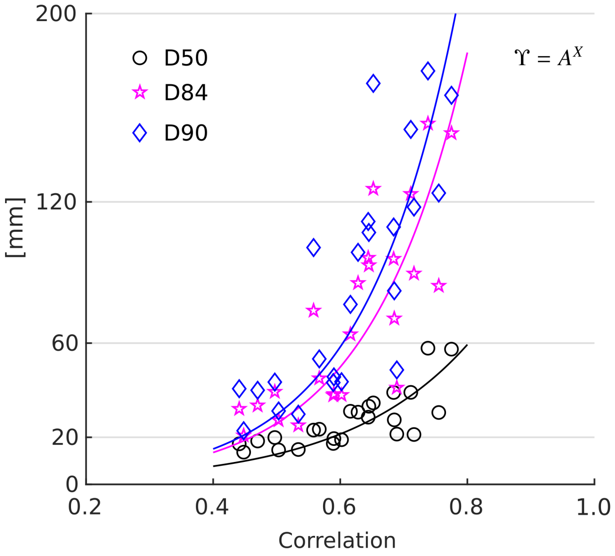

Figure 3.7: *Non–linear regression analysis of the grain size characteristics D_{50}, D_{84}, and D_{90} using the power objective function $\Upsilon = A^X$.*

Figure 3.7 illustrates the regression analysis conducted for the three percentile pass rates: D_{50}, D_{84}, and D_{90} using the correlation statistical feature of the co–occurence matrix. The analysis reveals that different grain size characteristics correspond to different ranges of correlation values. Specifically, within the correlation range of 0.4 to 0.6, the grain size characteristics are as follows: D_{50} ranges from 7.7 mm to 21.4 mm, D_{84} from 13.5 mm to 49.8 mm, and D_{90} from 15.1 mm to 58.4 mm, corresponding to the sand class.

Furthermore, within the correlation range of 0.6 to 0.8, the grain size characteristics are delineated as follows: D_{50} ranges from 21.4 mm to 59.4 mm, D_{84} from 49.8 mm to 183.4 mm, and D_{90} from 58.4 mm to 226.6 mm, corresponding to the pebble class. Values of correlation grater than 0.8 are associated with large pebbles, which have dimensions exceeding 6 cm.

The validation process, as described in Section 3.2.5, was applied to the non-linear models of the grain size characteristics D_{50}, D_{84}, and D_{90}. The models achieved overall predictive accuracies of 68.8%, 76.6%, and 76.6% for D_{50}, D_{84}, and D_{90}, respectively.

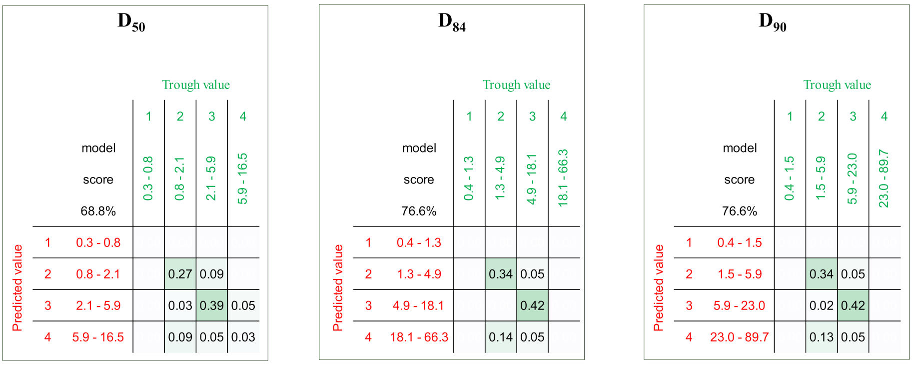

D_{50}

	model score 68.8%	Trough value 1 0.3 - 0.8	2 0.8 - 2.1	3 2.1 - 5.9	4 5.9 - 16.5
Predicted value 1	0.3 - 0.8				
2	0.8 - 2.1		0.27	0.09	
3	2.1 - 5.9		0.03	0.39	0.05
4	5.9 - 16.5		0.09	0.05	0.03

D_{84}

	model score 76.6%	Trough value 1 0.4 - 1.3	2 1.3 - 4.9	3 4.9 - 18.1	4 18.1 - 66.3
Predicted value 1	0.4 - 1.3				
2	1.3 - 4.9		0.34	0.05	
3	4.9 - 18.1			0.42	
4	18.1 - 66.3		0.14	0.05	

D_{90}

	model score 76.6%	Trough value 1 0.4 - 1.5	2 1.5 - 5.9	3 5.9 - 23.0	4 23.0 - 89.7
Predicted value 1	0.4 - 1.5				
2	1.5 - 5.9		0.34	0.05	
3	5.9 - 23.0		0.02	0.42	
4	23.0 - 89.7		0.13	0.05	

Figure 3.8: *Overall predictive accuracies matices of D_{50}, D_{84}, and D_{90} grain size characteristics.*

After conducting the non-linear regression analysis, it was determined that the correlation property of the co-occurrence matrix represented the most significant statistical attribute. Consequently, the co–occurrence matrix was calculated on the orthophoto by employing a windowed approach, with each window having a square surface area of one square meter. The correlation value was recorded at the center pixel of the square surface area. Thus, without compromising the spatial resolution of the orthophoto (2.5 cm), the spatially detailed correlation map (Figure 3.9). Using the correlation ranges of the co-occurrence matrix previously described, a grain size map containing information on the three grain size characteristics D_{50}, D_{84}, and D_{90} can be determined.

Even though the orthophoto images allow us to observe patches with different grain sizes through the air-water interface, the equations derived from the presented method require specific calibration for shallow water channels. Indeed, as highlighted by Carbonneau et al. (2005) [7], the regression law applied to the dry part of the riverbed cannot be considered valid for water channels. Furthermore, the pixel window size may not meet the minimum size required to obtain a stable signal for the variables used: the co-occurrence matrix and autocorrelation function.

3.4 Discussion

This research builds upon the methodologies established by Butler et al. (2001 [18]) , Carbonneau et al. (2003 [24], 2004 [6]), in the field of grain size assessment. This study leverages orthophotos acquired from UAV flights and digital images of dry exposed river bars collected during field surveys. By integrating autocorrelation and co–occurrence matrix texture analyses with the grain size curve derived from image grain segmentation [10], this study confirms the added value of remote sensing and image processing techniques in fluvial geomorphology.

The use of 1x1 meter digital images for ground truthing, combined with high-resolution orthophoto, allowed for the detailed and spatially continuous mapping of riverbed roughness with a resolution of 2.5 cm.

The ability to generate detailed grain size maps supports hydraulic modeling targeted towards ecological studies [23], also bolstering eco-hydraulics models that demand high spatial definition and exploit high-performance computing techniques for analysis and simulation [27]. Detailed grain size information enriches hydraulic models, providing a more accurate representation of riverbed conditions and flow dynamics. Furthermore, this data is valuable for ecological frameworks that rely on granular habitat characteristics to plan restoration projects. By offering a method to obtain spatially continuous grain size data, this study facilitates a more integrated approach to riverine ecosystem management and conservation.

During the processing of the orthophoto, several challenges were encountered, primarily due to artifacts such as blur and shadows. These issues, linked to the planning of UAV flights and the camera settings, did not compromise the final result.

3.5 Conclusions

In conclusion, this study demonstrates the potential of using orthophotos and digital image analysis for detailed and efficient grain size mapping of braided riverbeds. The work underscores the value of the correlation property of the co-occurrence matrix as a predictor of sediment size, offering an approach to support hydraulic and ecological modeling. The spatially detailed correlation map shown in Figure 3.9, coupled with the laws obtained through nonlinear regression, represents the map containing information on the three grain size characteristics D_{50}, D_{84}, and D_{90}. The validation process applied to the nonlinear models of the three grain size characteristics has ascertained a overall predictive accuracies of 68.8%, 76.6%, and 76.6% for D_{50}, D_{84}, and D_{90}, repectiely.

The UAV image postprocessing yielded an orthophoto with a spatial resolution of 2.5 cm. For geolocalization accuracy, the RMS values are 4.28 cm for the x-coordinate, 5.14 cm for the y-coordinate, and 5.45 cm for the z-coordinate. Although the spatial resolution of the orthophoto aligns with the grain size variability at the study site, the geolocalization precision is inferior to the size of the riverbed cobbles. Nonetheless, this does not compromise the results regarding grain size variability on a broader scale. It should be emphasized that despite these drawbacks, the approach still effectively analyzes the overall patterns of sediment distribution.

As riverine environments continue to face anthropogenic and environmental stressors, such as climate change, the methodologies applied in this research provide essential tools for understanding and managing these complex braided river systems. Specifically, the use of unmanned aerial vehicle (UAV) flights for grain size assessment offers detailed insights into sediment dynamics, which are critical for evaluating the ecological health of the river. These UAV-derived data allow researchers to track changes in sediment composition and distribution over time, revealing how these factors influence habitat structure and the availability of resources for aquatic life. Such information is invaluable in devising strategies to mitigate the impacts of stressors on river ecology, ensuring the preservation of biodiversity and the sustainability of these vital ecosystems.

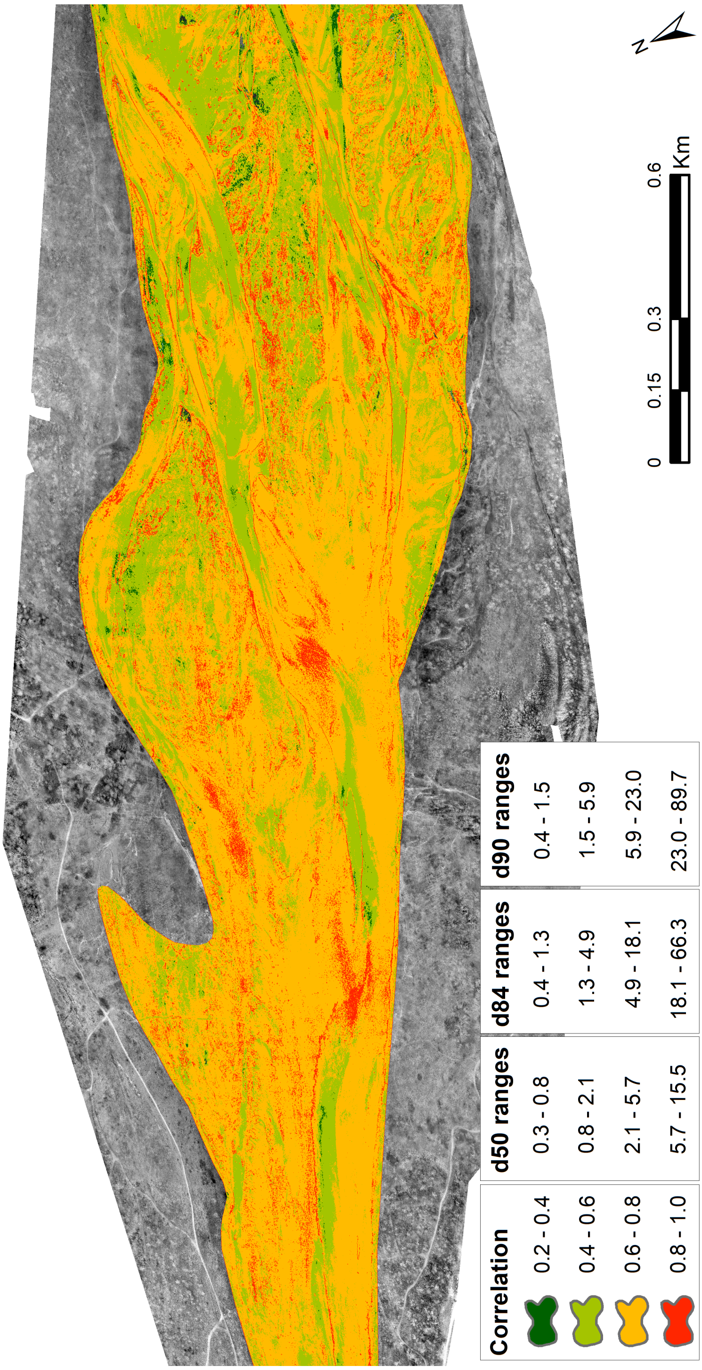

Figure 3.9: Correlation map for the Piave River reach at a 2.5 cm ground resolution, showing grain size ranges corresponding to the D_{50}, D_{84}, and D_{90} percentiles.

References

[1] Brad Murray A and Chris Paola. A cellular model of braided rivers. *Nature*, 371(6492):54–57, 1994. doi: 10.1038/371054a0.

[2] M. Bevk and I. Kononenko. A statistical approach to texture description of medical images: a preliminary study. In *Proceedings of 15th IEEE Symposium on Computer-Based Medical Systems (CBMS 2002)*, pages 239–244, 2002. doi: 10.1109/CBMS.2002.1011383.

[3] G. Botter, Stefano Basso, A. Porporato, I. Rodriguez-Iturbe, and A. Rinaldo. Natural streamflow regime alterations: Damming of the piave river basin (italy). *Water Resources Research*, 46, 06 2010. doi: 10.1029/2009WR008523.

[4] Kristin Bunte and Steven R. Abt. *Sampling surface and subsurface particle-size distributions in wadable gravel-and cobble-bed streams for analyses in sediment transport, hydraulics, and streambed monitoring*. 2001. doi: 10.2737/rmrs-gtr-74.

[5] Daniel Buscombe. Transferable wavelet method for grain-size distribution from images of sediment surfaces and thin sections, and other natural granular patterns. *Sedimentology*, 60(7):1709–1732, 2013. doi: https://doi.org/10.1111/sed.12049.

[6] Patrice E. Carbonneau, Stuart N. Lane, and Normand E. Bergeron. Catchment-scale mapping of surface grain size in gravel bed rivers using airborne digital imagery. *Water Resources Research*, 40(7), 2004. doi: https://doi.org/10.1029/2003WR002759.

[7] Patrice E. Carbonneau, Normand Bergeron, and Stuart N. Lane. Automated grain size measurements from airborne remote sensing for long profile measurements of fluvial grain sizes. *Water Resources Research*, 41(11), 2005. doi: https://doi.org/10.1029/2005WR003994.

[8] Patrice E. Carbonneau, Normand E. Bergeron, and Stuart N. Lane. Texture-based image segmentation applied to the quantification of superficial sand in salmonid river gravels. *Earth Surface Processes and Landforms*, 30(1):121–127, 2005. doi: https://doi.org/10.1002/esp.1140.

[9] Fi-John Chang and Chang-Han Chung. Estimation of riverbed grain-size distribution using image-processing techniques. *Journal of Hydrology*, 440-441:102–112, 2012. ISSN 0022-1694. doi: https://doi.org/10.1016/j.jhydrol.2012.03.032.

[10] Martin Detert and Volker Weitbrecht. Automatic object detection to analyze the geometry of gravel grains - a free stand-alone tool. *River Flow 2012 -*

Proceedings of the International Conference on Fluvial Hydraulics, 1:595–600, 01 2012.

[11] Wolman M. Gordon. A method of sampling coarse river-bed material. *Eos, Transactions American Geophysical Union*, 35(6):951–956, 1954. doi: https://doi.org/10.1029/TR035i006p00951.

[12] David Graham, Ian Reid, and Stephen Rice. Automated sizing of coarse-grained sediments: Image-processing procedures. *Mathematical Geology*, 37: 1–28, 01 2005. doi: 10.1007/s11004-005-8745-x.

[13] David J. Graham, Stephen P. Rice, and Ian Reid. A transferable method for the automated grain sizing of river gravels. *Water Resources Research*, 41(7), 2005. doi: https://doi.org/10.1029/2004WR003868.

[14] Robert M Haralick. *Computer and robot vision*. Addison-Wesley Pub. Co., –, 1992.

[15] Robert M. Haralick, K. Shanmugam, and Its'Hak Dinstein. Textural features for image classification. *IEEE Transactions on Systems, Man, and Cybernetics*, SMC-3(6):610–621, 1973. doi: 10.1109/TSMC.1973.4309314.

[16] Naveed Iqbal, Rafia Mumtaz, Uferah Shafi, and Syed Zaidi. Gray level co-occurrence matrix (glcm) texture based crop classification using low altitude remote sensing platforms. *PeerJ Computer Science*, 7:e536, 05 2021. doi: 10.7717/peerj-cs.536.

[17] Laws Kenneth Ivan. *Textured image segmentation*. Ph.D. Dissertation, University of Southern California, –, 1980.

[18] Stuart N. Lane Justin B. Butler and Jim H. Chandler. Automated extraction of grain-size data from gravel surfaces using digital image processing. *Journal of Hydraulic Research*, 39(5):519–529, 2001. doi: 10.1080/00221686.2001.9628276.

[19] N. Lang, A. Irniger, A. Rozniak, R. Hunziker, J. D. Wegner, and K. Schindler. Grainet: mapping grain size distributions in river beds from uav images with convolutional neural networks. *Hydrology and Earth System Sciences*, 25 (5):2567–2597, 2021. doi: 10.5194/hess-25-2567-2021.

[20] David Mair, Guillaume Witz, Ariel Prado, Philippos Garefalakis, and Fritz Schlunegger. Automated detecting, segmenting and measuring of grains in images of fluvial sediments: The potential for large and precise data from specialist deep learning models and transfer learning. *Earth Surface Processes and Landforms*, 12 2023. doi: 10.1002/esp.5755.

[21] Raphaël Miazza, Ivan Pascal, and Christophe Ancey. Automated grain sizing from uncrewed aerial vehicles imagery of a gravel-bed river: Benchmarking of three object-based methods. *Earth Surface Processes and Landforms*, 2024. doi: https://doi.org/10.1002/esp.5782.

[22] Luis Moya, Homa Zakeri, Fumio Yamazaki, Wen Liu, Erick Mas, and Shunichi Koshimura. 3d gray level co-occurrence matrix and its application to identifying collapsed buildings. *ISPRS Journal of Photogrammetry and Remote Sensing*, 149:14–28, 2019. doi: https://doi.org/10.1016/j.isprsjprs.2019.01.008.

[23] Michael Nones. Numerical modelling as a support tool for river habitat studies: An italian case study. *Water*, 11(3), 2019. doi: 10.3390/w11030482.

[24] Stuart N. Lane Patrice E. Carbonneau and Normand E. Bergeron. Cost-effective non-metric close-range digital photogrammetry and its application to a study of coarse gravel river beds. *International Journal of Remote Sensing*, 24(14):2837–2854, 2003. doi: 10.1080/01431160110108364.

[25] B. Purinton and B. Bookhagen. Introducing *PebbleCounts*: a grain-sizing tool for photo surveys of dynamic gravel-bed rivers. *Earth Surface Dynamics*, 7(3): 859–877, 2019. doi: 10.5194/esurf-7-859-2019.

[26] Fernando Roberti de Siqueira, William Robson Schwartz, and Helio Pedrini. Multi-scale gray level co-occurrence matrices for texture description. *Neurocomputing*, 120:336–345, 2013. ISSN 0925-2312. doi: https://doi.org/10.1016/j.neucom.2012.09.042. Image Feature Detection and Description.

[27] Marcos Sanz-Ramos, David López-Gómez, Ernest Bladé, and Danial Dehghan-Souraki. A cuda fortran gpu-parallelised hydrodynamic tool for high-resolution and long-term eco-hydraulic modelling. *Environmental Modelling and Software*, 161, 2023. doi: 10.1016/j.envsoft.2023.105628.

[28] Francesco Sioni, Silvio Davolio, Federico Grazzini, and Lorenzo Giovannini. Revisiting the atmospheric dynamics of the two century floods over north-eastern italy. *Atmospheric Research*, 286:106662, 2023. doi: https://doi.org/10.1016/j.atmosres.2023.106662.

[29] Roman Weichert, M Wickenhäuser, G Bezzola, and H Minor. *Grain size analysis for coarse river beds using digital imagery processing*, pages 753–760. 06 2004. doi: 10.1201/b16998-97.

[30] A. S. Woodget, C. Fyffe, and P. E. Carbonneau. From manned to unmanned aircraft: Adapting airborne particle size mapping methodologies to the characteristics of suas and sfm. *Earth Surface Processes and Landforms*, 43(4):857–870, 2018. doi: https://doi.org/10.1002/esp.4285.

[31] Amy S. Woodget and Robbie Austrums. Subaerial gravel size measurement using topographic data derived from a uav-sfm approach. *Earth Surface Processes and Landforms*, 42(9):1434–1443, 2017. doi: https://doi.org/10.1002/esp.4139.

Conclusion

This thesis work is comprehensively structured into three chapters.

The first chapter describes the development of the unsupervised and cloud-based algorithm for the near-real-time analysis of stack SAR images for river dynamics monitoring during extreme flood events with Sentinel–1. The proposed algorithm incorporates a Self-Adaptive Thresholding Approach (SATA), which is based on the Otsu algorithm. The algorithm, tested on a 13 km-long reach of the Tagliamento River (Italy), helped us understand the role of the buffer distance B_d from the wet-dry edges and demonstrated that a relatively small buffer width–compared to the channel width–is more appropriate for avoiding the inclusion of other land classes. It also clarified that two cycles of the thresholding algorithm enhance the bimodal distribution of the histogram, allowing for a reliable separation of the two classes: water and dry soil. The analysis of the Sentinel–1 images available in the period from 2014 to 2021 associated whit the water level recorded from the Venzone gauging station allowed us to obtain a representative law of the innundation dynamics. Two behaviors were identified: (i) for a water level less than 1 m the proportion of wet areas increases markedly from 20% to 60%; (ii) for a water level higher than 1 m, the proportion of wet areas increases less rapidly, reaching 100%. Moreover, three flood events that occurred in October 2018, November 2019, and December 2020 were analyzed to obtain the temporal evolution of the wet area proportion coupled with the water level changes. For the 2019 flood event, a bank erosion was detected, allowing us to document the time evolution of the lateral erosion. Some advancements in the structure of the algorithm could improve speckle noise removal by considering K, a parameter of the edge-stopping function, not as a fixed value but by modeling it with the generalized Gamma distribution function. To smooth the jagged contours of the planimetric delineation of wetted channels, future enhancements to the proposed algorithm might incorporate a regional growing (RG) step. This technique improves the precision of water body delineation by progressively expanding identified water pixels into neighboring areas, employing a repetitive process of thresholding and region growing until a specified tolerance level is achieved. Another element of uncertainty in the delineation of flooded areas is related to the presence of nearby dense canopy cover that prevents the C-band wavelength from reaching the water's surface. Coupling the C-band with the L-band, characterized by a longer wavelength, has the potential to enhance the accuracy and robustness of the flood area delineation process.

The second chapter illustrates the application of the algorithm to the higher ground-resolution SAR data provided by the COSMO-SkyMed mission. It examines the temporal evolution of the braiding system within the same 13 km-long reach of the Tagliamento River discussed in the first chapter, yielding (i) the temporal evolution of the Total Braiding Intensity (TBI) index, (ii) the oscillation length of the Maximum Channel Distance (MCD), and the oscillation length of the Cross-Sectional Cumulative Wetted Area (WA). The Total Braiding Intensity (TBI) index was observed to range between 2.0 and 2.3 before the peak of the flood, and it increased during the descending phase of the flood. The complex spatial oscillation behaviour of MCD and WA was then analized with the Continuous Wavelet Transform (CWT). This analysis hilighted that the dimensionless wavelengths λ for both the Maximum Channel istance (MCD) and the Cross-Sectional Cumulative Wetted Area (WA) are dependent on the hydrometric level (h). As the water level increases, the dimensionless wavelengths (λ) range from 3.5 to 5.5. For water levels greater than 0.6 meters, the dimensionless wavelengths approximately return to values around 2.2.

The last chapter focuses on the assessment of grain size in the Piave River bed, aiming to provide a comprehensive understanding of river dynamics. To achieve this, a grain size map of the Piave River bed was developed through several steps: (i) capturing digital images covering one square meter each to establish ground truths, which were then used to generate granulometric curves via an image segmentation method; (ii) conducting a drone flight to collect an orthophoto with a ground resolution of 2.5 cm; (iii) analyzing the texture of $1m^2$ orthophoto tiles, taken from the same locations as the digital images, using co-occurrence matrix and autocorrelation function techniques; (iv) performing regression analysis to correlate the texture properties of the orthophoto tiles with the granulometric indices D_{50}, D_{84}, D_{90}, and D_{95} derived from the digital images; (v) compiling these analyses into a map that illustrates the spatial distribution of grain sizes across the river reach.

Acknowledgments

For my PhD experience, I must be grateful to a wide group of people. Although the idea of pursuing a period of research had been in my mind for a long time, a chance encounter with Prof. Guido Zolezzi represented the activation energy that pushed me to write the proposal for the PhD call during a hot and sunny August. Therefore, before anyone else, I would like to thank Prof. Guido Zolezzi for giving me the opportunity to have this great life experience. I also warmly thank Prof. Alfonso Vitti and Prof. Walter Bertoldi for their patience and constant support and the valuable suggestions they provided.

As public employee, I am naturally grateful to the General Secretary of the Eastern Alps District Basin Authority, Eng. Francesco Baruffi, for allowing the realization of this project, and to Dr. Marina Colaizzi and Eng. Michele Ferri, who welcomed me back at the end of the leave period granted to me.

A special thanks to Gloria for the support and for understanding the importance of this phase of my life.

List of Figures

List of Tables

Acronyms

ANN	Artificial neural network
B_I	Braiding Index
CNN	Convolutional neural network
CWT	Continuous Wavelet Transform
CSM	COSMO–SkyMed
DL	Deep Learning
DOY	Day of the year
ES	Expert Systems
EVI	Enhanced Vegetation Index
ICD	Index Change Detection
IW	Interferometric Wide swath mode
LSWI	Land Surface Water Index
L1	Level 1 grid product of Sentinel–1
MCD	Maximum Channel Distance
NDWI	Normalized Difference Water Index
NDVI	Normalized Difference Vegetation Index
SAR	Synthetic Aperture Radar
SATA	Self-Adaptive Thresholding Approach
TB_I	Total Braiding Index
WT	Wavelet Transforms
WA	Wet Area

List of symbols

$\Psi_0(\eta)$	wavelet function
η	nondimensional “space” parameter
δ_x	spatial or temporal frequency of acquisition
δ_c	spatial frequency of acquisition
x_n	series of measurements
N	total number of measurements
ω_0	non-dimensional frequency
$W_n(s)$	Wavelet Transforms
L_b	lengths of islands and (or) bars in reach;
L_r	length of reach measured midway between banks
N_b	number of bars
N_l	number of braids
L'	distance between successive confluence and bifurcation
L_{Ctot}	sum of the lengths of all segments of the primary channel
L_{Cmax}	length of the widest channel
W_r	Width ratio index
b	width of an individual wet channel
B	total width of the active channel
L_{Main}	main channel length
L_i	length of singol bankfull braid channel
$\Re$	Real part of a complex number
$\Im$	Imaginary part of a complex number
s_0	smalest scale
Δ_j	number of sub–octaves per octave
J	largest scale
h_i	water level at time t_i
t_{SAR}	SAR acquisition time
α_r	relief slope in the range direction
θ_i	incidence angle

γ_f^0	backscatter on a flat terrain
γ^0	backscatter on a tilted terrain
α_{az}	relief slope in the azimuth direction
I_t	partial time derivative of the intensity image
I_0	initial intensity image
Δ	divergence operator
∇	gradient operator
c	edge stopping function
K	constant parameter
μ	class mean

List of publications

ISI Journal Papers: published or in press

1. **Rossi D.**, Zolezzi G., Bertoldi W., Vitti A. 2023. Monitoring Braided River-Bed Dynamics at the Sub-Event Time Scale Using Time Series of Sentinel–1 SAR Imagery. *Remote Sensing*, 15, 3622. DOI: `https://doi.org/10.3390/rs15143622`

Conferences contributions

5. **Piccolroaz S.**, Fraccarollo L., Martinengo M., Scolozzi R., Rossi D., Borga M., Fait S., Galata L., et al. 2021. Life FRANCA: a project on Flood Risk ANticipation and Communication in the Alps. *IDRA 2021*, Reggio Calabria (Italy)

4. **Rossi D.**. 2021. Detection of Gravel-bed River Dynamics Under Different Flow Conditions Using Time Series of Sentinel–1 SAR Data. *AGU 2021*, New Orleans (USA)

3. **Rossi D.**. 2022. SAR data processing for the detection and monitoring of braided gravel bed rivers morphodynamics at event scale. *ASITA 2022*, Genova (Italy)

2. **Rossi D.**. 2022. SAR data processing for the detection and monitoring of braided gravel bed rivers morphodynamics at event scale. *THE FLUVIAL SYSTEM 2022*, Modena (Italy)

1. **Rossi D.**, Bertoldi W., Vitti A., Zolezzi G. 2022. Detection of Gravel-bed River Dynamics Under Different Flow Conditions Using Time Series of SAR Data Acquisitions. *XVI CONVEGNO NAZIONALE GIT 2022*, Fondi (Italy)

This thesis investigates the complex dynamics of braided rivers, emphasizing the need for integrated management and conservation strategies to preserve their biodiversity and ecological integrity despite anthropogenic and environmental pressures. It aligns with European Directives aimed at balancing hydraulic risk reduction with water quality improvement through measures like river naturalization projects. The research introduces an innovative unsupervised algorithm developed for Sentinel-1 SAR data, capable of overcoming challenges posed by weather and day-night cycles, and adaptable to other SAR databases. This algorithm, which employs a Self-Adaptive Thresholding Approach (SATA), facilitates the accurate classification of 'dry soil' and 'water' areas, enabling analysis of inundation dynamics, hydrometric levels, and bank erosion phenomena.

The thesis further explores the relationship between morphological indices (Total Braiding Intensity, Maximum Channel Distance, Cumulative Wetted Area) and discharge variations, utilizing high-resolution COSMO-SkyMed satellite imagery to enhance the detection of narrow river branches and assess morphological changes during flood events.

The final field of research was the assessment of bed grain size using UAV imagery. By analyzing the grayscale roughness of the orthophoto and performing regression analysis to correlate texture properties of the orthophoto tiles with the granulometric features, a map illustrating the spatial distribution of grain sizes was obtained.

Daniele Rossi conducted his PhD research at the DICAM, University of Trento, facilitated by a paid leave granted by the Eastern Alps District Basin Authority. After years of experience in water resource management and hydrogeological risk planning, in November 2016 he embarked on his PhD journey, motivated by the desire to gain a deeper understanding of the morphological aspects of rivers. This period proved to be fruitful, enabling him to gain insights into the characteristics and applications of SAR data in environmental monitoring, with a particular focus on braided watercourses.